CONTRACTOR REPORT

SAND83—7024
Unlimited Release
UC-63c

The Design and Development of a High Concentration and High Efficiency Photovoltaic Concentrator Using a Curved Fresnel Lens

Ronald S. Scharlack, Abbot Moffat
Thermo Electron Corporation
Waltham, MA

Prepared by Sandia National Laboratories Albuquerque, New Mexico 87185 and Livermore, California 94550 for the United States Department of Energy under Contract DE-AC04-76DP00789

Printed August 1983

When printing a copy of any digitized SAND Report, you are required to update the markings to current standards.

Issued by Sandia National Laboratories, operated for the United States Department of Energy by Sandia Corporation.

NOTICE: This report was prepared as an account of work sponsored by an agency of the United States Government. Neither the United States Government nor any agency thereof, nor any of their employees, nor any of their contractors, subcontractors, or their employees, makes any warranty, express or implied, or assumes any legal liability or responsibility for the accuracy, completeness, or usefulness of any information, apparatus, product, or process disclosed, or represents that its use would not infringe privately owned rights. Reference herein to any specific commercial product, process, or service by trade name, trademark, manufacturer, or otherwise, does not necessarily constitute or imply its endorsement, recommendation, or favoring by the United States Government, any agency thereof or any of their contractors or subcontractors. The views and opinions expressed herein do not necessarily state or reflect those of the United States Government, any agency thereof or any of their contractors or subcontractors.

Printed in the United States of America
Available from
National Technical Information Service
U.S. Department of Commerce
5285 Port Royal Road
Springfield, VA 22161

NTIS price codes
Printed copy: A08
Microfiche copy: A01

SAND83–7024
Unlimited Release
Printed August 1983

Distribution
Category UC–63c

The Design and Development of a High Concentration and High Efficiency Photovoltaic Concentrator Using a Curved Fresnel Lens

Ronald S. Scharlack
Abbot Moffat
Thermo Electron Corporation
Waltham, MA

Under Sandia Contract No. 13–9436

Abstract

Thermo Electron has designed a high concentration photovoltaic module that uses a domed, point-focus Fresnel lens. Their design, design optimization process, and results from lens and receiver tests are described in this report. A complete module has not been fabricated and probably will not be fabricated in the future; however, Thermo Electron's optical design, analysis, and testing of both secondary optical units and domed Fresnel lenses have made a significant contribution to our project. Tooling errors prevented the lens from reaching its potential efficiency by the end of the contract, and resolution of these tooling problems is currently being attempted with a follow-on contract, #68-9463.

TABLE OF CONTENTS

Chapter		Page
1	INTRODUCTION AND SUMMARY	1
2	MODULE OPTIMIZATION	3
	2.1 COST/PERFORMANCE PARAMETERS	3
	2.2 ASSUMPTIONS	4
	2.3 RESULTS	8
3	OPTICS DESIGN	13
	3.1 LENS DESIGN	13
	3.2 SECONDARY DESIGN	15
	3.3 DESIGN MODIFICATIONS DUE TO TOOL CONFIGURATION	16
4	LENS TOOL FABRICATION	21
	4.1 TOOL DESIGN	21
	4.2 OPTICS ANALYZER	21
	4.3 INITIAL RESULTS	23
	4.4 LENS TESTING UNDER SUNLIGHT	28
	4.5 LENS AND TOOL ANALYSIS	32
	4.5.1 Beveled Facet Faces	32
	4.5.2 Tool Fabrication Options	33
	4.6 TEST TOOL	35
	4.7 INJECTION MOLDING TOOL REWORK	37
	4.8 FINAL RESULTS	37
5	CELL DESIGN AND FABRICATION	45
6	CELL COOLING	47
	6.1 JET IMPINGEMENT HEAT SINK	48
	6.2 FINNED HEAT SINK	48
	6.3 FLATTENED TUBE HEAT SINK	58
	6.4 ROUND TUBE HEAT SINK	58
	6.5 PASSIVE HEAT SINK	64

TABLE OF CONTENTS (Continued)

Chapter		Page
	6.6 GENERAL	69
	6.7 HEAT SINK MANUFACTURING OPTIONS	69
7	MODULE DESIGN	83
	7.1 DESIGN CRITERIA	83
	7.2 MODULE CASE	83
	7.3 RADIATION SHIELD	87
	7.4 CELL ASSEMBLY ATTACHMENT	91
	7.5 LENS ASSEMBLY TECHNIQUES	93
8	INSTRUMENTATION	95
	8.1 ELECTRONIC LOAD	95
	8.2 DIRECT/DIFFUSE RADIATION MONITOR	95
	8.3 CELL JUNCTION TEMPERATURE MEASUREMENT	98
9	ANNUAL ENERGY EVALUATION	107
	9.1 RESULTS	112
10	CELL TESTING	115
	10.1 MICROWAVE ASSOCIATES' EMVJ CELLS	115
	10.2 PLANAR JUNCTION CELLS	115
11	DESIGN RECOMMENDATIONS AND CONCLUSIONS	129
	11.1 LENS TOOLING AND PRODUCTION	129
	11.2 HEAT REMOVAL	129
	11.3 MODULE DESIGN AND FABRICATION	129
	11.4 SECONDARY CONCENTRATION	129
	11.5 INSTRUMENTATION	130
	11.6 GENERAL	130
	11.7 CONCLUSIONS	130
	APPENDIX 1	131

1. INTRODUCTION AND SUMMARY

The cost of electric power produced from photovoltaic cells can be made competitive with conventional power sources either by reducing the areal cost of the cells or by substituting lower-cost lenses or reflectors for expensive cell area. This latter method is the direction of the concentrator program in general and this program in particular. A high concentration ratio is desired because the cell cost can be reduced to a relatively small part of the system cost, and the fabrication of smaller cells allows the efficiency of the cells to be increased, since the areal value of the cells is high.

Thermo Electron has designed and developed a high concentration and high efficiency prototype photovoltaic concentrator based upon an injection molded domed Fresnel lens. A domed lens was chosen because the curvature of the front surface reduces reflective losses and allows high concentration ratios due to a reduced sensitivity to chromatic diffusion and off-axis errors. Figure 7.1 shows an exploded view of the module with an active cell cooling/heat collection system. Figure 3.2 shows several views of the domed lens produced during the program.

Tooling capable of low cost, large volume production of the lenses was fabricated and sample lenses have been molded and tested. The lenses demonstrate the high optical efficiency obtainable by injection molded parts. Lens efficiencies of 86 percent have been measured by Sandia Laboratories and by Thermo Electron. Errors in mold fabrication have limited the lens efficiency at high concentrations to 77 percent, but these problems are not intrinsic to the molding process and can be corrected.

Instrumentation to test the concentrator components was designed and fabricated during the program. This instrumentation includes a laser lens analyzer, an electronic load capable of measuring cell parameters and thermal impedance between the cell and heat sink, and a direct/diffuse/total radiation monitor.

Microwave Associates designed and fabricated high concentration, etched multiple vertical junction cells for this program. These cells show good efficiency at high concentrations, although additional development work is required for the cells to achieve their potential efficiency. Cells from Applied Solar Energy Corporation (ASEC) were also tested during the program.

Several cell cooling designs have been investigated in detail. These designs include both active and passive methods for removing the heat from the cell. Cell cooling optimizations employed criteria to either minimize the cost of power produced or minimize the cost of energy produced based upon annual weather data. The weather data have also been used to estimate the annual energy available to various collector configurations with either active or passive cooling.

Module designs based upon the technology developed and tested during the program have been generated and they show excellent potential for achieving the cost goals of the National Photovoltaic Program. Production techniques for manufacturing the module case and components have provided one of the major inputs for the designs.

2. MODULE DESIGN

2.1 COST/PERFORMANCE PARAMETERS

The various elements that affect the cost and efficiency of a photovoltaic concentrating system were analyzed and included in a computer program to assist in optimizing the design of the concentrating module. The cost/power ratio (or $/watt) was minimized while the concentration ratio and sizes of the curved Fresnel lenses and module were varied. This parametric analysis allowed the effects of these major design parameters to be examined in detail. The flexibility provided by this technique was useful because the exact cost and power relationships were not precisely known, therefore the precise location of a cost/power minimum was not as critical as observing an overall trend and allowing more general design and manufacturing factors to influence the design. Such factors included a desire to manufacture modules which can be readily handled by automatic machines and human operators, a tendency to select a lower concentration ratio given comparable performance because this reduces other system constraints, and a desire to utilize fewer cells and larger lenses.

The cost/power ratio was determined by the effects of the cost components and efficiency factors.

$$\frac{C}{P} = \frac{\sum_i C_i/A}{I/A \prod_j \eta_j},$$

where $\sum C_i/A$ is the summation of the individual cost components per unit area, I/A is light intensity per unit area, and $\prod \eta_j$ is the product of the individual efficiency factors.

The cost components examined were:

C_{CELL} - Cell cost, which is a function of cell size and mounting cost.

C_{MOD} - Module cost, which is a function of module size, lens size, and number of cell locations.

C_{LENS} - Lens cost, which is a function of lens area and assembly cost.

C_{INTA} - Interconnect assembly cost, which is a function of number of cells and the precision required by the concentration ratio and lens size.

C_{INTC} - Interconnect conductor cost, which is a function of the current generated by the cells and the size and number of cells in the module.

C_{MAT} - Materials cost for tracking and structure, which is a function of the stiffness required by the concentration ratio and the size of the module.

C_{ASSM} - Assembly cost for tracking and structure, which is a function of the precision required and the number of units which require precision alignment.

C_{BOS} - Balance of system cost which is related to the area of the system.

The efficiency factors included were:

η_{CELL} - Cell efficiency, which is a function of intensity, temperature, and cell size.

η_{OPT} - Optical efficiency, which is a function of lens or reflector design.

The optical efficiency, as well as the actual light intensity, affects only the magnitude of the cost/power ratio, not the locations of the minima nor the shape of the parametric curves.

2.2 ASSUMPTIONS

All cost components were expressed by the cost per aperture area, in units of $\$/cm^2$ and all dimensions are in cm.

The cell cost was estimated at \$0.50 for mounting and \$0.50/cm^2 for cell area cost, or

$$\frac{C_{CELL}}{AREA} = \frac{0.5}{D^2} + \frac{0.5}{CR},$$

where D^2 is the lens area and CR is the concentration ratio.

The module cost was estimated by assuming a material cost which is related to the module surface area and the module lateral dimension, since a large module will require additional material for stiffness. In addition, a cost adder for each cell location was included.

$$\frac{C_{MOD}}{AREA} = \frac{k_2 \sqrt{n}\, D\, (4 \sqrt{n}\, D^2 + n\, D^2) + k_1\, n}{n\, D^2},$$

where n is the number of lens units per module, k_1 is the cost adder per cell location, and k_2 is the cost factor for the module material. The above expression simplifies to

$$\frac{C_{MOD}}{AREA} = k_2 \sqrt{n}\, D \left(1 + \frac{4}{\sqrt{n}}\right) + \frac{k_1}{D^2}$$

for the analysis $k_1 = 0.10$ \$
$k_2 = 1.8 \times 10^{-5}$ \$/cm^3.

The lens cost is area related and an adder for bonding the lenses together was included.

$$\frac{C_{LENS}}{AREA} = 0.002 \text{ \$/cm}^2 + \frac{0.10 \text{ \$}}{D^2}$$

The interconnect assembly cost is related to the basic assembly cost and a cost factor, COSTF, which increases the assembly cost when additional precision is required during assembly. The cost factor is a function of the tolerance, TOL, required, which was assumed to be 0.1 times the linear cell dimension, or

$$TOL = 0.1 \sqrt{\frac{D^2}{CR}}$$

when $\quad TOL \geq 0.0254, \; COSTF = 1 + 5 \log \left(\frac{0.406}{TOL}\right)$

and when $\quad TOL < 0.0254, \; COSTF = 7 + 2.5 \log \left(\frac{0.0254}{TOL}\right).$

This cost relationship was given in the 1953 ASME Handbook: Metals Engineering Design, edited by Oscar J. Horgin in an article entitled "Designing for Production" by Roger W. Bolg. Such cost relationships are, at best, only approximations to actual cost relationships, and must therefore be used cautiously.

The interconnect conductor cost was determined by estimating the length of conductor required to interconnect the module and optimizing the conductor cross section to minimize the cost/power ratio. The estimated conductor length S is given by

$$S = n\,D \left(1 + \frac{0.65}{\sqrt{n}}\right).$$

The output power P is

$$P = P_o - i^2 R,$$

where P_o is the nominal module output, i the cell current, and R the conductor resistance.

$R = \frac{S\,\rho}{a}$, where ρ is the volume resistivity of a thin cross sectional area. When expressed per unit aperture area the above expression becomes

$$\frac{P}{A} = \frac{P_o}{A} - \left(\frac{i}{A}\right)^2 \frac{\rho\,D^3}{a} \left(1 + \frac{0.65}{\sqrt{n}}\right).$$

The interconnect conductor cost is approximated by

$$\frac{C_{INTC}}{AREA} = \frac{CPV \cdot S \cdot a}{n\ D^2},$$

where CPV is the volumetric cost of the conductor. This reduces to

$$\frac{C_{INTC}}{AREA} = CPV \cdot \frac{a}{D} \left(1 + \frac{0.65}{\sqrt{n}}\right).$$

For copper conductors $\rho = 1.724 \times 10^{-6}\ \Omega$ cm and CPV is estimated at $\$0.08/cm^3$ for an insulated and prepared interconnect. Aluminum conductors are less costly since $\rho = 2.828 \times 10^{-6}\ \Omega$ cm and CPV is estimated at $\$0.02/cm^3$.

The material costs for tracking and the structure were estimated based upon the required stiffness, which varies as the square root of the concentration ratio, and the approximate square root relationship between material required and the required stiffness. The required material also increases with the size of the structure and module.

$$\frac{C_{MAT}}{AREA} = k_3\ CR^{\frac{1}{4}}\ \sqrt{n}\ D,$$

where $k_3 = 4 \times 10^{-6}\ \$/cm^3$.

The assembly cost varies as the angular tolerance required or $\frac{TOL}{D}$, and a factor which includes the structure assembly cost, which increases with module size, and a tracking assembly cost which decreases with module size.

$$\frac{C_{ASSM}}{AREA} = \frac{k_4\ CR^{\frac{1}{2}}\ (\sqrt{n}\ D + k_5)}{n\ D^2},$$

where $k_4 = 7.5 \times 10^{-3}\ \$/cm$
$k_5 = 30$ cm.

The balance of systems cost was estimated at $\$50/m^2$ or

$$\frac{C_{BOS}}{AREA} = 0.005\ \$/cm^2.$$

The correlation for cell efficiency is

$$\eta_{CELL} = \eta_{CELL} \text{ at } CR = 100\ (CRFAC)(SFAC)(TFAC),$$

where CRFAC is the factor relating the increase in cell efficiency to increased concentration, SFAC is the factor relating the decrease of efficiency with increased cell size, and TFAC is the factor relating the decrease in cell output with increasing cell temperature.

$$CRFAC = 1 + 0.1\ [\log\ (CR \cdot \eta_{OPT}) - 2]$$

$$SFAC = 1.0167 - 0.0417 \cdot D^2/CR \cdot \eta_{OPT}$$

$$TFAC = 1.0 - T_{COEF}\ (T_{CELL} - 25),$$

where $T_{COEF} = 0.003 - 0.0005\ [\log\ (CR \cdot \eta_{OPT}) - 2]$

and $T_{CELL} \approx T_{COOLANT} + H_{FILM} \frac{I}{A} D^2\ (1 - \eta_{OPT} \cdot \eta_{CELL} \text{ at } 100).$

Preliminary studies have shown that the effects of T_{COEF} and T_{CELL} offset each other over the range of concentration ratios from 400 to 1000. Therefore, T_{CELL} was taken as 25, giving TFAC = 1.0.

Preliminary analysis had shown the uniformity of illumination (up to a 4:1 ratio) does not affect cell efficiency.

2.3 RESULTS

The evaluation of the optimization study indicated there was a broad minimum in the cost/power ratio in the range of concentration from 600 to 1000, lens sizes of 17.5 to 25 cm, and module sizes of 85 to 115 cm. (See Figures 2.1 and 2.2.) The areas of lowest cost/power occur near a module size of 90 cm on a side with lenses 22.5 cm on a side. The following table gives the cell size as a function of lens size and concentration ratio.

Concentration Ratio	Lens Size in cm (in.)			
	17.5	20	22.5	25
600	0.71 (0.28)	0.82 (0.32)	0.92 (0.36)	1.02 (0.40)
800	0.62 (0.24)	0.71 (0.28)	0.79 (0.31)	0.88 (0.35)
1000	0.55 (0.22)	0.63 (0.25)	0.71 (0.28)	0.79 (0.31)

Subjective factors indicate:

A concentration ratio of 600 to 800

A lens size of ∿22.5 cm x 22.5 cm

16 lenses per module

and Cell size at 600 x 0.92 cm (0.36) on a side

at 800 x 0.79 cm (0.31) on a side

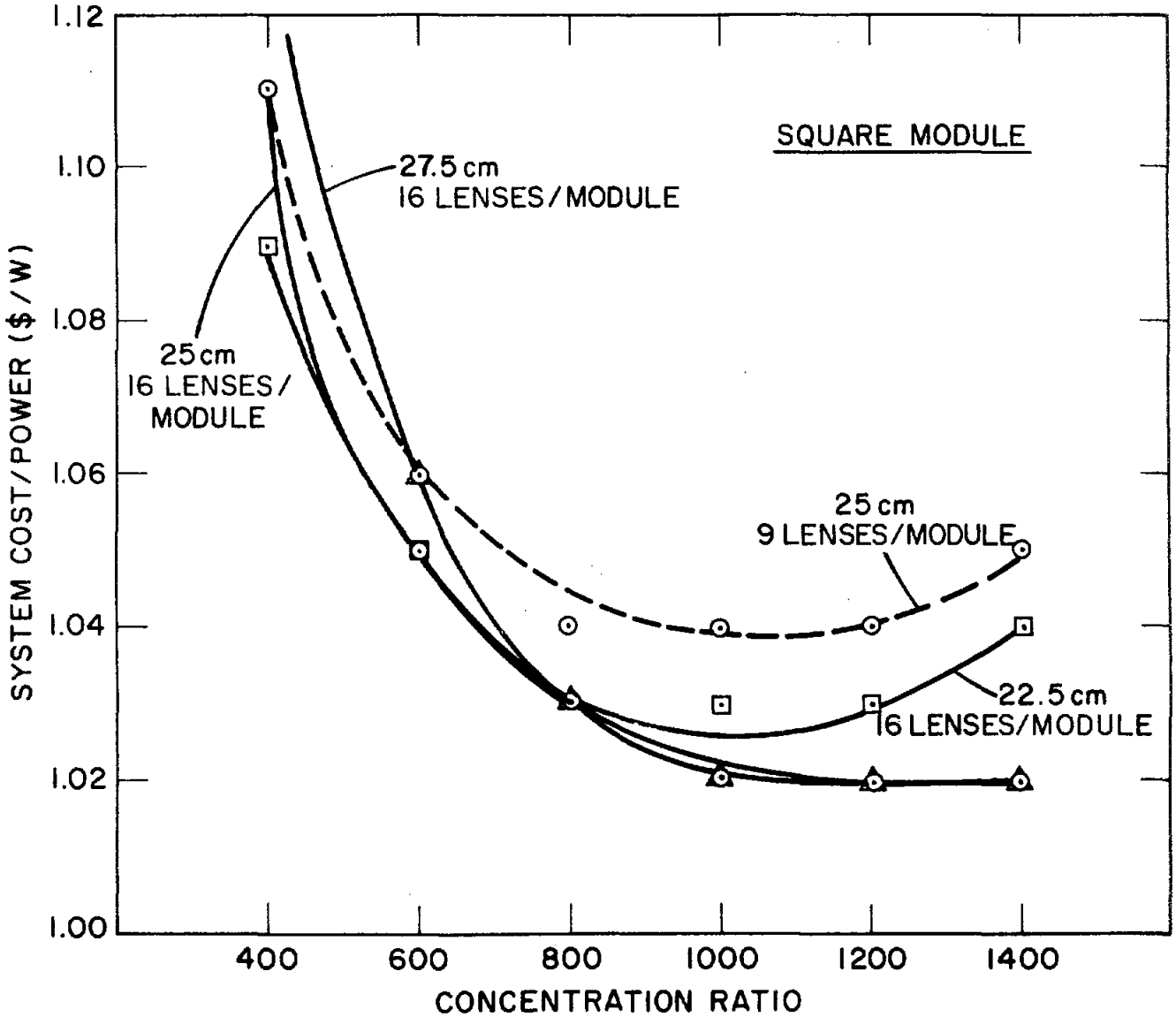

Figure 2.1 System Cost/Power vs Concentration Constant Lens Efficiency

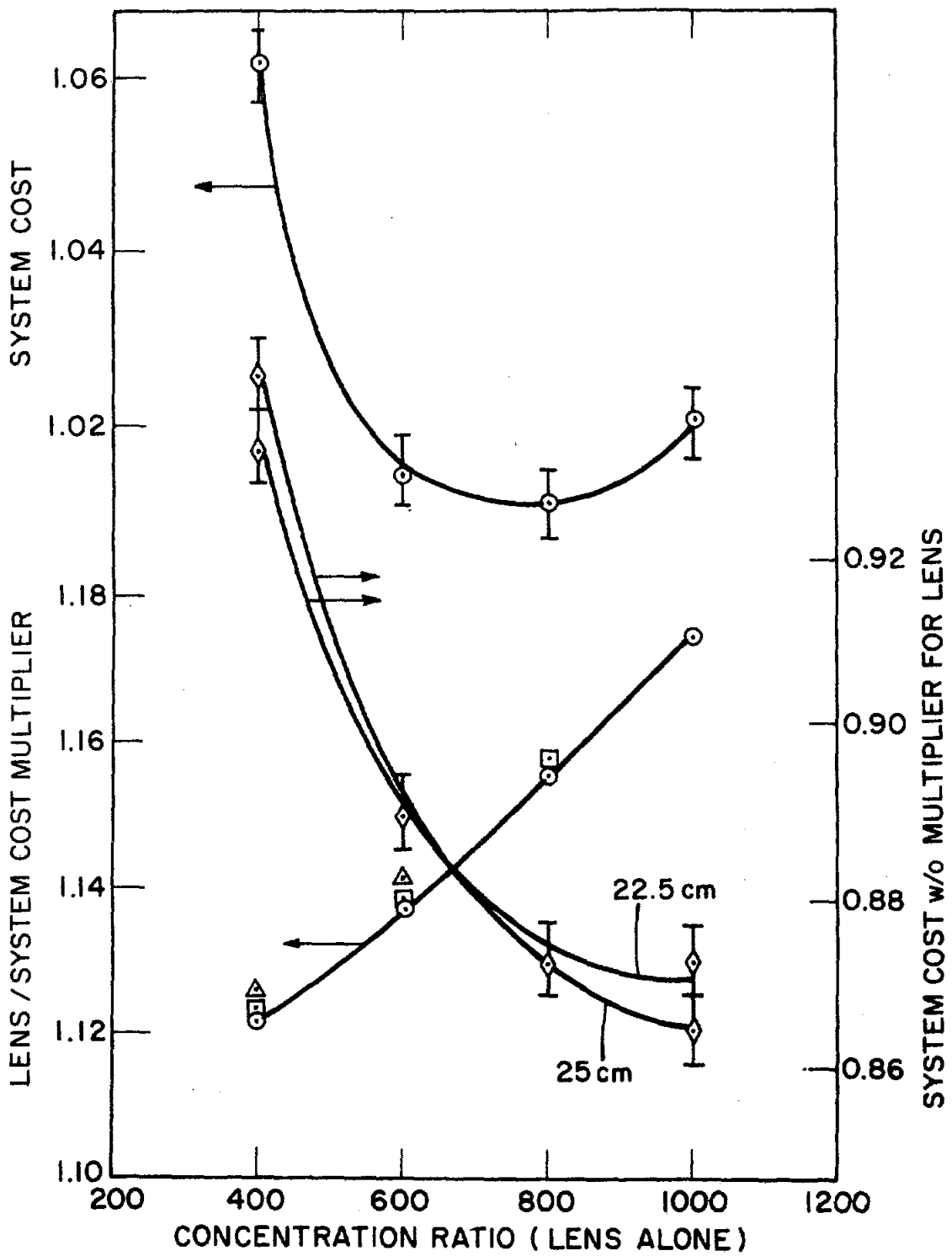

Figure 2.2 Lens Effects on System Cost/Power

3. OPTICS DESIGN

3.1 LENS DESIGN

The domed Fresnel lens is the key optical element in the module. The lens has a curved shape primarily to achieve bending of the light rays at the front surface of the lens. By distributing the light ray bending between the entrance and exit surfaces a reduction in surface reflections, chromatic aberrations, and off-axis aberrations can be achieved relative to a flat lens with a smooth front surface. A lens with Fresnel grooves on the front surface was not considered because of dirt accumulation problems. The curvature of the lens requires the use of reentrant facets (facets with negative relief angles) to eliminate refraction of light at locations on the exit surface that are not at the prescribed angles. These locations include the angles between Fresnel facets and the facet peaks that are rounded due to fabrication limitations. Figure 3.1 shows a typical lens section and facet detail. The lenses were designed to be injection molded because of the low processing costs, the tight tolerances, and excellent surface finish that can be achieved with injection molding. The reentrant facets required that the injection mold, or tooling, have a collapsible core for the release of the part after molding. Alternative release techniques, such as springing the lens facets over a solid core, were not acceptable because of the facet distortion that would result if the acrylic was sufficiently plastic to not break during release.

The entrance and exit angles of the lens were designed to balance and therefore minimize the losses from surface reflections, chromatic aberrations, and off-axis aberrations of the lens. The solar spectrum, the spectral response of the cell, and the dispersion of acrylic were accounted for in the design process. The optimized design that resulted incorporated a variable exit angle that would require curvature of the faceted surfaces. An examination of suboptimal alternatives, including those with constant exit angles, indicated that a performance degradation

A-3377

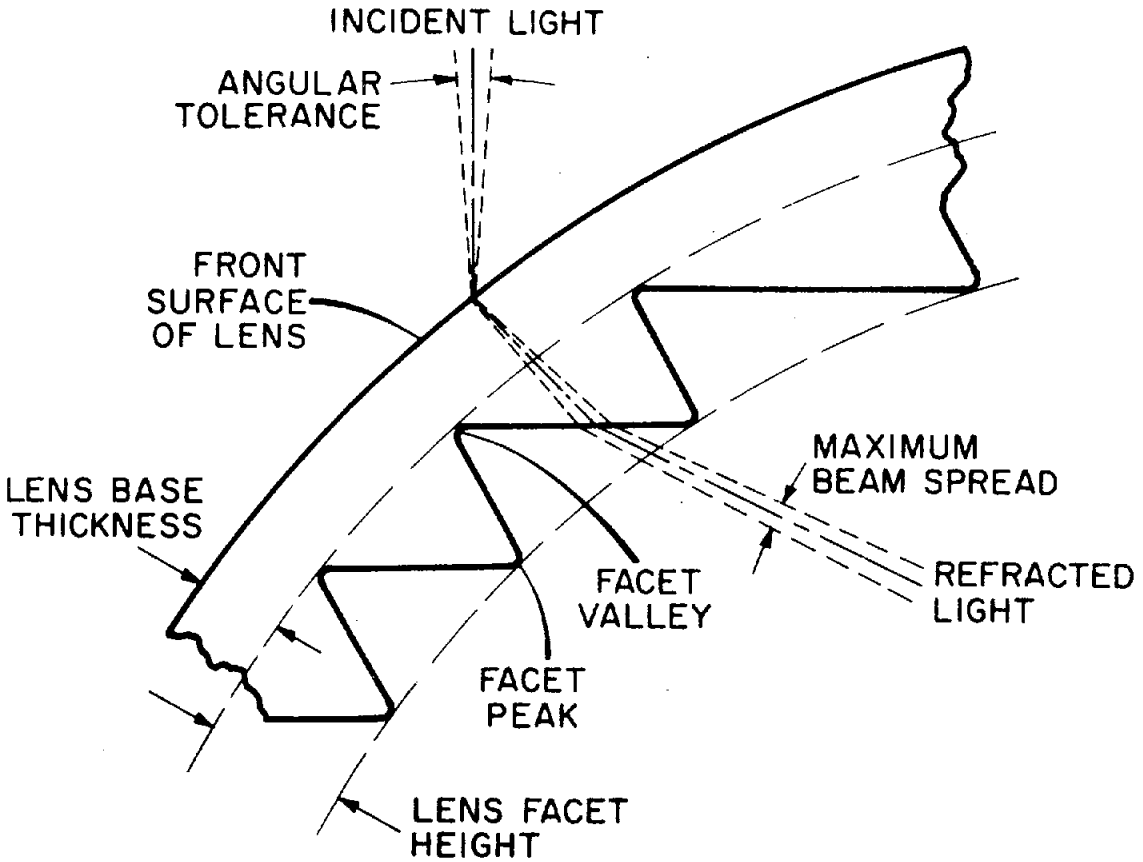

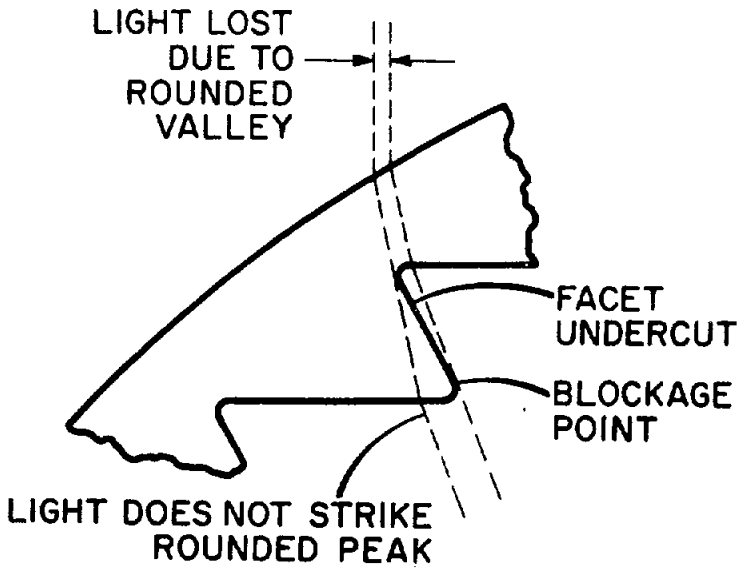

Figure 3.1 Curved Fresnel Lens and Facet Detail

of only 0.1 percent would result from the use of a plano-convex design which has an exit angle of 0°, instead of a design with curved exit angles. A lens designed with a constant exit angle has flat facets which permit simplified tool fabrication.

A square shape for the lens was selected because of the improved packing of squares in a module relative to that of circles or hexagons. Hexagons pack efficiently, but result in edges with missing segments. For example, in a rectilinear module with 16 hexagonal lenses, the packing is only 78 percent of maximum. The packing efficiency does not reach 90 percent unless there are 60 lenses per module.

3.2 SECONDARY DESIGN

The lens design was also biased to a longer focal length to allow the optional incorporation of a secondary optical element. This secondary concentrator would ideally have a compound elliptical shape, but for the prototypes the shape was limited to that of a truncated cone. The secondary concentrator was designed to be fabricated from a solid material with an index of refraction of approximately 1.5 instead of a metallic reflector to obtain both increased concentration and the use of total internal reflection. The selected material was borosilicate glass due to its low optical absorption, over the spectrum of interest, and its resistance to damage from either intense light or thermal shock. Borosilicate glass has a low coefficient of thermal expansion and therefore is well matched to silicon. This close match of expansion coefficients reduces the requirements on the physical properties of the coupling between the secondary concentrator and the cell.

Several techniques for bonding the cell and secondary concentrator were considered. These included electrostatic bonding and adhesive bonding. The adhesives under consideration were silicone, silicates, epoxies, and thermoplastics. The silicone that was used is applied with a solvent but reacts with either atmospheric water vapor or a catalyst to effect a cure. The solvent serves as a transport and viscosity reducing agent. This particular silicone was recommended and provided by Dow

Corning and is available under the number Q1-2577. Varian Associates reported good bonding and stability results from both a clear epoxy used to encapsulate LED's and the FEP thermoplastic from DuPont. The epoxy used by Varian was Hysol 050-100 (clear), but a similar epoxy, Stycast 1269A from Emerson and Cuming, was used in our experiments. DuPont's FEP is available in films of various thicknesses. We successfully bonded cells to glass with 1 mil FEP at 600°F.

Four sizes of secondary concentrators were fabricated for use with cells of different sizes. The sides of the cones formed a 78.4° angle with the horizontal in order to limit the exit angle of the light. This cone angle results in a concentration ratio of 2.3. An additional secondary concentrator design for the Microwave cells was fabricated, and this had a cone angle of 70.9°. The concentration ratio of this cone, with a higher limit on the exit angle, was 2.57.

3.3 DESIGN MODIFICATIONS DUE TO TOOL CONFIGURATION

A review of the tool design, during the fabrication of the tool, uncovered an area where potential molding problems could occur. The potential problem area arose because the core pieces slide radially inward and therefore did not provide any relief for the facets, which had a zero facet angle. Since the tool mechanism was nearly complete, it was less costly to modify the lens design and provide 2° of relief angle for the facets than to change the tool mechanism. The final lens design has a front surface with more curvature to match the -2° angle of the exit surface. A drawing of the lens is shown in Figure 3.2. Figure 3.3 shows the results of a ray trace program with a slice of the lens 25° from the lens axis and light entering 0.3° off axis.

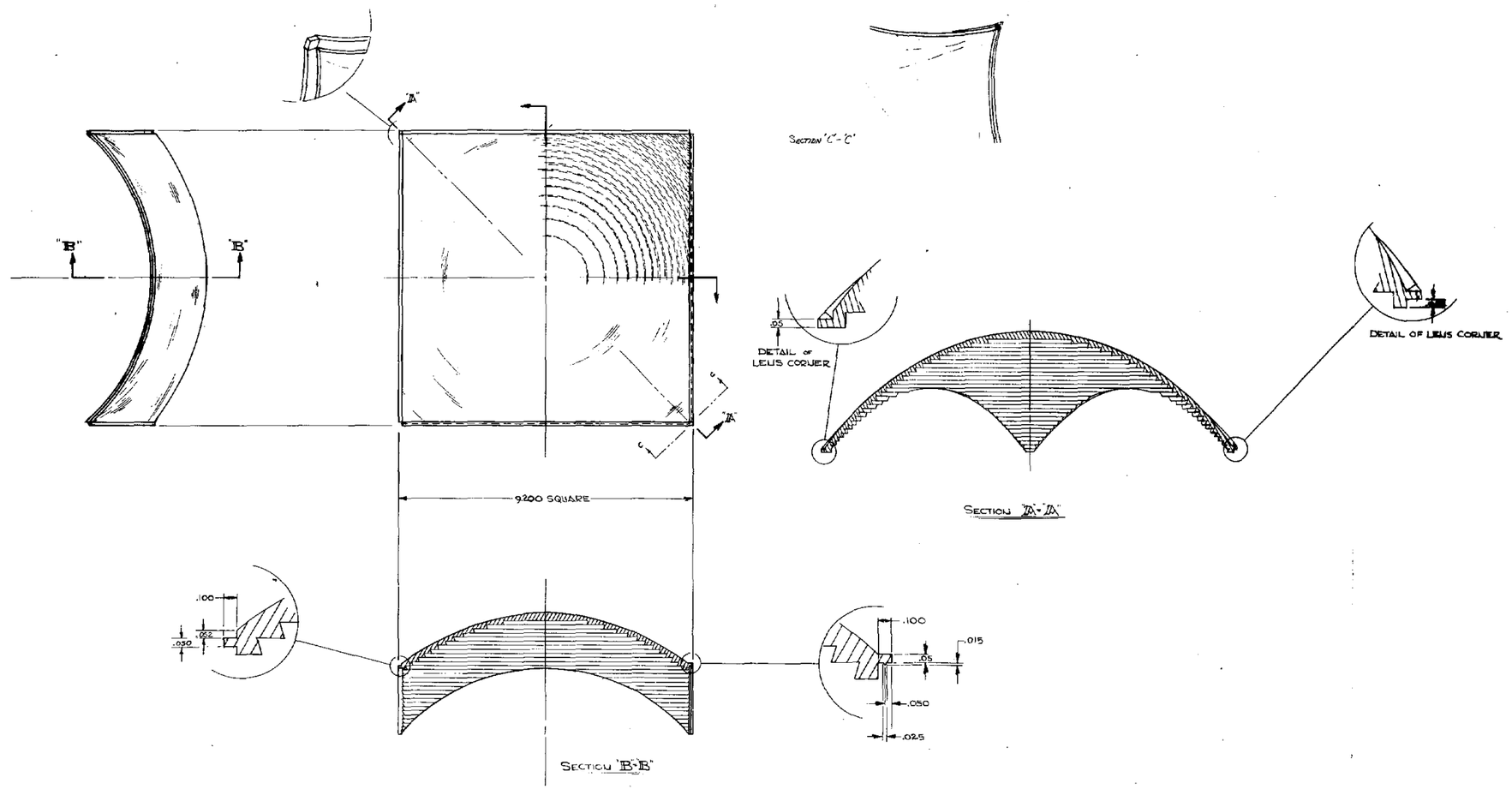

Figure 3.2 Domed Fresnel Lens

```
**** PERTINENT LENS DATA ****

-LENS PARAMETERS-

CONCENTRATION RATIO= 600.000   NUMBER OF FACETS= 50   TARGET TYPE= 1   HEIGHT RATIO= 1.0500   LENS DESIGN ANGLE= .00524

-BEAM LOSSES THRU LENS-

INCIDENCES OF TIR=  0     % ENERGY LOST TO:     INTERFERENCE= .00026     SURFACE REFLECTION=  0.0789
ANGLE OF INCIDENCE (DEGREES)= .30000     ACTUAL CONCENTRATION RATIO= 483.09

AVERAGE FACET ERROR= .00000     STANDARD DEVIATION= .00000     ILG= 3     ANG DIV=  5.000
```

0 DIST	INTEN	0	1	2	3	4	5	6	7	8	9	10
-0.700	7.7											
-0.686	11.1											
-0.672	14.5											
-0.658	17.5											
-0.643	19.3											
-0.629	21.5											
-0.615	27.0											
-0.601	33.9											
-0.587	38.2											
-0.573	49.6											
-0.559	78.5	5										
-0.544	123.8	45										
-0.530	171.5	45										
-0.516	273.6	3445										
-0.502	418.2	233445										
-0.488	565.1	12334455										
-0.474	853.9	11222333444555										
-0.460	1230.9	1122223333344444555										
-0.445	1360.8	11222223333344444555										
-0.431	1478.7	1112222223333333444444555										
-0.417	1888.8	111222222233333333444444455555										
-0.403	2323.7	11122222223333333334444444444555555										
-0.389	2495.3	111222222223333333334444444444455555555										
-0.375	2689.2	11122222222233333333334444444444555555555										
-0.361	3052.4	1111222222222233333333333344444444444455555555										
-0.346	3339.3	111122222222222333333333333444444444444555555555										
-0.332	3729.5	11111222222222222233333333333334444444444444455555555555										
-0.318	3939.6	111112222222222222333333333333334444444444444455555555555										
-0.304	4159.7	1111122222222222222333333333333334444444444444445555555555555										
-0.290	4252.5	11111222222222222222333333333333334444444444444445555555555555										
-0.276	4341.0	111112222222222222223333333333333344444444444444445555555555555										
-0.262	4435.1	1111122222222222222233333333333333344444444444444445555555555555555										
-0.247	4497.2	11111222222222222222333333333333333444444444444444455555555555555										
-0.233	4556.8	111112222222222222223333333333333334444444444444445555555555555555										
-0.219	4582.6	1111122222222222222233333333333333344444444444444455555555555555555										
-0.205	4609.2	11111222222222222222333333333333333444444444444444555555555555555										
-0.191	4630.9	111112222222222222223333333333333334444444444444445555555555555555										
-0.177	4633.9	111112222222222222223333333333333334444444444444445555555555555555										
-0.163	4630.2	111112222222222222223333333333333334444444444444445555555555555555										
-0.148	4628.0	1111122222222222222233333333333333344444444444444455555555555555555										
-0.134	4597.8	111112222222222222223333333333333334444444444444445555555555555555										
-0.120	4566.3	11111222222222222222333333333333333444444444444444555555555555555										
-0.106	4528.4	11111222222222222222333333333333333444444444444444555555555555555										
-0.092	4432.3	111112222222222222223333333333333334444444444444445555555555555555										
-0.078	4356.0	11111222222222222222333333333333333444444444444444555555555555555										
-0.064	4231.4	1111122222222222222233333333333333344444444444444455555555555555										
-0.049	4052.6	11111222222222222222333333333333333444444444444444555555555555555										
-0.035	3787.9	1111122222222222222333333333333334444444444444445555555555555555										
-0.021	3513.2	11111222222222222222333333333333333444444444444444555555555555555										
-0.007	3294.4	1111122222222222222333333333333334444444444444445555555555555555										
0.007	2865.3	11122222222233333333333444444444444555555555555										
0.021	2501.2	1122222222233333333334444444444455555555										
0.035	2374.3	112222222233333333344444444444555555555										
0.049	2239.1	11222222233333333444444444455555555										
0.064	1881.3	1122222223333334444444455555555										
0.078	1453.5	112222223333344444455555										
0.092	1207.4	12223333444445555										
0.106	1007.2	122333444444555										
0.120	689.3	2334444555										
0.134	500.9	23344555										
0.148	361.6	34455										
0.163	275.0	4455										
0.177	182.5	45										
0.191	143.0	45										
0.205	103.4	5										
0.219	74.0	5										
0.233	55.9	5										
0.247	34.3											
0.262	27.0											
0.276	21.9											
0.290	18.5											
0.304	16.5											
0.318	14.2											
0.332	11.6											
0.346	8.9											
0.361	6.5											
0.375	5.5											
0.389	4.8											
0.403	4.3											
0.417	3.7											
0.431	3.1											
0.445	2.6											
0.460	2.3											
0.474	2.0											
0.488	1.6											
0.502	1.3											
0.516	0.9											
0.530	0.7											
0.544	0.6											
0.559	0.4											
0.573	0.3											
0.587	0.1											
0.601	0.0											
0.615	0.0											
0.629	0.0											
0.643	0.0											
0.658	0.0											
0.672	0.0											
0.686	0.0											
0.700	0.0											

0MAX. INTENSITY= 6473.

Figure 3.3 Lens Ray Trace Incidence Angle 0.3°

4. LENS TOOL FABRICATION

4.1 TOOL DESIGN

One of the major goals of this program was to develop injection molding tooling for the mass production of the domed Fresnel lens. The design of the molding tool was complicated by the need to accommodate the 46 undercut facets on the inner surface of the lens. The faceted surface of the tool was required to collapse radially inward in order to release the lens after molding. This was accomplished with a nine-piece tool core, as indicated in Figure 4.1.

The release operation was performed by first drawing the center core segment away from the molded lens. This action pulls the four narrow tool segments adjacent to the center radially inward, by means of sliding dovetailed joints. Finally, the four corner quadrants of the tool move upward and slightly radially inward, releasing the molded lens. This sequence was then reversed, preparing the tool for the next molding cycle.

The first step in the fabrication of the molding tool was the machining of the dovetails and mating surfaces of the nine core segments. These were then mounted on the actuating mechanism and fixed in the "uncollapsed" position. This assembly was lathe turned as a single unit to cut the Fresnel facets. The tool core assembly had a circular geometry at this point, to avoid interrupted cutting during the lathe turning. After the Fresnel facets were cut, the core assembly was trimmed to the square design geometry. The final step was the polishing of the faceted tool surface to an optical finish. The female mold, which forms the smooth outer surface of the lens, presented no unusual design problems and was fabricated by standard machining and polishing methods.

4.2 OPTICS ANALYZER

An optics analyzer was developed to aid in determining the quality of the lenses produced by injection molding. The instrument was designed

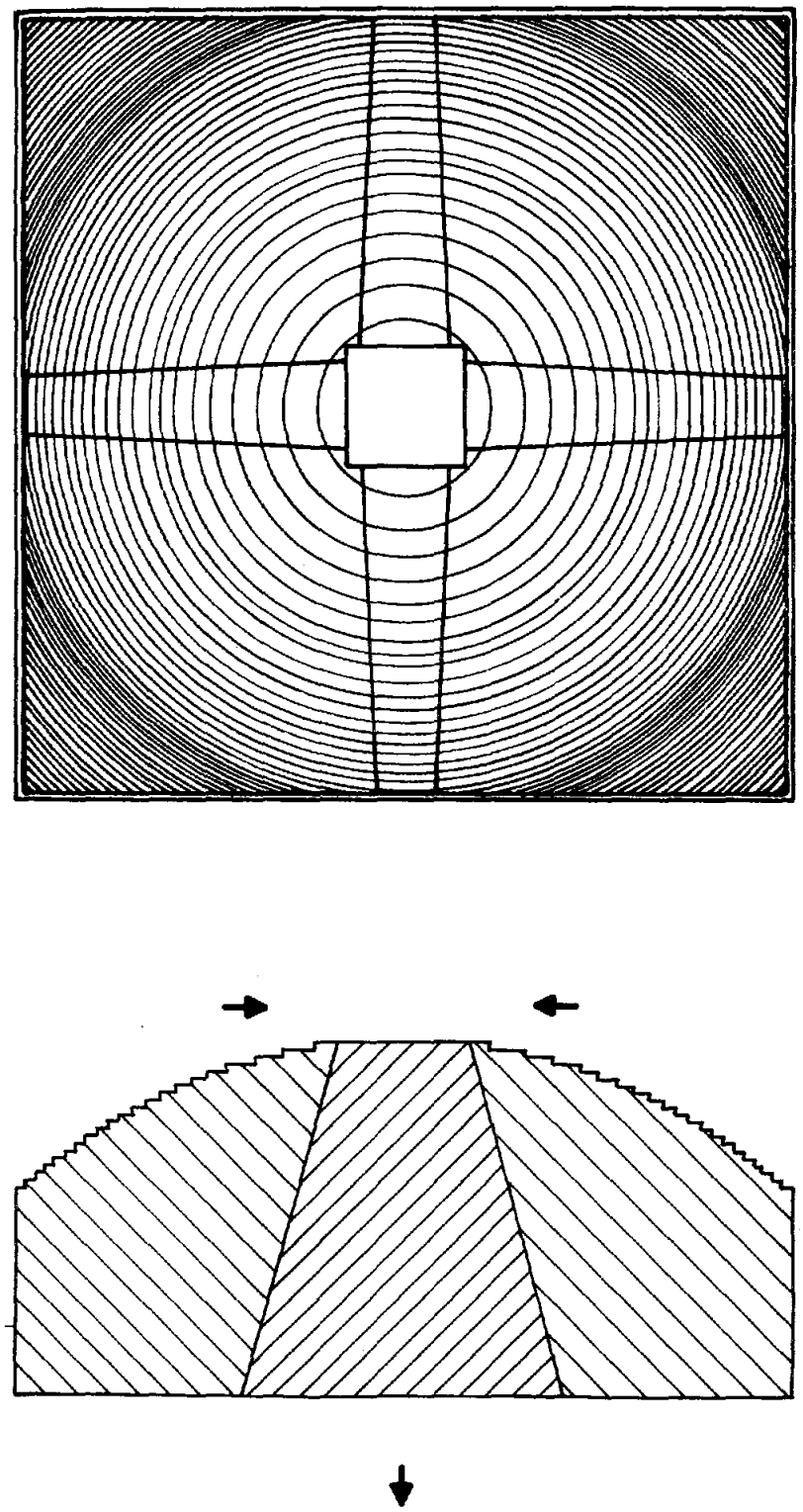

Figure 4.1 Nine-Piece Tool Core

to measure the overall transmission efficiency of a point focus lens, and also to indicate the instantaneous efficiency of any small section of a lens.

The analyzer incorporates a helium-neon laser as a collimated light source, and a solar cell detector to measure the intensity of the laser beam after it passes through the lens. The laser, mounted on a motorized linear slide, can be scanned radially across the lens. The detector is mounted at the target of the lens, and both the lens and detector are mounted on a motor-driven turntable beneath the laser, as indicated in Figure 4.2.

In the instantaneous mode, the analyzer displays the fraction of the original (unattenuated) laser beam intensity which is striking the detector at that moment. The output from a linear radial scan across a lens, with the analyzer in the instantaneous mode, is shown in Figure 4.3.

The overall transmission efficiency of a point focus lens was measured by performing a linear radial scan with the laser while rotating the lens beneath it, and integrating the instantaneous output of the detector. In this manner the entire active area of the lens was examined in a tight spiral scan. A potentiometer mounted on the motorized slide functions as a position indicator. The output of the potentiometer was used by the integrating circuitry to adjust the instantaneous value of the laser signal to reflect the increase in lens area represented by each turntable revolution as the laser scans from the center of the lens to its corner. The integrated output from a spiral scan is shown in Figure 4.4. A schematic of the optics analyzer circuitry is shown in Figure 4.5. Figure 4.6 is a photograph of the optics analyzer in operation.

4.3 INITIAL RESULTS

Lenses were first molded on the tool after the Fresnel facets were cut, but before these surfaces were polished. The purpose of this production run was to verify the mechanical functioning of the collapsible

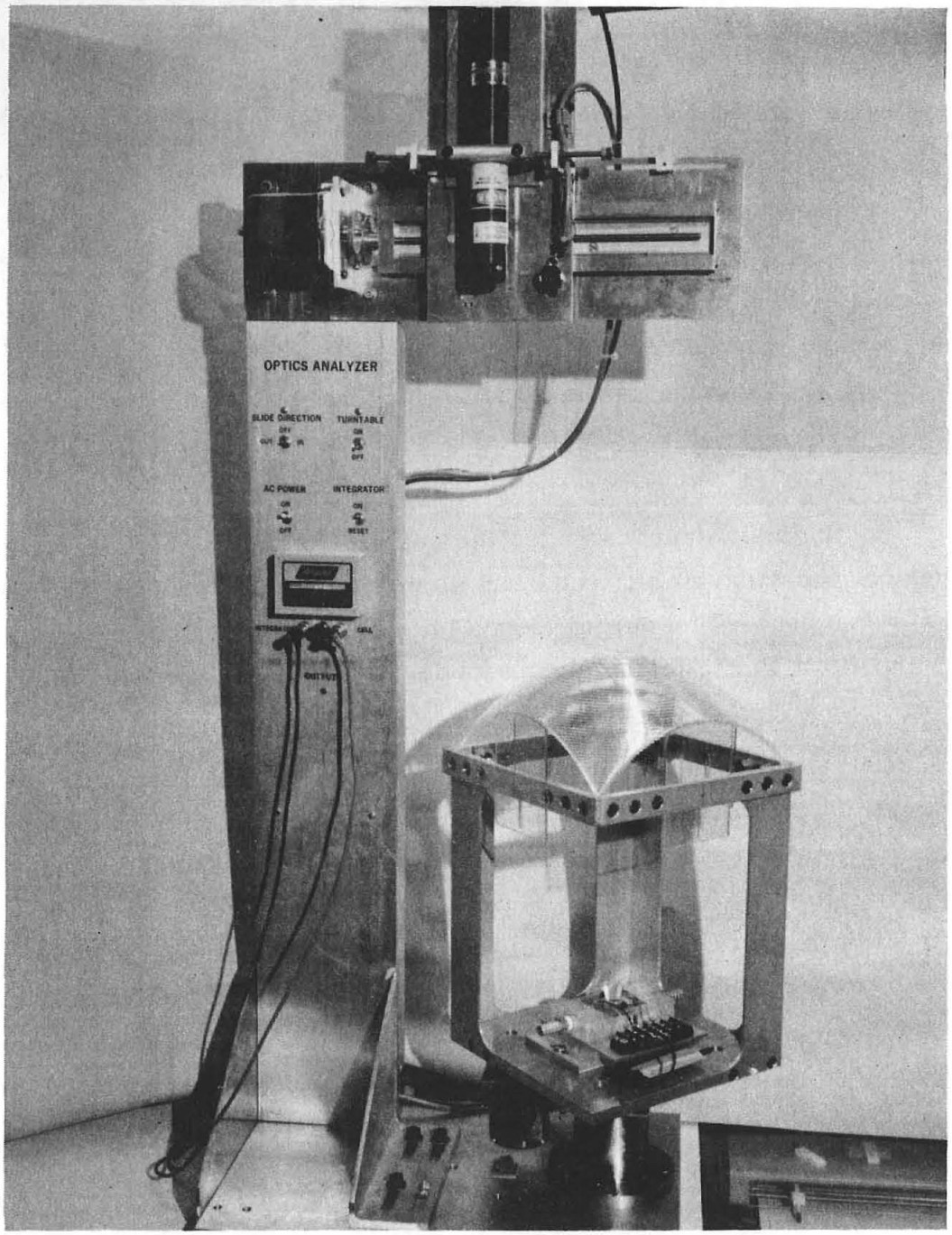

Figure 4.2 Optics Analyzer

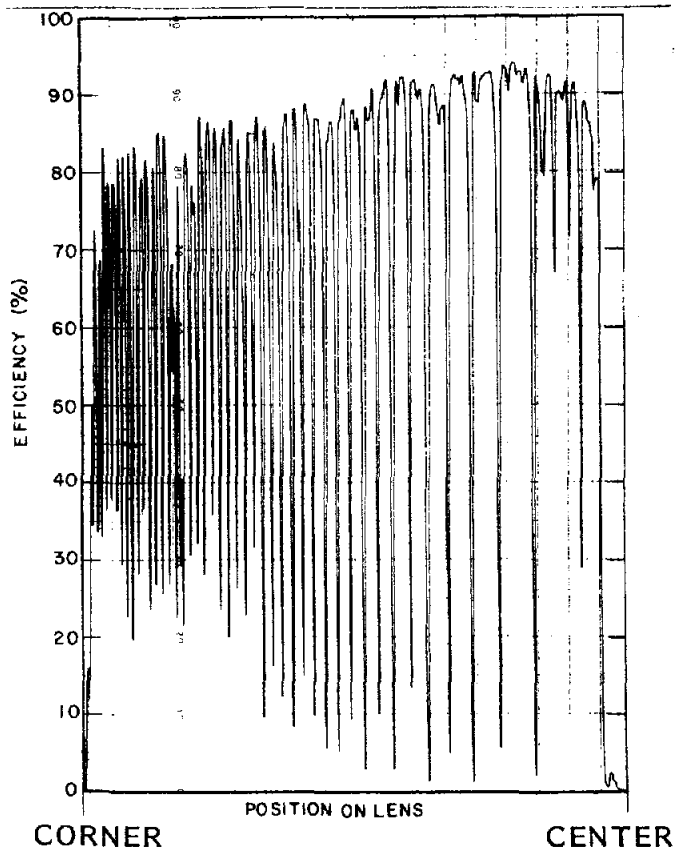

Figure 4.3 Instantaneous Output From Linear Scan

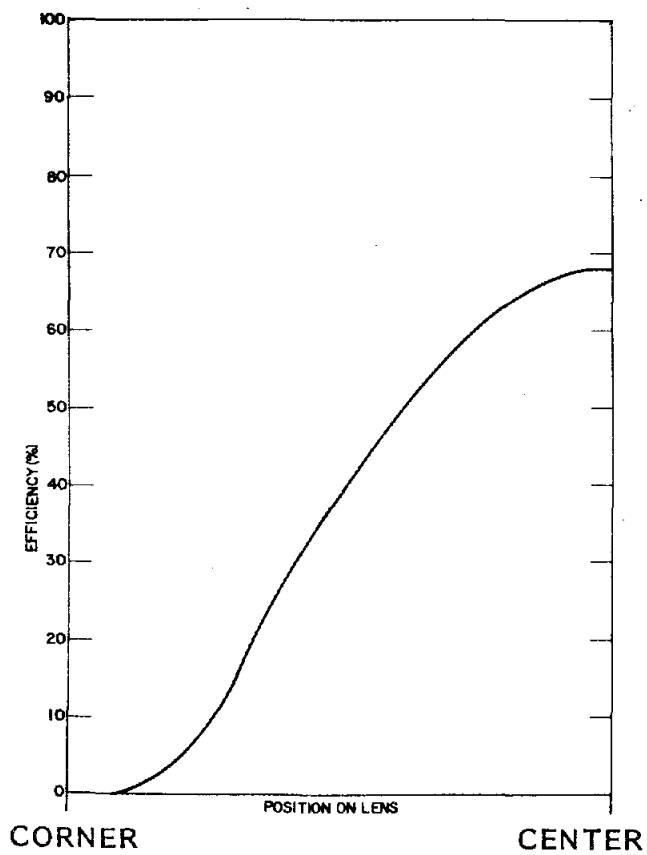

Figure 4.4 Integrated Total Output From Spiral Scan

A-6066

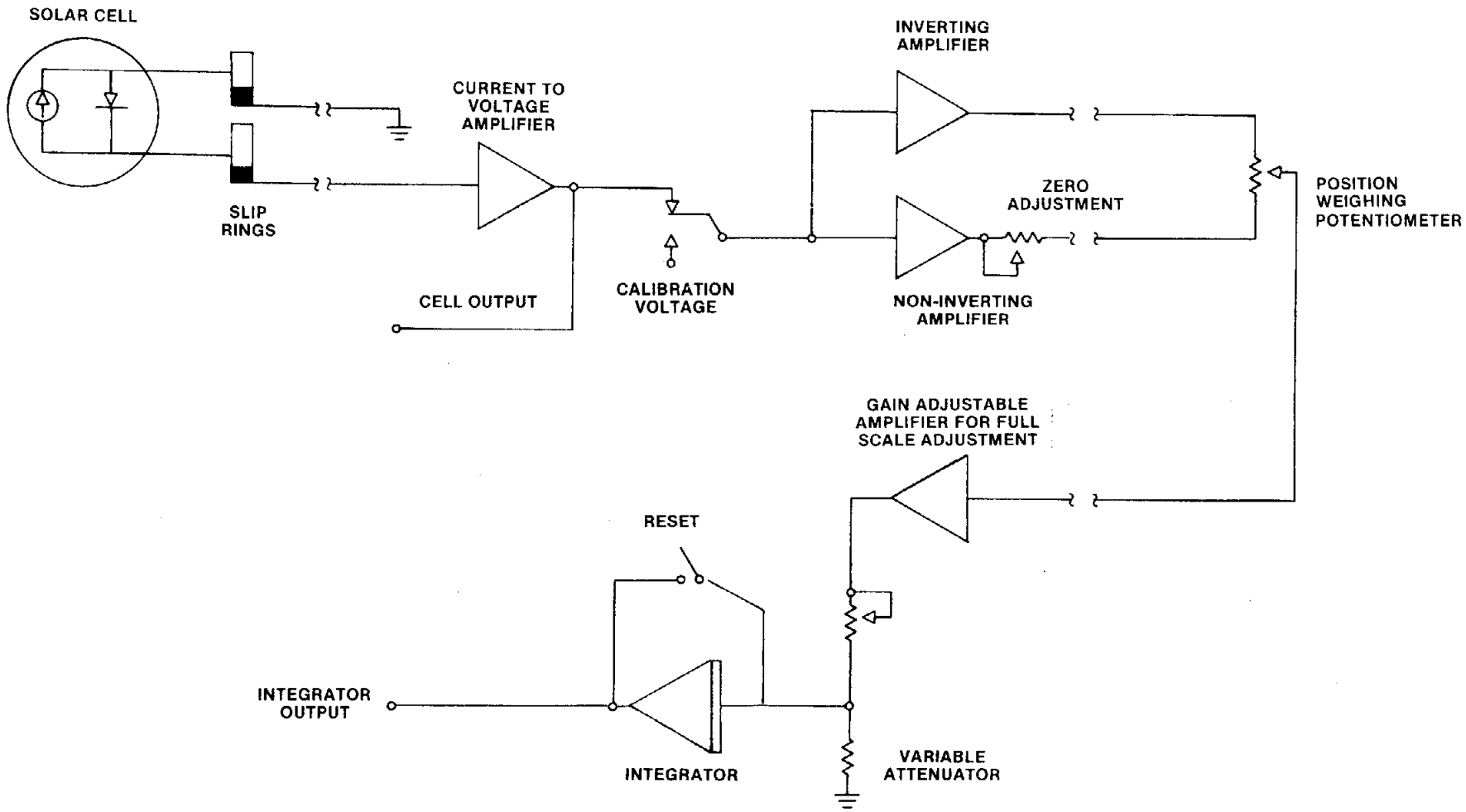

Figure 4.5 Schematic of Lens Analyzer Electronics

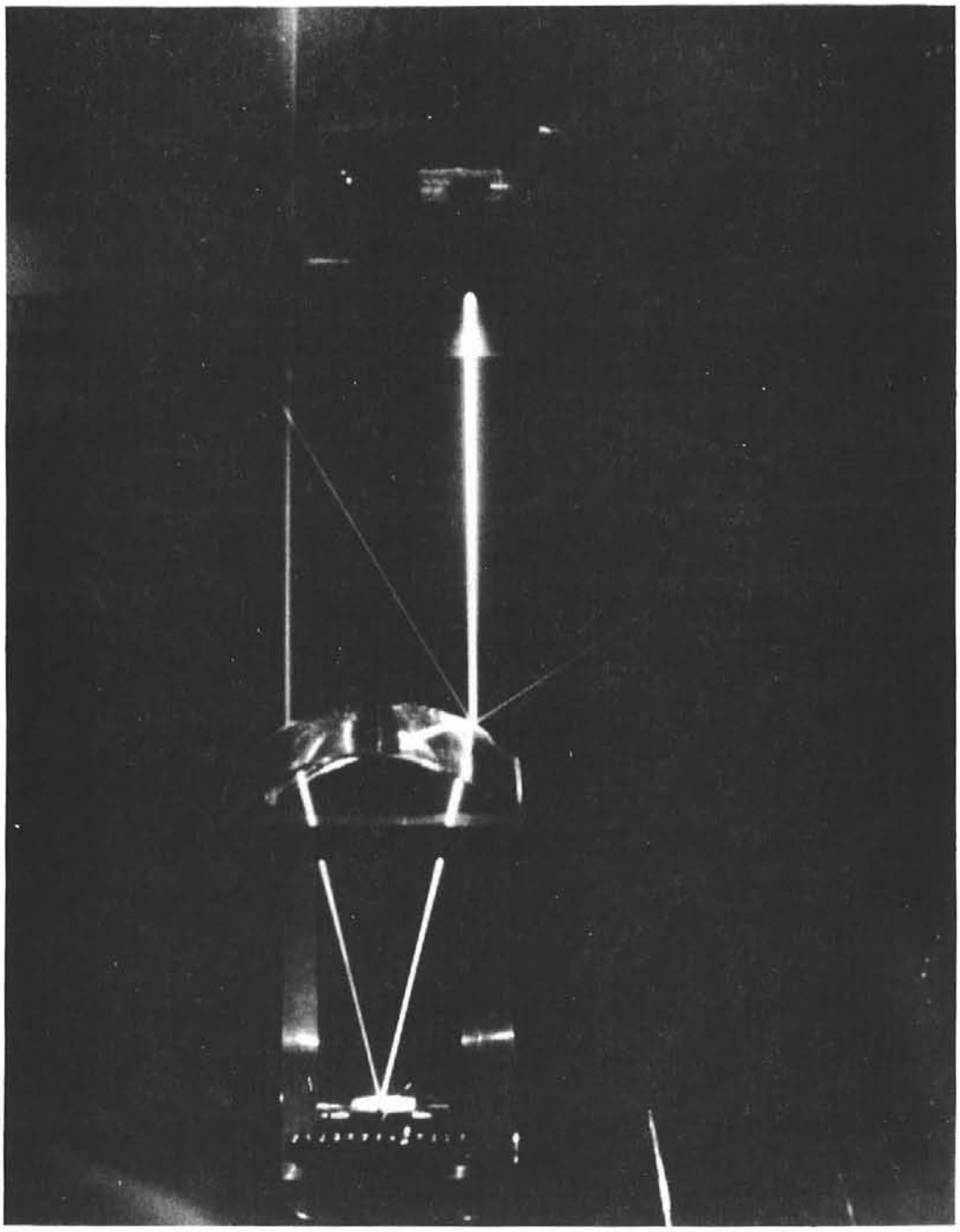

Figure 4.6 Optics Analyzer in Operation

core tool. The tool functioned correctly; although the inside surfaces of the lenses were unpolished, the overall geometry of the molded parts appeared promising. The Fresnel facets faces were flat and the facet valleys were quite sharp. The facet peaks were rounded, with tip radii in the 0.008- to 0.012-in. range, rather than the 0.004- to 0.005-in. range specified in the design. This peak rounding was initially thought to be due to nonoptimal molding parameters such as low melt temperature, rapid cycling time, and low injection pressure, rather than due to rounded facet valleys on the tool. The central section of these lenses was not correct, as the center core segment of the tool had not been machined to the proper shape. This information was communicated to the molder.

After the molding tool was polished, another run of lenses was produced. Although the physical appearance of these was greatly improved over the unpolished run, their optical efficiency was much lower than expected. Efficiency measurements made on the optics analyzer at Thermo Electron and performance testing under sunlight at Sandia's point focus Fresnel lens test facility both yielded efficiency values in the 69- to 70-percent range for a target cell size of 0.37 in. x 0.37 in.

4 4 LENS TESTING UNDER SUNLIGHT

The lenses were tested under sunlight at Sandia's point focus Fresnel lens test facility. Typical results are indicated in Figures 4.7 through 4.9. These results agreed very closely with those obtained on the optics analyzer at Thermo Electron; i.e., approximately 70 percent for a 0.37-in. square target increasing to approximately 85 percent for a 0.75-in. square target.

Additional sunlight testing was performed at Thermo Electron. The technique was measurement of the short circuit current (I_{sc}) of a well-characterized cell at 1 sun. The cell was then illuminated by the lens, and the ratio of I_{sc} at concentration to I_{sc} at 1 sun was used to determine the average intensity of light on the cell. Multiplying this intensity by the cell area and dividing by the lens area and the intensity of direct

A-5800

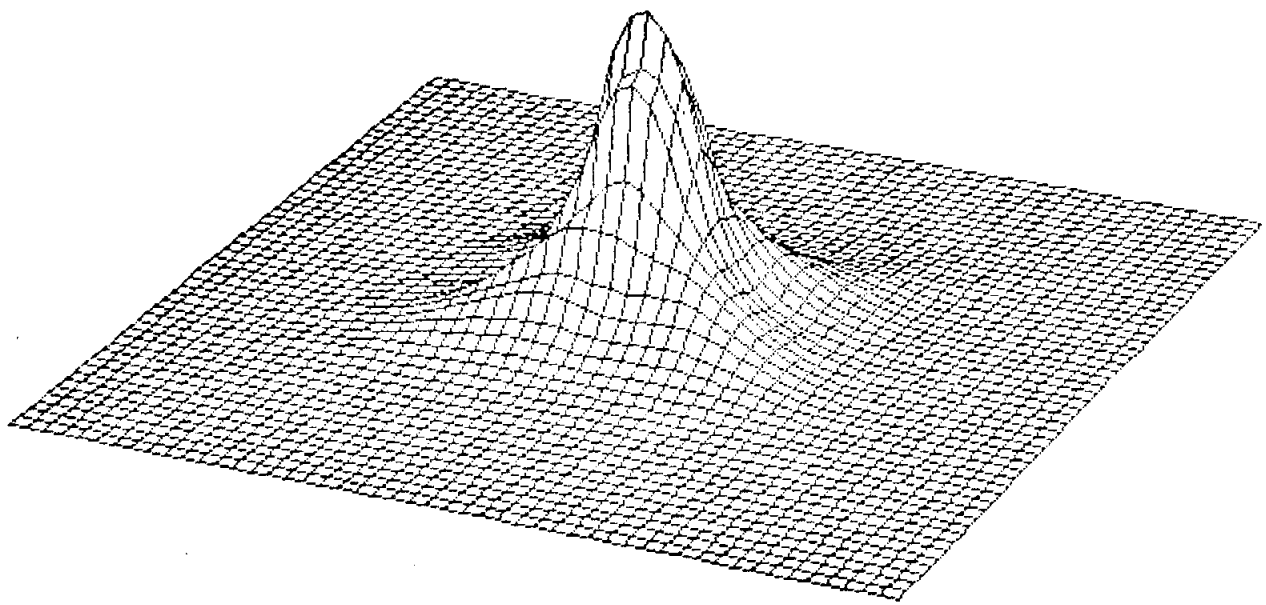

3-D PLOT OF FILE THE09
E1 - 25 Az - 25
Scan Efficiency = 85.54%

File THE09 recorded on 6/9/31 at 1130 used 1 filter(s).
Ws = Clear with a thin haze
Cs = Thermo Electron domed VM 100 lens #2, L-to-C = 13.63
Ratio = 1.20038273622 Fltfac = 2278.32643335 F10
Pts = 51 Lns = 51

This rectangular lens has dimensions of 9 by 9 in.

Figure 4.7 Sandia Test Results of Initial Polished Lens

A-5801

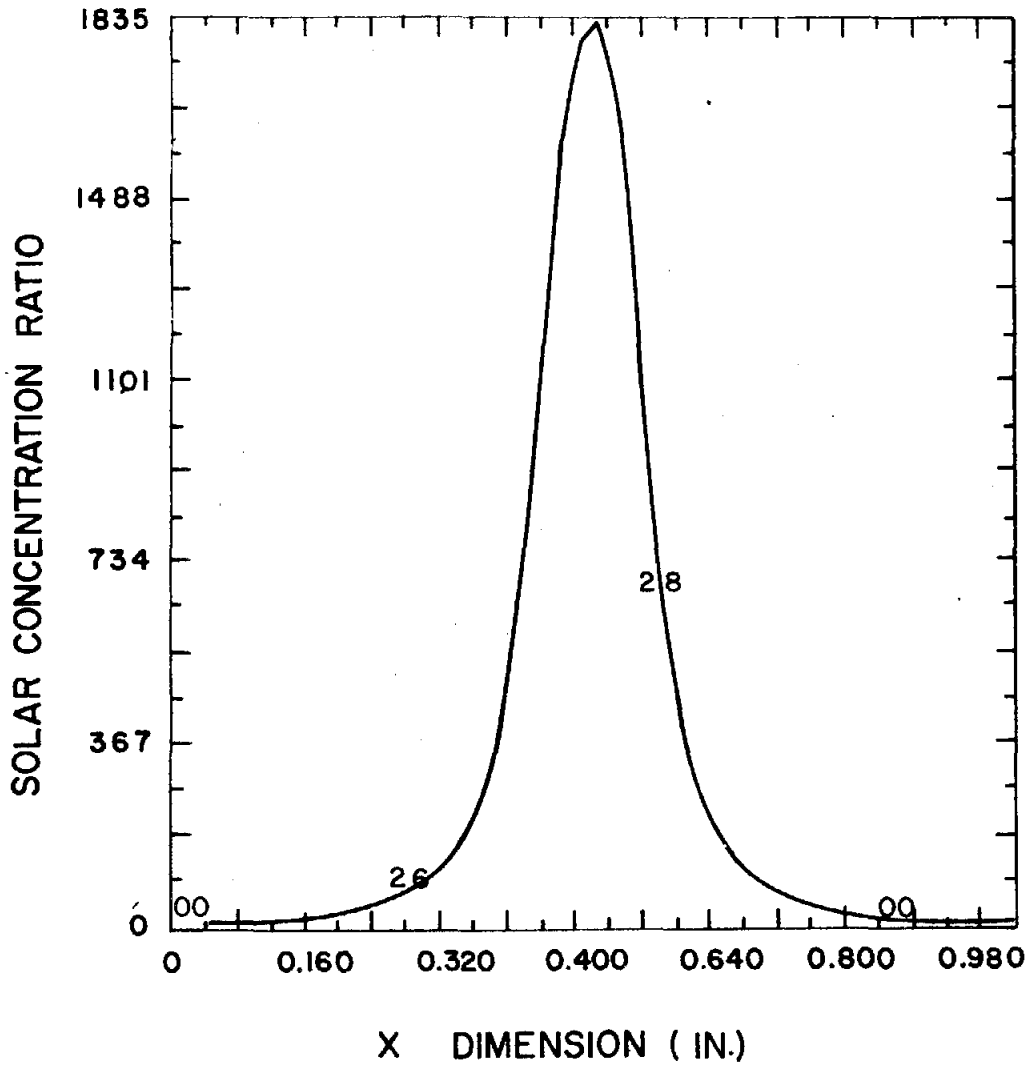

PLOT OF SLICES:
26
OF FILE THE09

Image dimensions = 0.787, 0.787

Lens efficiency = 88.29%

Ave concentration = 115.46

Scan efficiency = 85.54%

Max scan conc. = 1834.70

Ave scan conc. = 69.29

File THE09 recorded on 6/9/81 at
1130 used 1 filter(s).
Ws = Clear with a thin haze
Cs = Thermo Electron domed VM 100
lens #2, L-to-C = 13.63
Ratio = 1.20038273622
Fltfac = 2278.32643335 F10
Pts = 51
Lns = 51

This rectangular lens has dimensions
of 9 by 9 in.

Figure 4.8 Sandia Test Results of Initial Polished Lens

A-5802

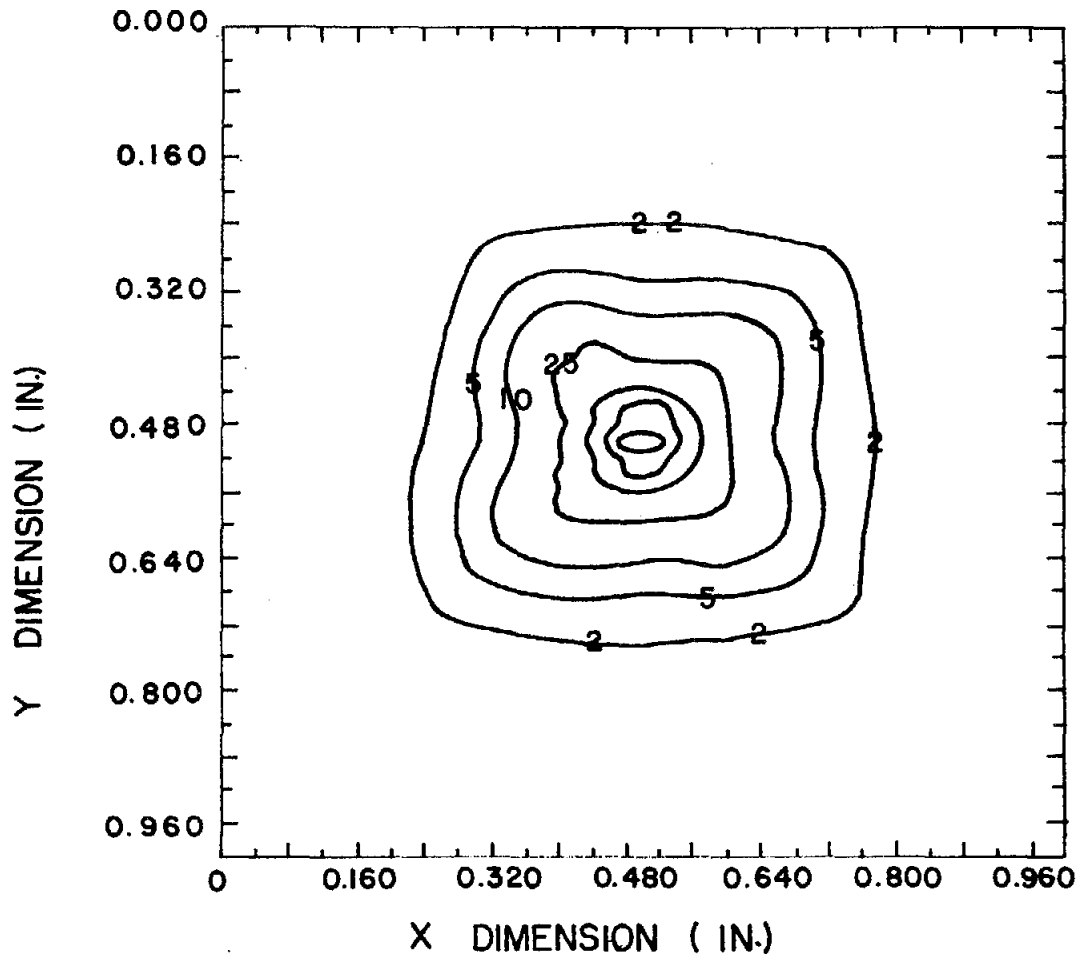

PLOT OF CONTOURS (%)
2
3
10
25
50
75
90

OF FILE THE09

Image dimensions = .37, .37

Lens efficiency = 00.11%

Scan efficiency = 85.54%

File THE09 recorded on 6/9/81 at 1130 used 1 filter(s).
Ws = Clear with a thin haze
Cs = Thermo Electron Domed VM 100 lens #2, L-to-C = 13.63
Ratio = 1.20038273622 Fltfac = 2278.32643335 F10
Pts = 51 Lns = 51

This rectangular lens has dimensions of 9 by 9 in.

Figure 4.9 Sandia Test Results of Initial Polished Lens

sunlight yields the lens efficiency. This calculation assumes that I_{sc} increases linearly with intensity. The results obtained by this method agreed very well with the measurements taken at Sandia and on the optics analyzer. Lenses molded from Rohm & Haas VM 100 and VO 52 injection molding pellets achieved efficiencies in the 69- to 70-percent range on 0.37-in. square target cells. Lenses molded from Rohm & Haas VS 100 pellets were slightly less efficient.

4.5 LENS AND TOOL ANALYSIS

As a result of careful examination with the optics analyzer and under a microscope and optical comparator, several distinct problems were found with the lens geometry. A major error was introduced during the polishing of the tool. Instead of maintaining the flat geometry of the facet faces as they were cut, the polishing technique resulted in beveling the tool facet faces. The bevel existed on a majority of the facet faces, and typically misaligned the affected surface by 1°. This produced a complementary bevel in the molded lens facet faces. The polishing step also slightly rounded the facet peaks on the tool, resulting in rounded facet valleys on the lens.

The facet peak radii on these lenses were again in the 0.008- to 0.012-in. range. This suggested that there might be a problem with the valley radii on the tool, rather than with the molding parameters, as had been previously assumed. A section of the faceted surface of the tool was obtained from the molder. This segment had been cut from the tool after the facets were turned, to obtain the square lens geometry. Examination of this part revealed that the tool facet valley radii were in fact 0.008- to 0.012-in. In addition, the surface finish on the unpolished facet faces was substantially rougher than had been anticipated.

4.5.1 Beveled Facet Faces

Light passing through the beveled area on the facet faces was not refracted through as large an angle as the light which passes through the

nonbeveled area. Therefore, this light falls outside of the target when it reaches the plane of the cell. This effect can be clearly seen by increasing the lens to target distances during sunlight testing. The amount of light striking the target cell increases as the lens to target distance increases, reaching a maximum at about 3/8 in. greater than the design distance. This occurs because the greater lens to target distance allows the light passing through the beveled areas of the facet faces to reach the target, while the correctly aimed light from the nonbeveled areas does not diverge far enough to miss the target. This effect is diagrammed in Figure 4.10. Using square target cells 2 cm on a side and a lens to cell distance of 13.7 in., lens efficiencies in the 85-percent range have been measured.

4.5.2 Tool Fabrication Options

In order to determine if the molding tool could be corrected, a survey of tool manufacturing methods and the tolerances these produce was made. The following information was obtained:

- Conventional lathe turning can achieve extremely sharp facet peak radii (0.0005 in.), and facet valley radii down to about 0.002 in., in a suitable material, such as 17-4 PH. Surface finishes in the 16 to 32 micro in. range can be obtained, with 24 micro in. being a reasonable target. This surface is suitable for polishing. The carbide tool used to turn stainless steel for the mold can not tolerate interrupted cuts.
- Grinding can produce peak radii similar to lathe turning, although a great deal of wheel redressing is required to obtain sharp valley radii of 0.005 in. Grinding produces a surface finish in the 8 to 24 micro in. range, but this still requires polishing to achieve a No. 1 mold finish suitable for optical components.

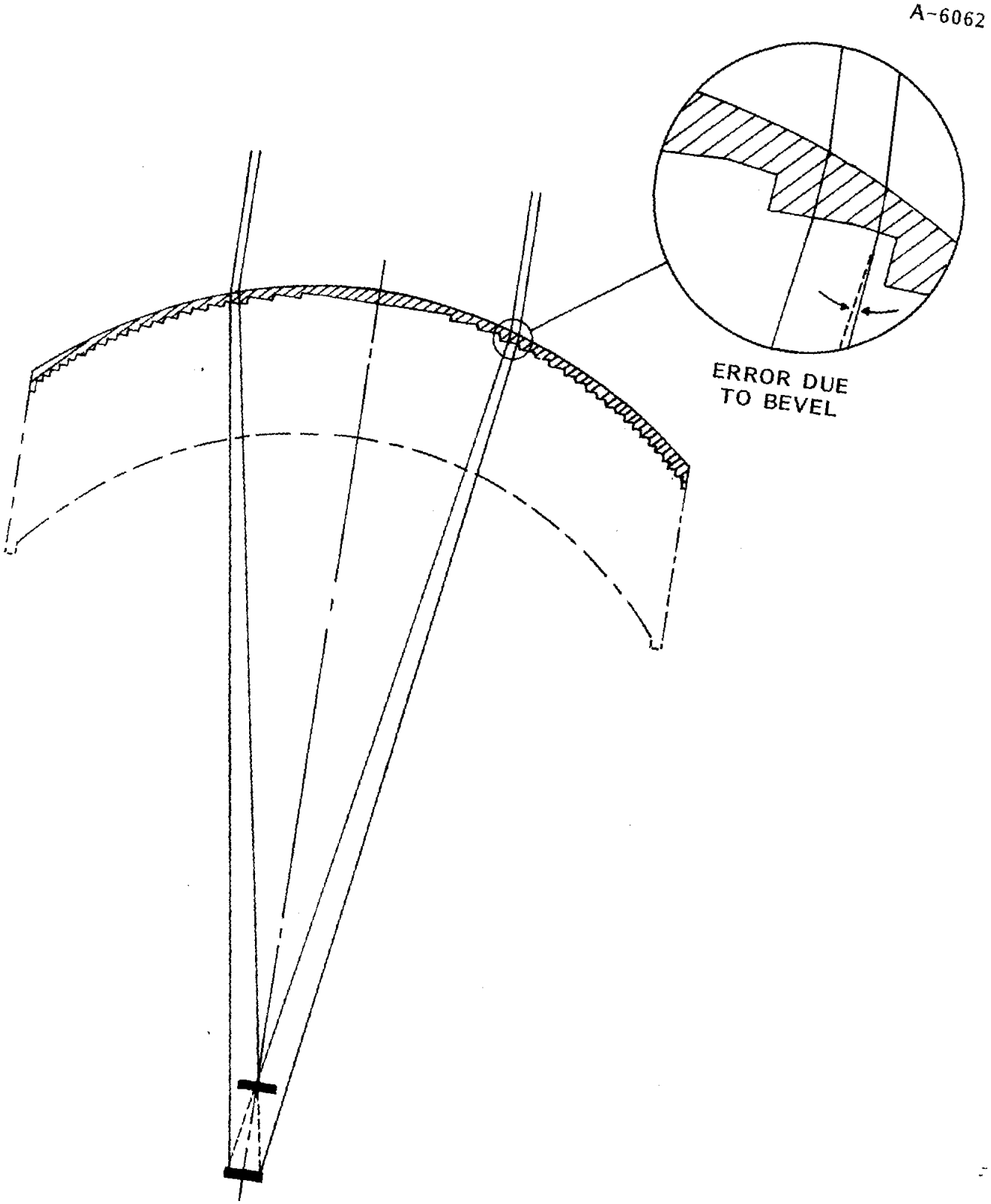

Figure 4.10 The Effect of Beveled Facet Faces

- Polishing procedures using 1.0 micron diamond can obtain a No. 1 mold finish, but care is required to preserve the original geometry of the tool.
- Diamond turning in certain nonferrous materials can achieve sharp facet peak radii (0.0005 in.), and valley radii in the 0.001-in. range. This process produces a surface finish which requires no further polishing, however, it is expensive and there are weight and size limitations on the available machines.

We concluded that the performance loss of the lenses was caused by the following:

- The tool was not turned from the most suitable material (420 stainless steel was used).
- The turning process was not performed as carefully as it should have been. This resulted in rounded facet valleys and a poor surface finish.
- The poor surface finish required too much of the subsequent polishing step, which resulted in the beveling of the tool facet faces and the rounding of the tool facet peaks.

We also felt that beveling of the tool surface could be eliminated if a lap polishing technique was used.

4.6 TEST TOOL

The validity of this information was tested by fabricating a sample tool at our in-house machine shop facility. A four piece faceted "test tool" was produced. Using conventional lathe turning techniques and 17-4 PH stainless steel stock, facet peak radii less than 0.0005 in. and facet valley radii of 0.0025 in. were achieved. The surface finish was 26 micro in. Subsequent heat treating increased the tool hardness to 42-46 on the Rockwell C scale. The configuration of the test tool is indicated in Figure 4.11.

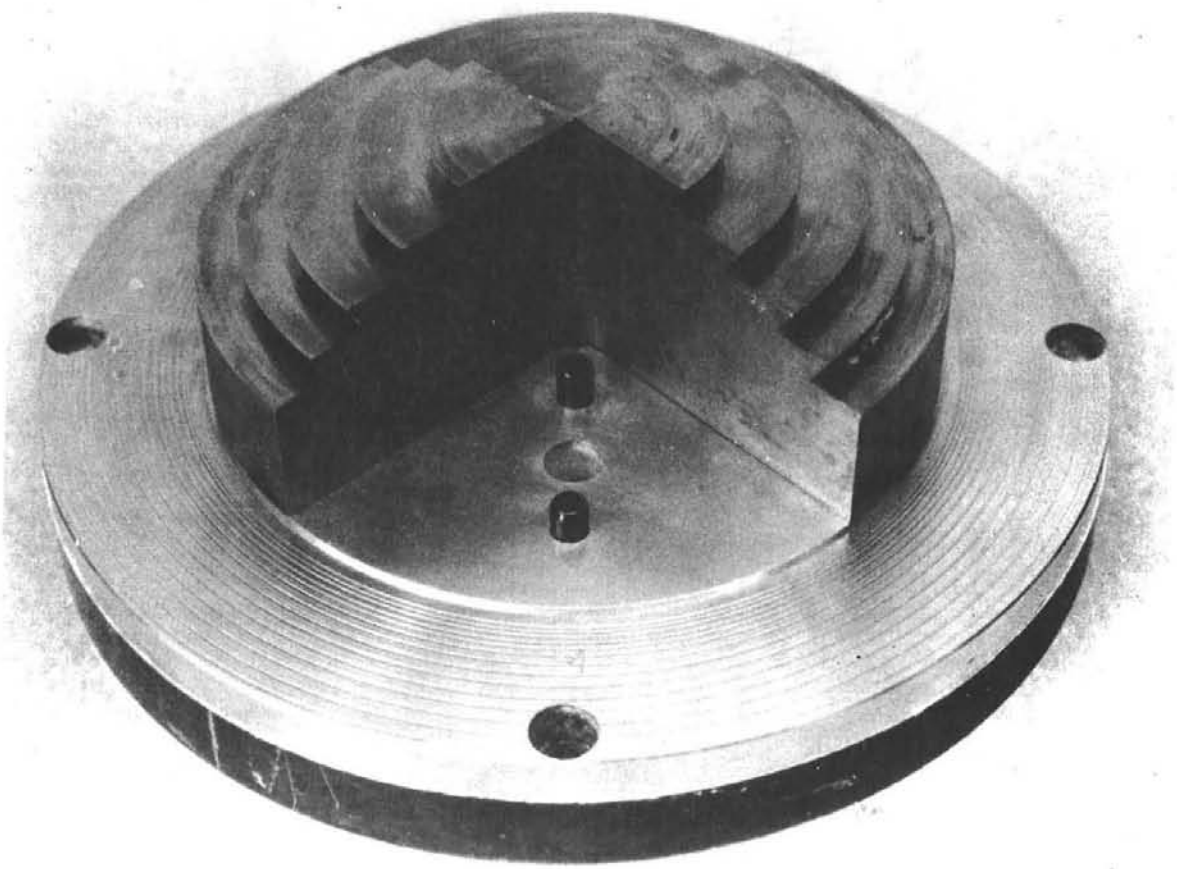

Figure 4.11 Test Tool

A cast lap polishing technique was designed to preserve the tool geometry during the polishing step. A reaction curing compound was cast against the tool to form the lap. The tool was mounted on a rigid turntable which could be made to rotate through a limited arc in both directions. The lap was clamped in a stationary position with its faceted surfaces contacting the facets on the tool. Polishing was effected by drip-feeding an abrasive slurry into the contact area while rotating the tool back and forth against the fixed lap. Several rigid and resilient materials were used to form laps. These are shown in Figure 4.12.

This process was partially successful in that it did remove material while maintaining the geometry of the test tool. Both facet peaks and valleys remained sharp. An optical polish was not achieved, however, possibly because the polishing motion was parallel to the machining marks left on the tool by the lathe turning. It is anticipated that an optical polish could be attained by adding a radial motion component to the lap during the polishing process.

4.7 INJECTION MOLDING TOOL REWORK

The injection molding tool was ground to restore the original flat facet face geometry, and to improve the tool facet peak and valley radii. A short run of lenses was produced on this unpolished tool. The lenses exhibited flat facet faces, sharp facet valley radii, and improved facet peak radii in the 6- to 12-mil range.

The tool was then repolished using a technique which provided additional support for the polishing tools.

4.8 FINAL RESULTS

The efficiency of lenses produced on the ground/polished tool has been measured at 72 percent for the design condition (0.37-in. square cell at a lens-to-cell distance of 13.37 in.), and in the 85- to 87-percent range for a larger cell 1.55 cm in diameter at lens-to-cell distances of 13.7 in.

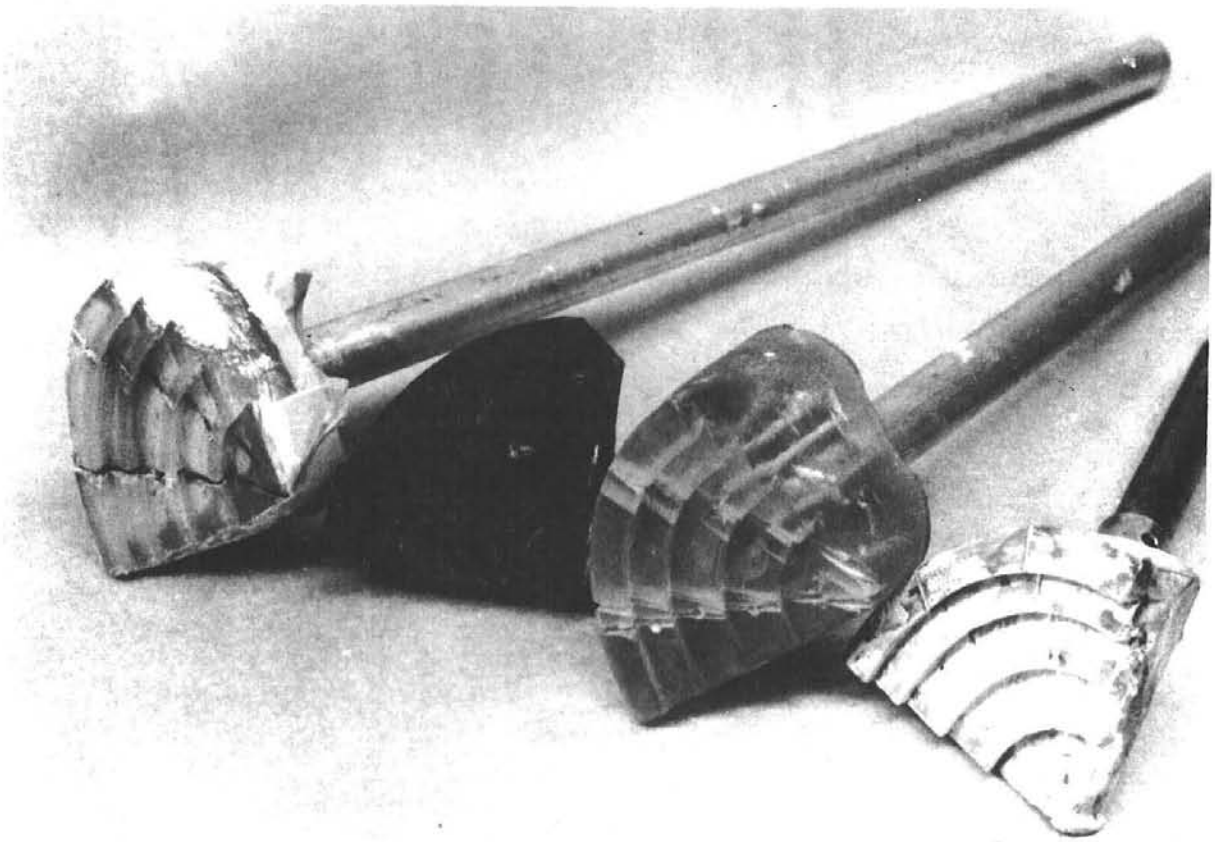

Figure 4.12 Laps

Results obtained at Sandia's point focus Fresnel lens test facility for the ground/polished lens are indicated in Figures 4.13, 4.14, 4.15, and 4.16. Note that these results are for the design target size at the design lens-to-cell distance.

Analyses of these lenses indicate that there is still considerable room for improvement in the configuration of the injection molding tool. Although the molded lenses are replicating the tool with great fidelity, they exhibit many non-flat areas on the facet faces, and considerable rounding of the facet peaks and valleys. Each of these areas could be improved with increased care in the fabrication of the tool, or the use of a more appropriate tool manufacturing process such as diamond turning.

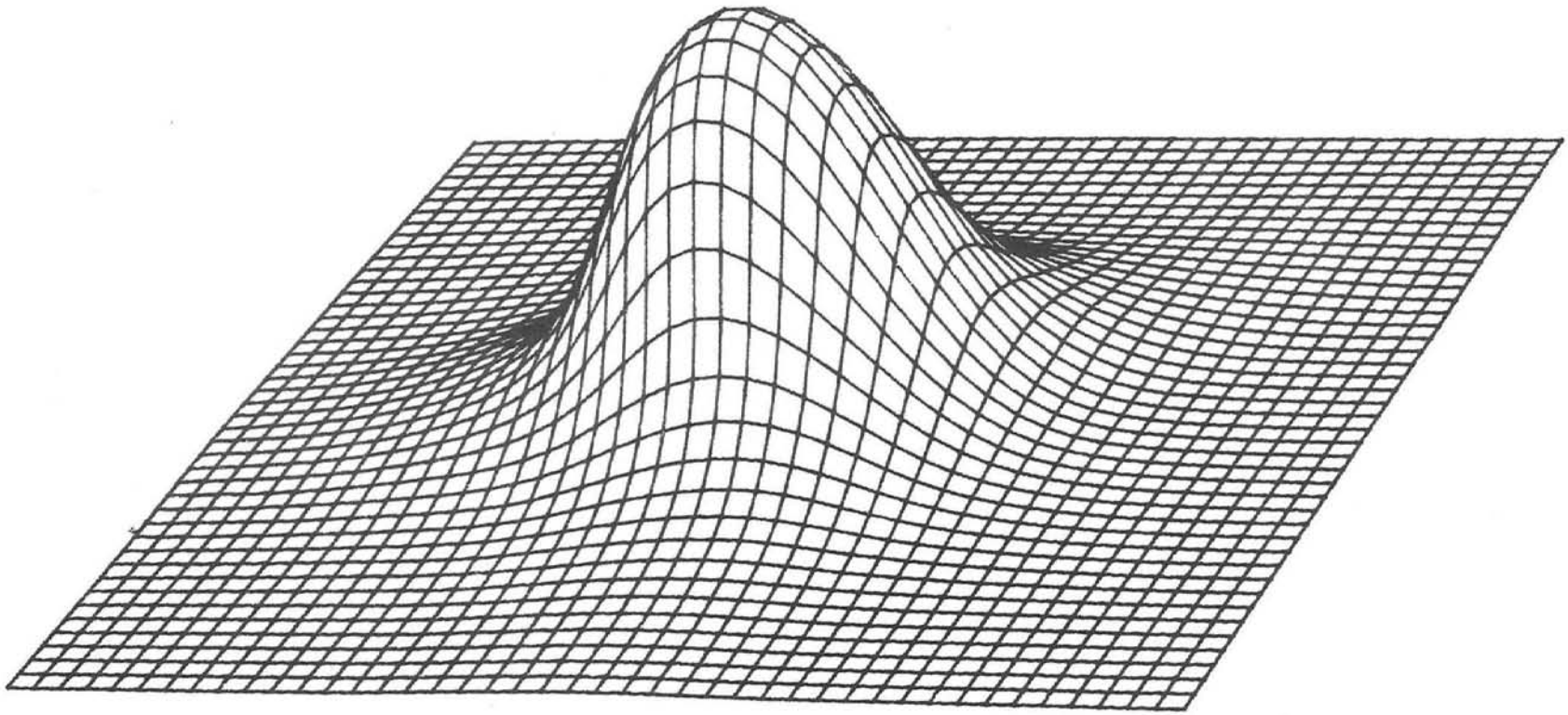

3-D PLOT OF FILE TEL10

El = 25 Az = 25

Scan Efficiency = 74.17%

Figure 4.13 Sandia Test Results for the Ground/Polished Lens

A-6102

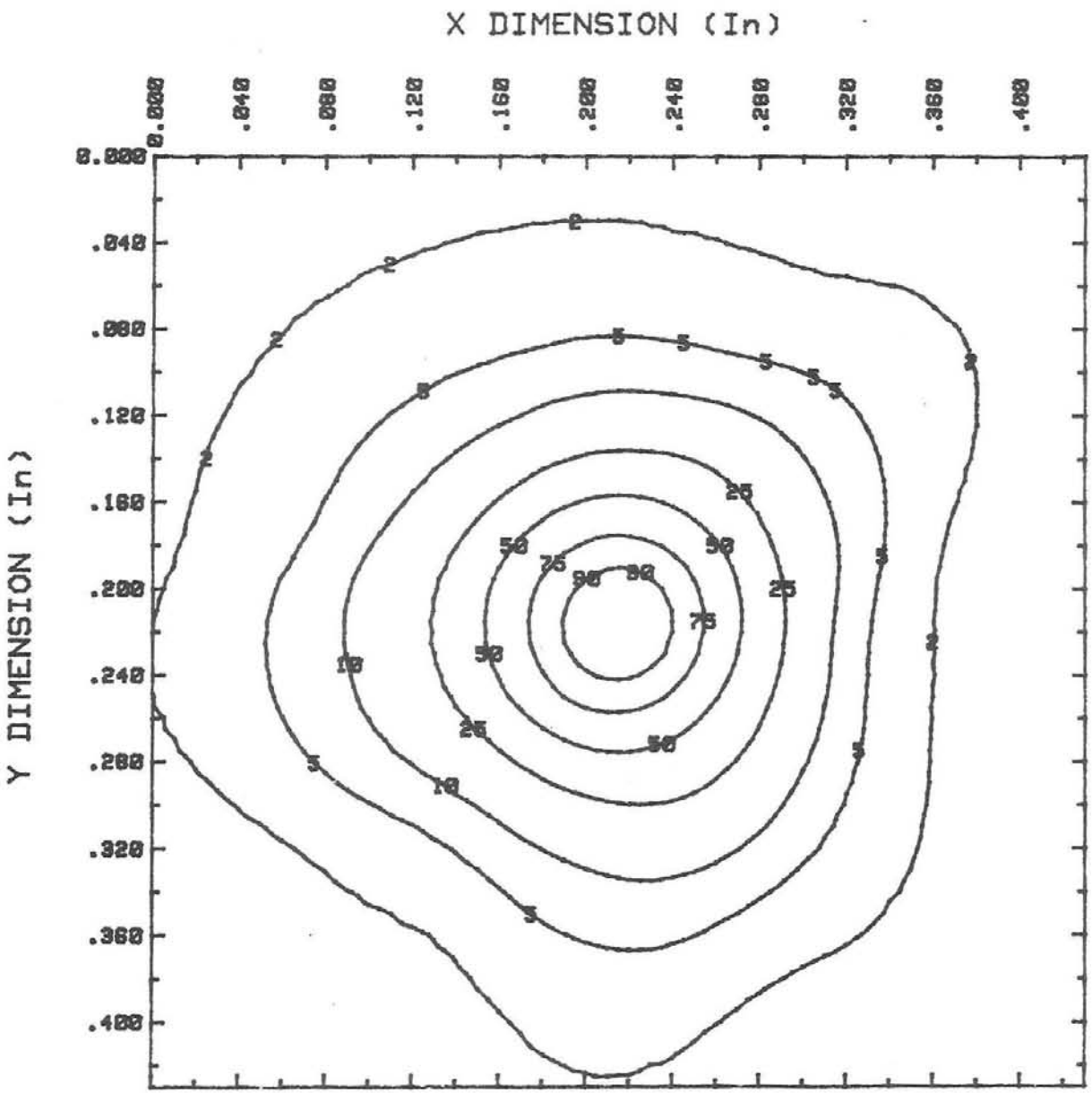

PLOT OF CONTOURS(%):
2
5
10
25
50
75
90

OF FILE TEL10

Image dimensions =
.37, .37
Lens Efficiency =
72.34%

Scan efficiency =
74.17%

Figure 4.14 Sandia Test Results for the Ground/Polished Lens

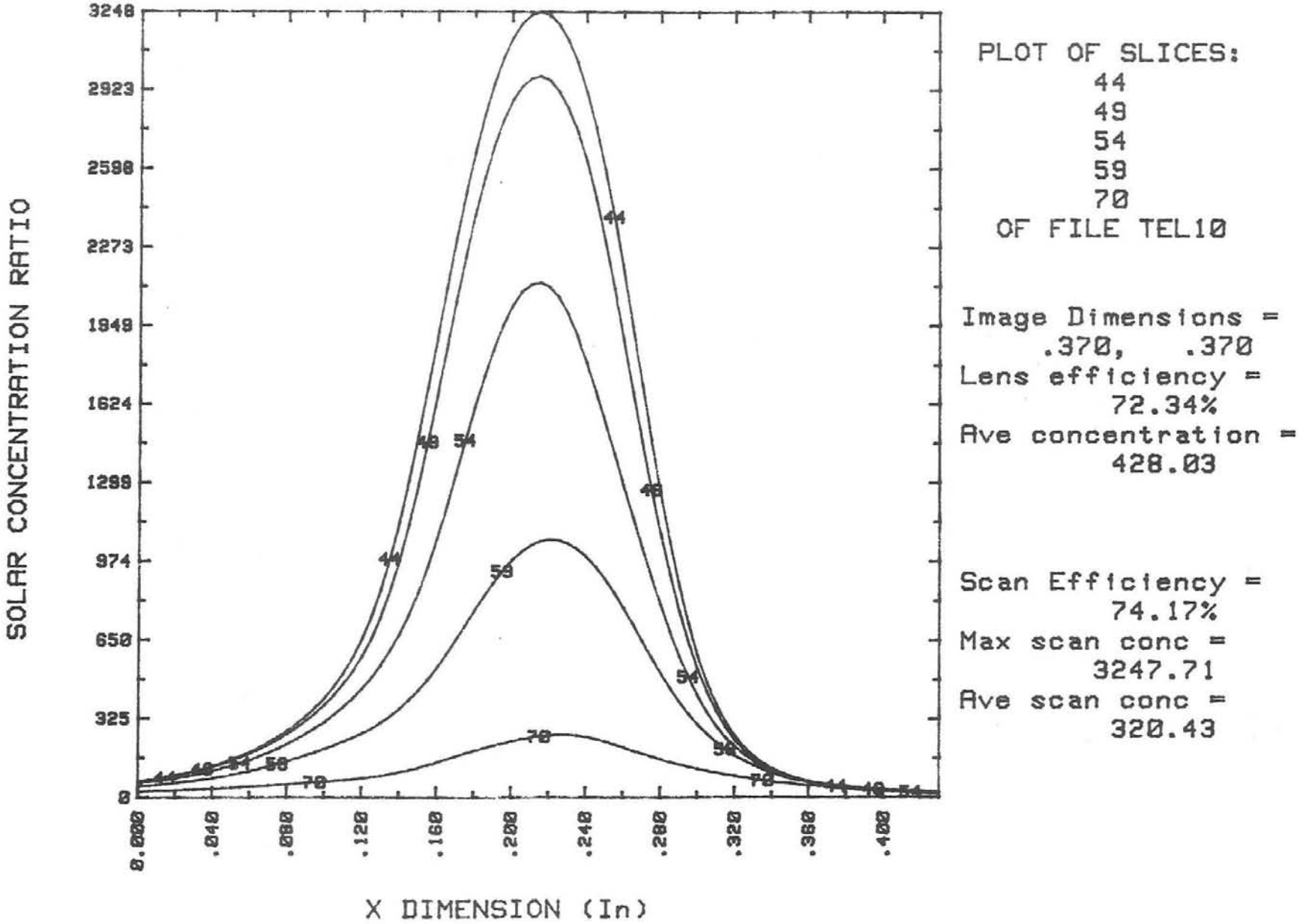

Figure 4.15 Sandia Test Results for the Ground/Polished Lens

A-6104

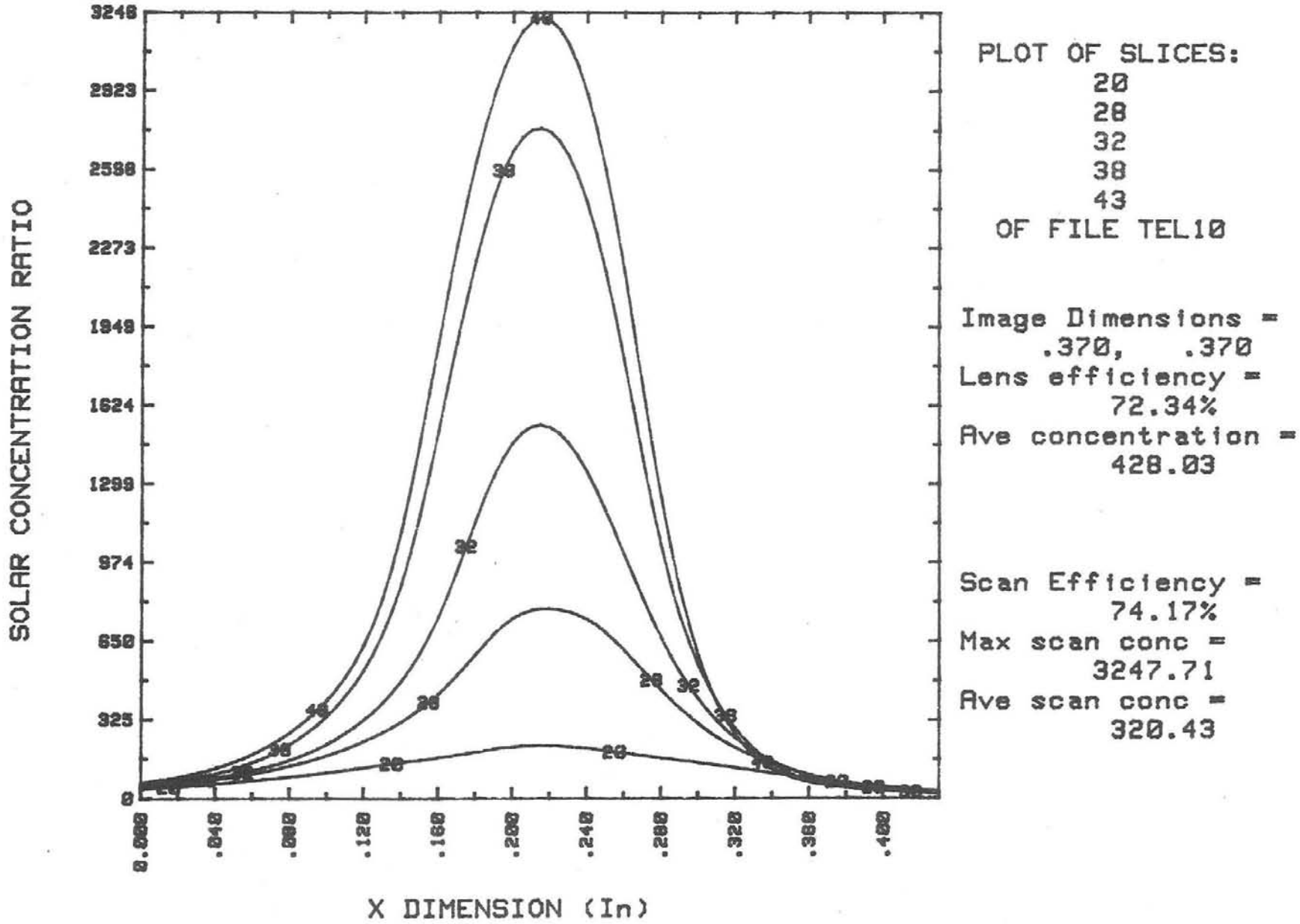

Figure 4.16 Sandia Test Results for the Ground/Polished Lens

5. CELL DESIGN AND FABRICATION

Microwave Associates was responsible for the design and fabrication of the etched, multiple vertical junction (EMVJ) cells. Their final report can be found in Appendix 1. Planar junction cells were obtained from Applied Solar Energy Corporation (ASEC). Test results for these cells can be found in Chapter 10.

6. CELL COOLING

Several techniques including both active and passive heat transfer methods were investigated during the program. Two of the active cooling designs were fabricated and tested to provide validation of the design methodology. The active techniques analyzed included two which employed turbulent flow and two which employed laminar flow. Manufacturing methods to produce the heat sinks were investigated for those designs which employed unusual geometries. A passive heat sink design was generated based upon minimizing the cost of energy delivered on an annual basis. Data from Typical Meteorological Year (TMY) weather tapes were used in the analysis. The active heat sink designs were based upon minimizing the cost per unit of power under typical direct insolation conditions.

The achievement of either of the design criteria demands that the cell cooling result in low cell to coolant temperature differences, low material cost, and low pumping losses for active systems. The heat flux for the designed cell operating at 850 kW/m^2 direct insolation and a lens efficiency of 85 percent is approximately 105,000 $Btu/hr\text{-}ft^2$ (330,000 W/m^2). This is a flux comparable to that of a furnace. The requirement for a high film coefficient to lower the cell/coolant temperature difference can be reduced by increasing the surface area available to the coolant. The techniques for achieving both increased surface areas and moderately high film coefficients are explored in detail in the following sections. Heat transfer involving two-phase flow was not investigated in detail due to the difficulty in maintaining the required pressure and temperature conditions over an array for the variety of applications in which the heat can be utilized. The coolant properties for the active cooling systems correspond to a 40% propylene glycol/60% water mixture at 120°F.

6.1 JET IMPINGEMENT HEAT SINK

Cell cooling by the impingement of one or multiple fluid jets on a heat sink was examined for the configuration shown in Figure 6.1. The use of a heat sink below the cell provides improved cooling with a reduced requirement for a high film coefficient. The heat sink size and intercell tubing size were optimized for several jet diameters at each of several flow rates. The results from the analytic model are shown in Figure 6.2.

A particular jet configuration was selected for experimental verification. The predicted values are shown in Figure 6.3, along with the measured values obtained during the experiments. Note that data in Figure 6.3 are based upon a lower heat input than the data of Figure 6.2. The experimental apparatus is shown disassembled in Figure 6.4, assembled in Figure 6.5, and under test in Figure 6.6. The heat input was delivered through an electric resistance heater pressed into a copper cone, which is in turn soldered to the heat sink. A square of aluminum, which was plated to allow soldering, was placed between the copper cone and the copper heat sink to simulate the BeO ceramic insulator that would be present in the cell package. The diameter of the copper cone at the interface surface was 0.18 in., which represents the approximate size of the expected light spot on the surface of a Microwave Associates' cell. Thermocouples were placed in the copper cone and at various distances from the jet center to allow correlation between measured and predicted values. Agreement between the predicted and measured values for cell temperature rise was excellent, as shown in Figure 6.3.

6.2 FINNED HEAT SINK

The finned heat sink design utilizes closely spaced fins to achieve a high film coefficient under laminar flow conditions. The fins provide an extended surface allowing the size of the heat sink to be reduced which decreases the temperature loss through the heat sink material.

A-6060

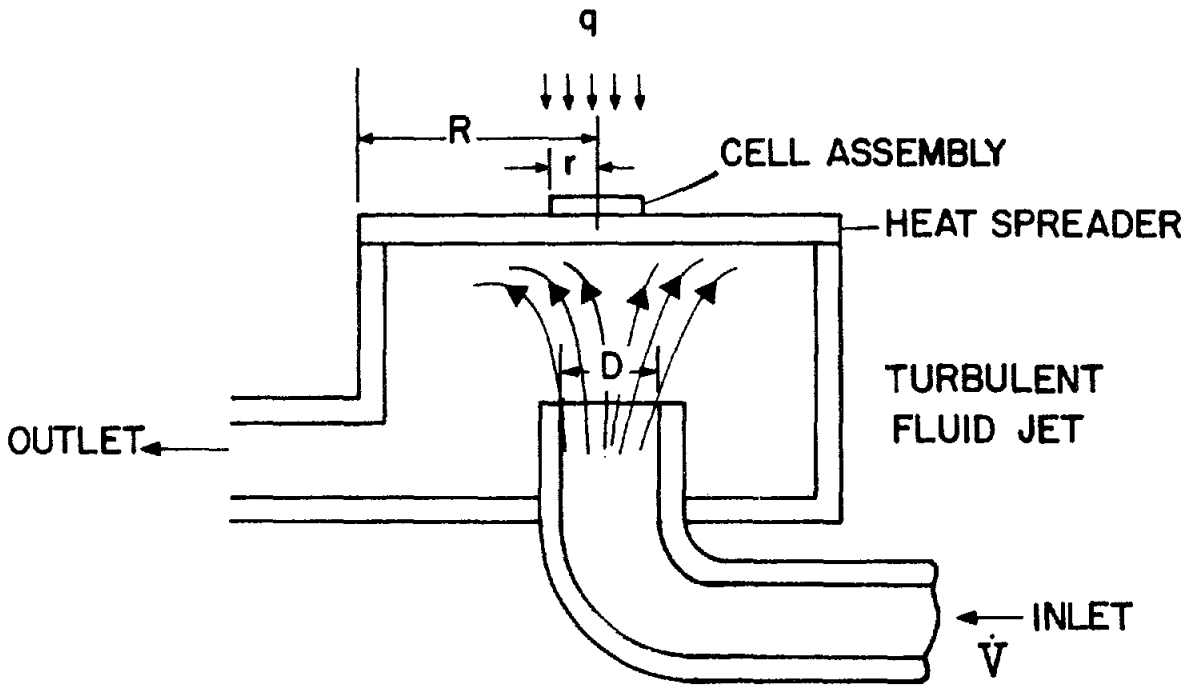

Figure 6.1 Jet Impingement Model

A-6056

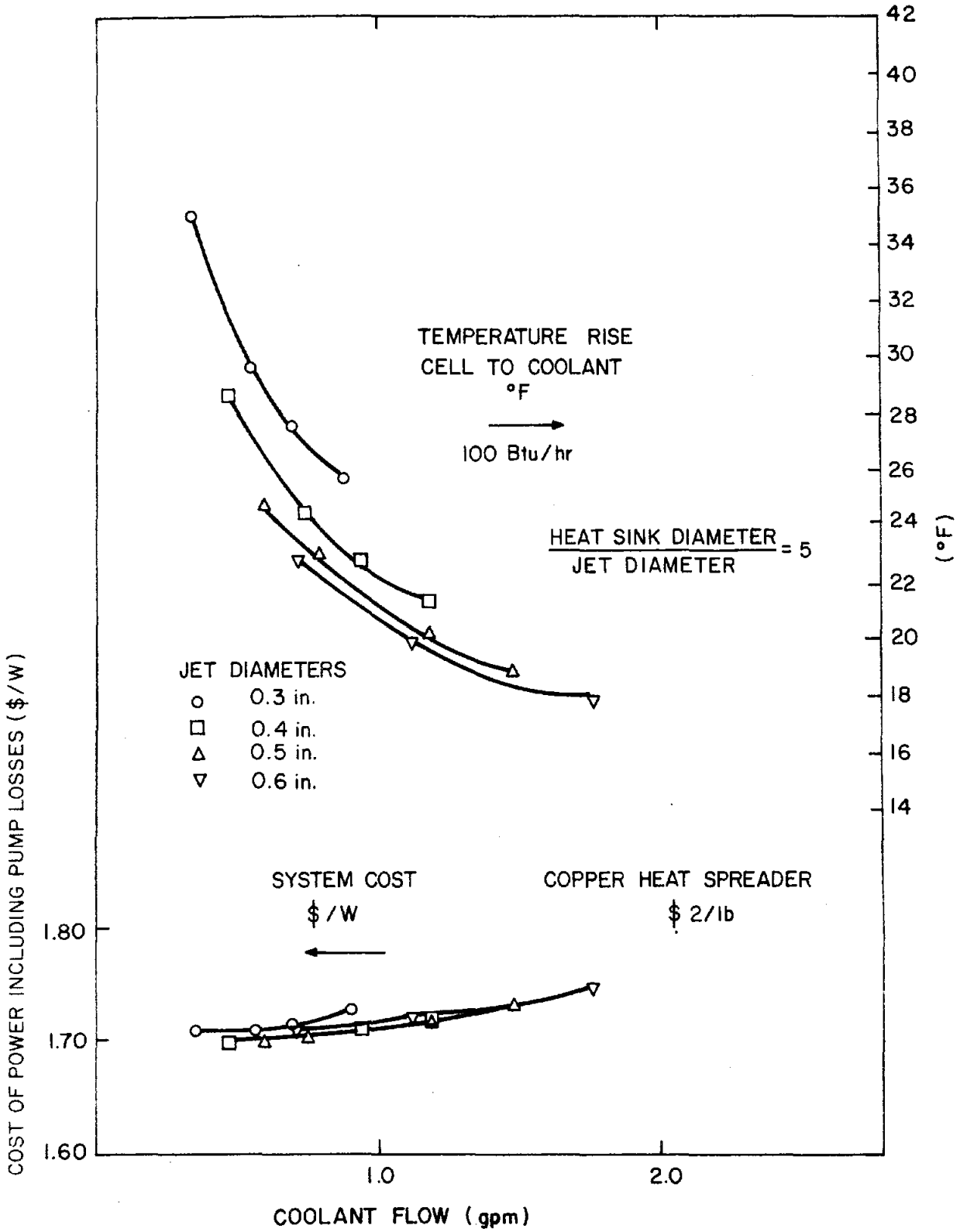

Figure 6.2 Jet Impingement Cell Heat Transfer

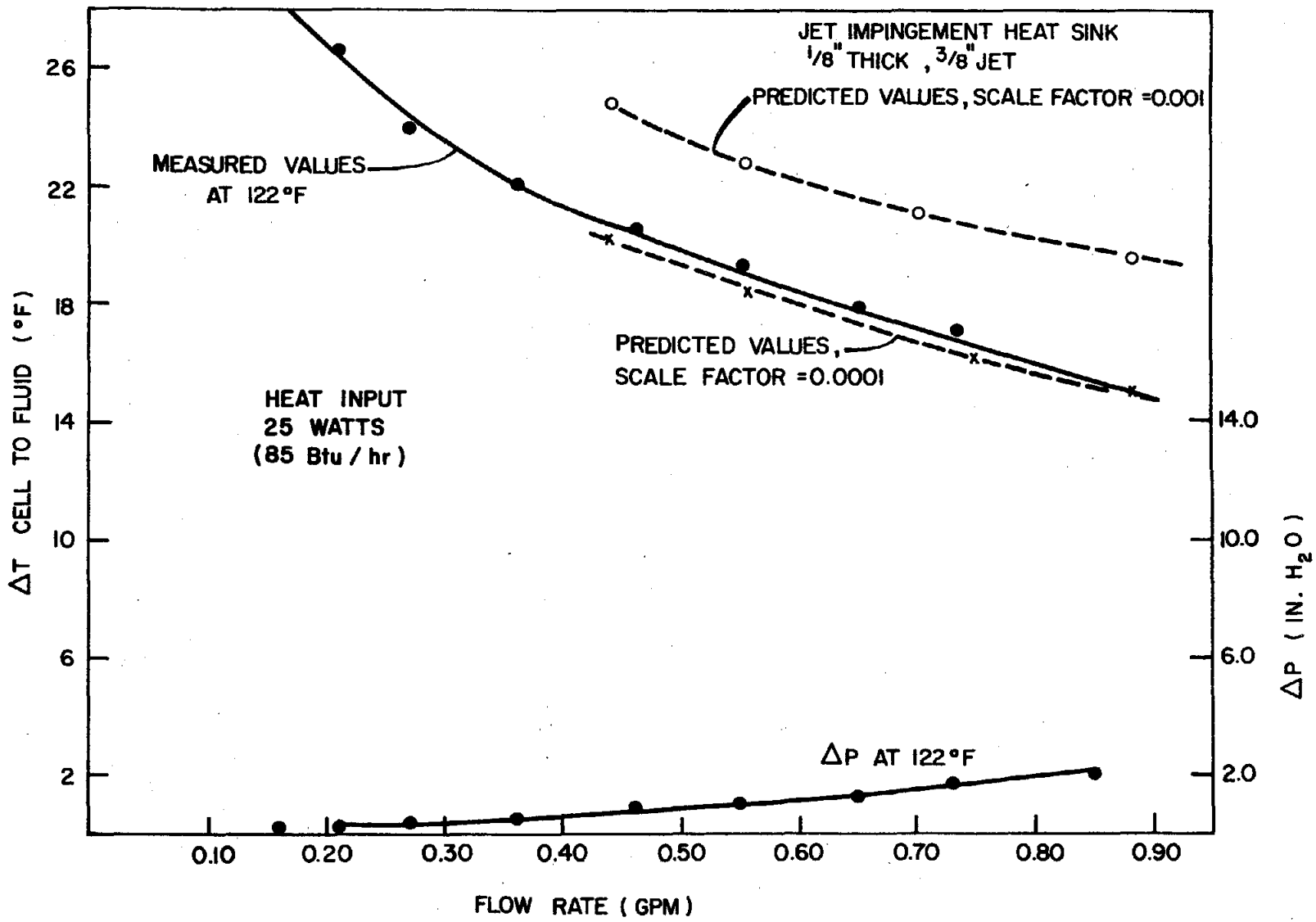

Figure 6.3 Jet Impingement Experimental Results and Predicted Values

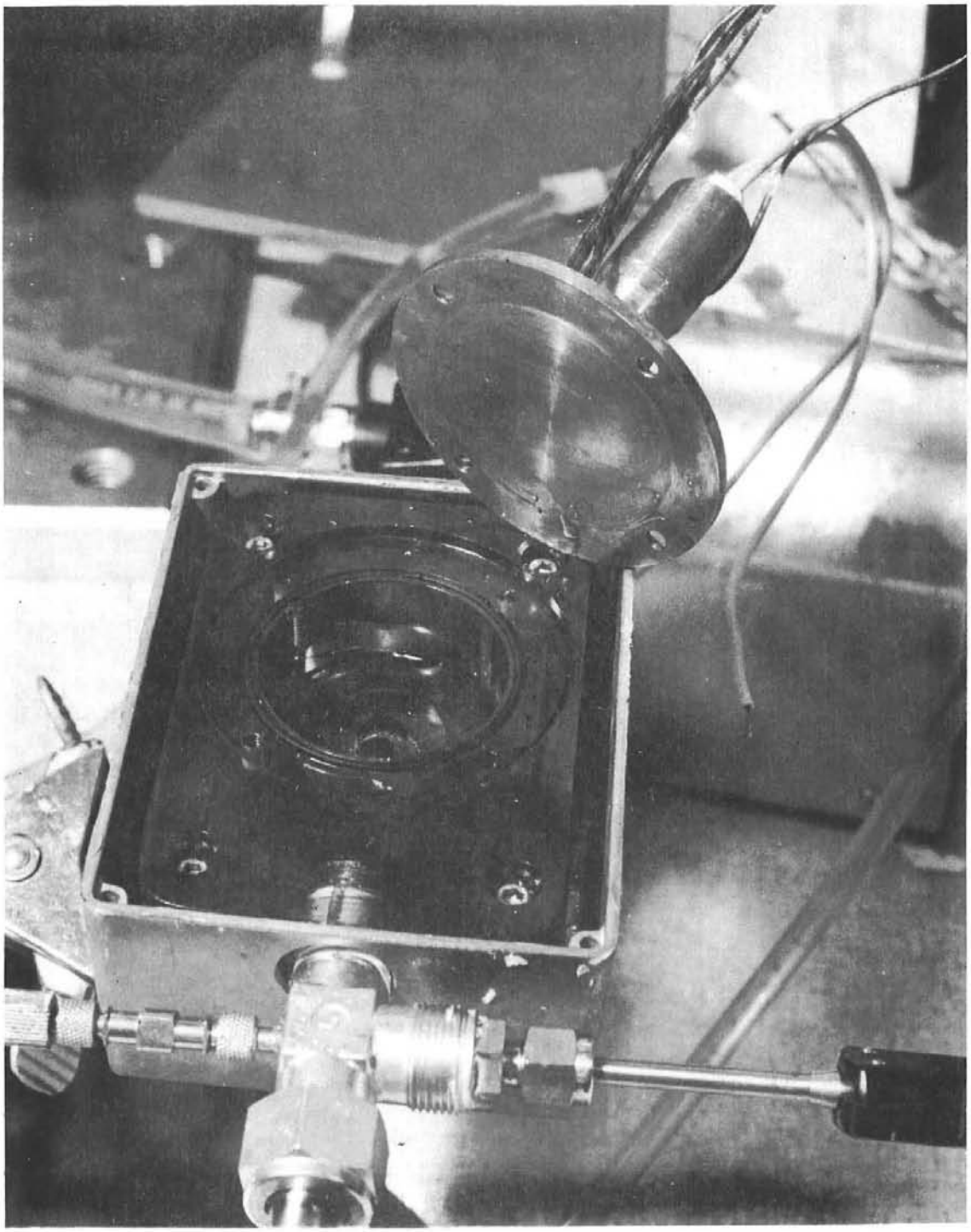

Figure 6.4 Jet Impingement Apparatus (View 1)

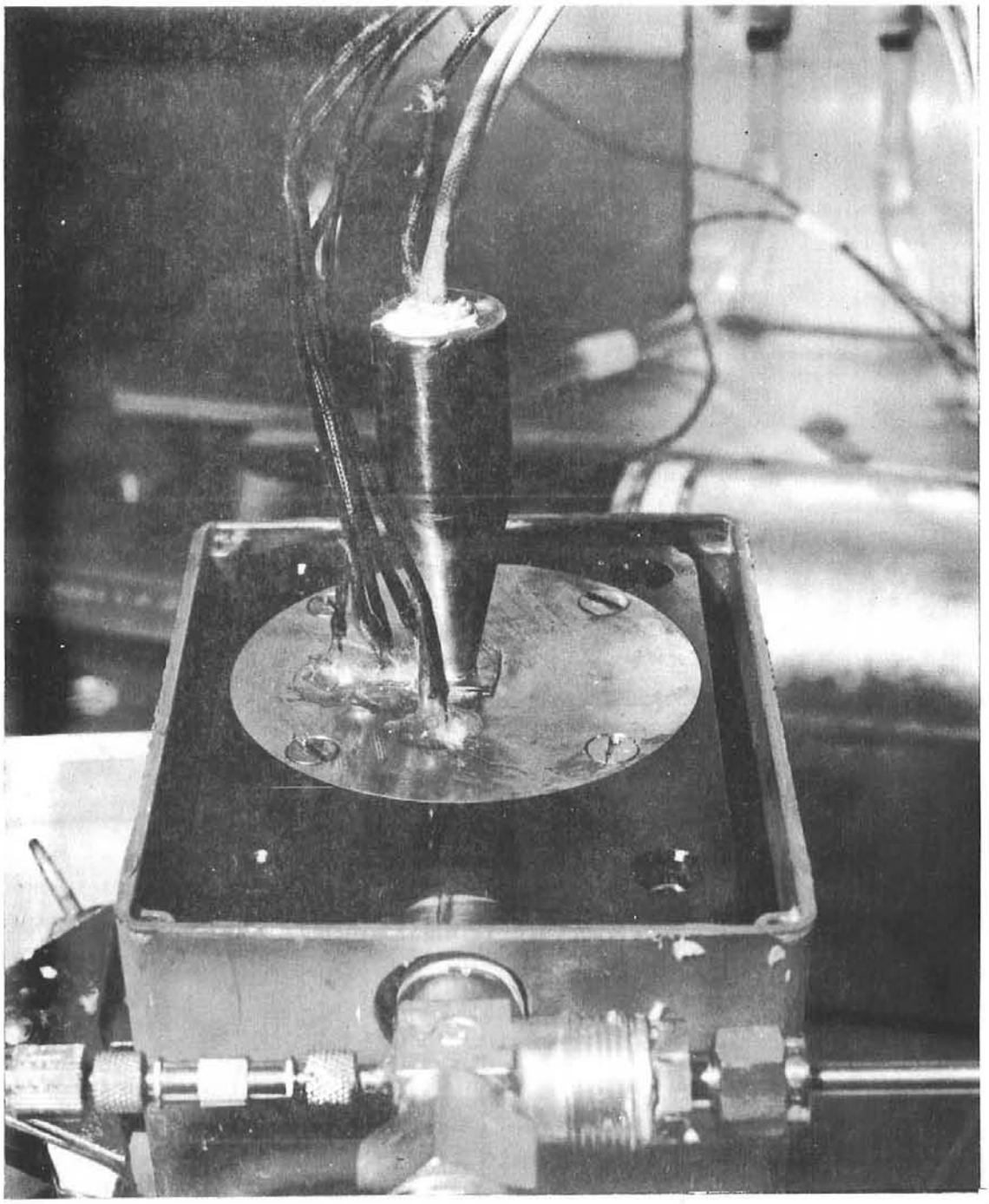

Figure 6.5 Jet Impingement Apparatus (View 2)

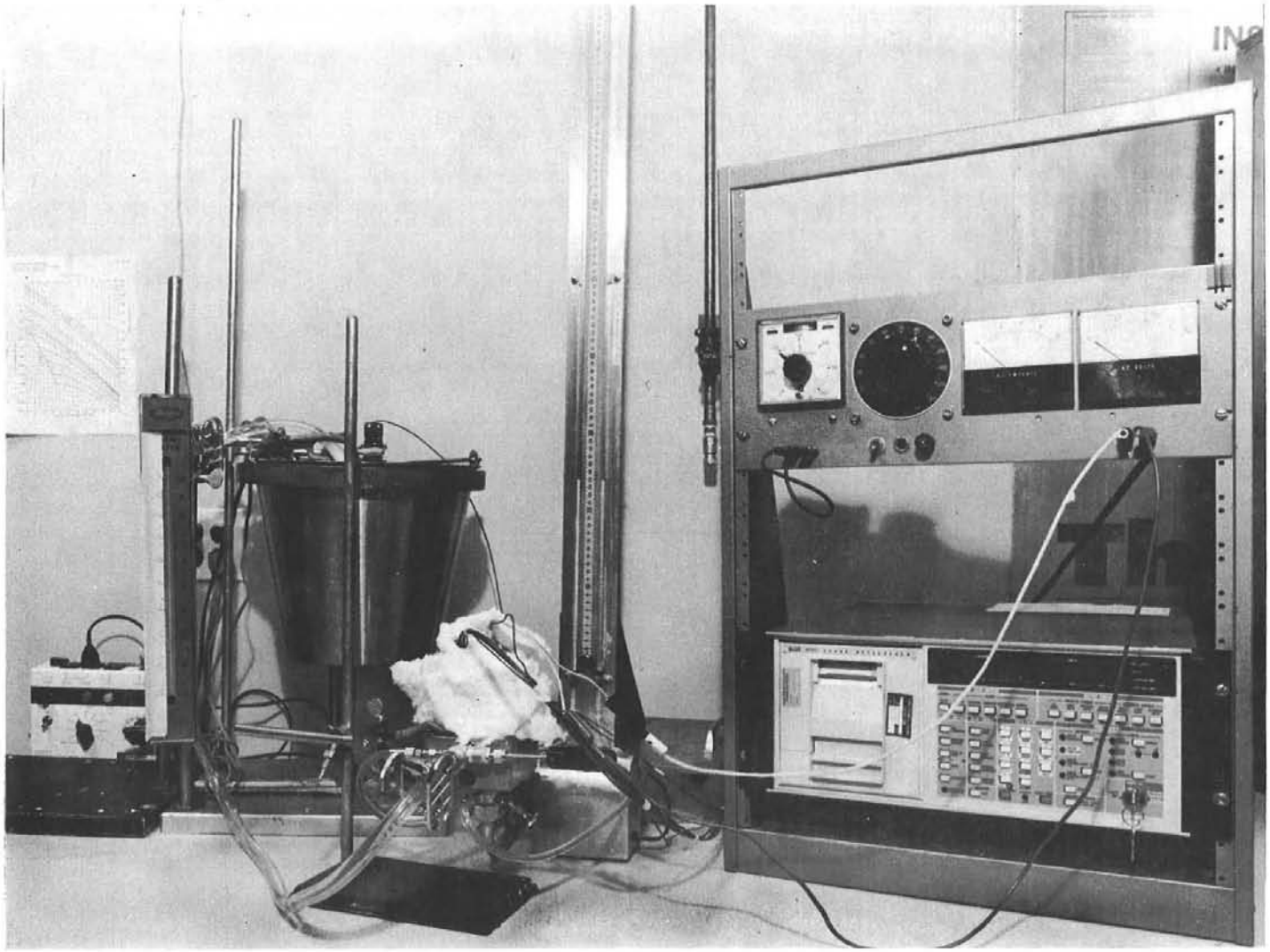

Figure 6.6 Jet Impingement Apparatus (View 3)

Both copper and aluminum heat sinks were designed. The advantage of aluminum is lower material and fabrication costs since the heat sinks can be made using a profile extrusion process. The disadvantages of aluminum include the requirement of plating to allow lead/tin soldering and corrosion potential in the coolant loop.

The heat sink itself is optimized by varying the base thickness, fin thickness, fin height, number of fins, heat sink length for a given space between fins, coolant flow rate, and heat sink volume. The results for the analysis of a copper heat sink are shown in Figure 6.7. A higher material cost was assumed because of the more complex processing required to form the fins.

The geometry of the finned heat sink is determined in part by the constraint that the length/width ratio will result in equal temperature differences across the heat sink length and width. This serves to utilize the heat sink material in the most efficient manner. Based upon the notation in Figure 6.8, the temperature differences in the x and y direction are given by

$$\Delta T_x = Q \frac{l_x}{K A_x} \text{ and } \Delta T_y = Q \frac{l_y}{K A_y} .$$

Since these temperature differences are equal

$$\frac{l_x}{l_y} = \frac{A_x}{A_y} = \frac{t_f h_f + l_y t_b}{l_x t_b}$$

or

$$\frac{l_x}{l_y} = \sqrt{1 + \frac{t_f h_f}{t_b l_y}} .$$

The heat sink design length-to-width ratio was constrained at a value that provided near optimum performance while heat sink volume was varied. The effects of adjusting the length/width ratio about this value were later examined and found to be minor.

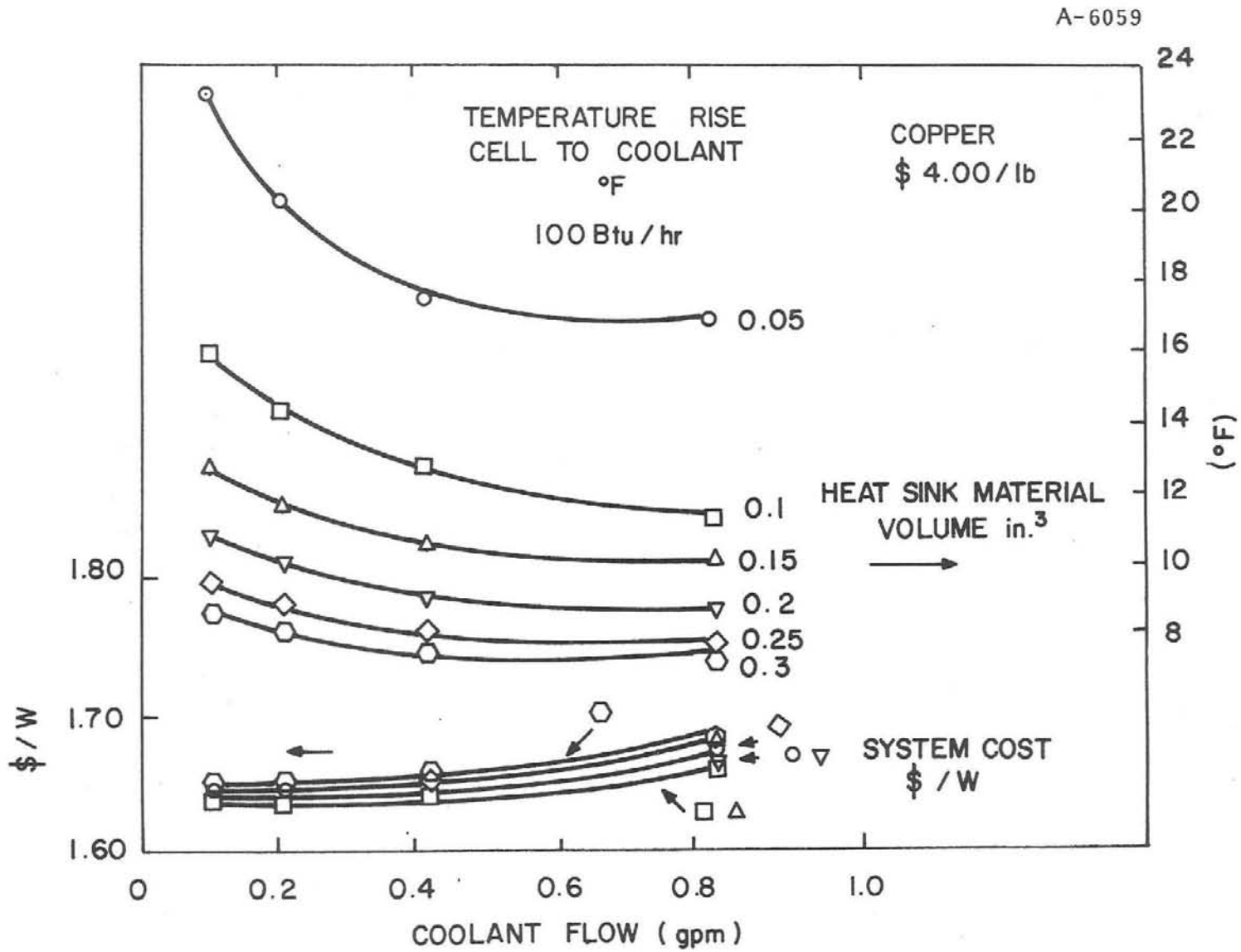

Figure 6.7 Finned Heat Sink Cell Heat Transfer

A-6063

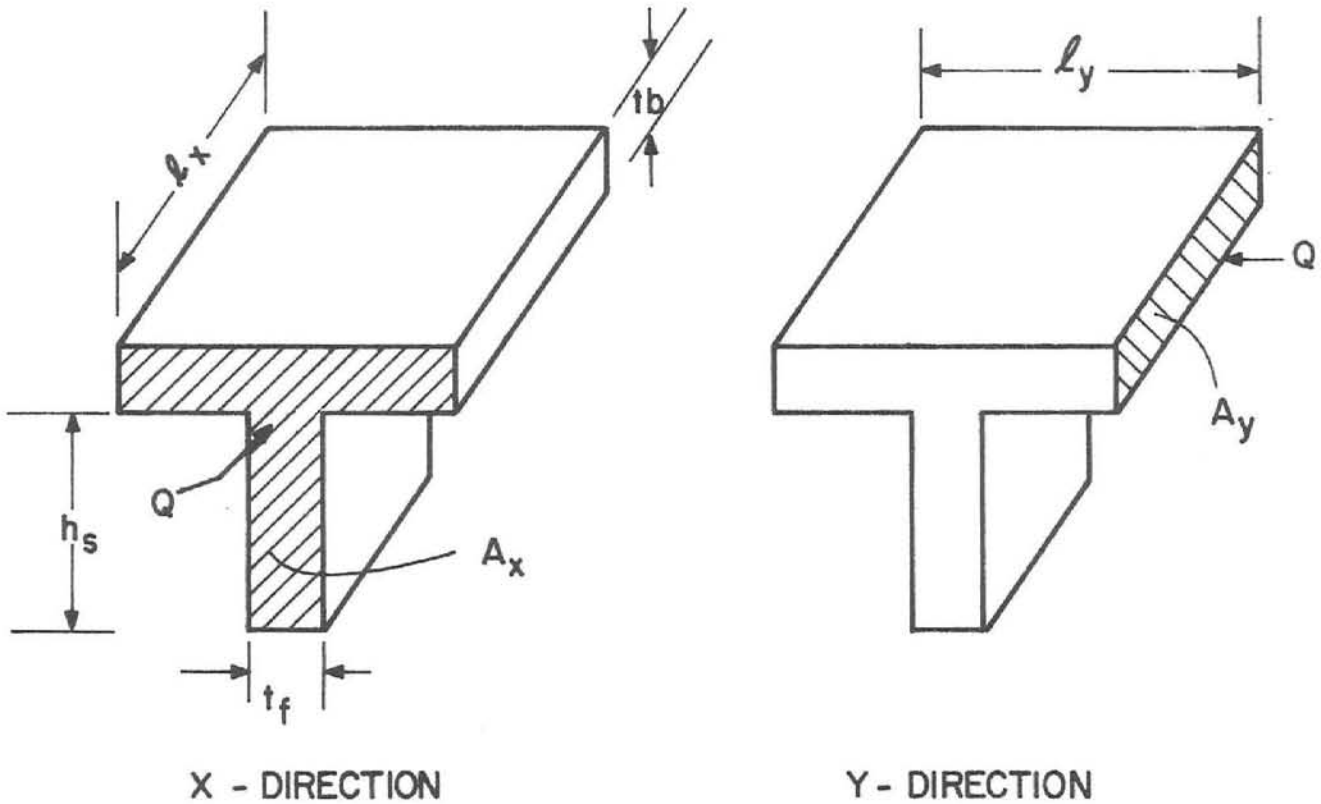

Figure 6.8 Model of Finned Heat Sink

Prototype finned heat sinks were designed for both copper and aluminum. Both heat sinks were fabricated and are shown in Figure 6.9. The predicted performance and experimentally measured data are shown in Figure 6.10. Performance predictions were made for a fluid temperature of 120°F.

6.3 FLATTENED TUBE HEAT SINK

The concept of utilizing the high film coefficient obtainable in laminar flow, by spacing the walls close together, was extended to a geometry that will probably prove more cost effective in a production design. This geometry is that of a flattened tube, preferably with the walls bonded together in the center. Although this geometry will not provide as compact a heat sink as the one with fins, it is less complex and more readily produced.

The analytic design results for the flat tube heat sink are shown in Figure 6.11. Although the system costs appear to be slightly higher than those for the finned heat sink, the flat tube heat sink does not require a housing and the housing costs have not been included for the finned heat sink. One possible design option for the flat tube heat sink is shown in Figure 6.12.

6.4 ROUND TUBE HEAT SINK

A simple section of copper tubing can act as a heat spreader, and if sufficiently high film coefficients are achieved using turbulent flow, then the entire cell cooling system can consist of a single section of tubing, suitably bent to a serpentine configuration. Such a configuration does not allow for differential expansion between the module case and the heat sinks, therefore its application is limited to lower concentration ratios where the differential expansion can be tolerated. The analytic design results shown in Figure 6.13 assume that the heat from the cell is distributed uniformly around the tube. This assumption can

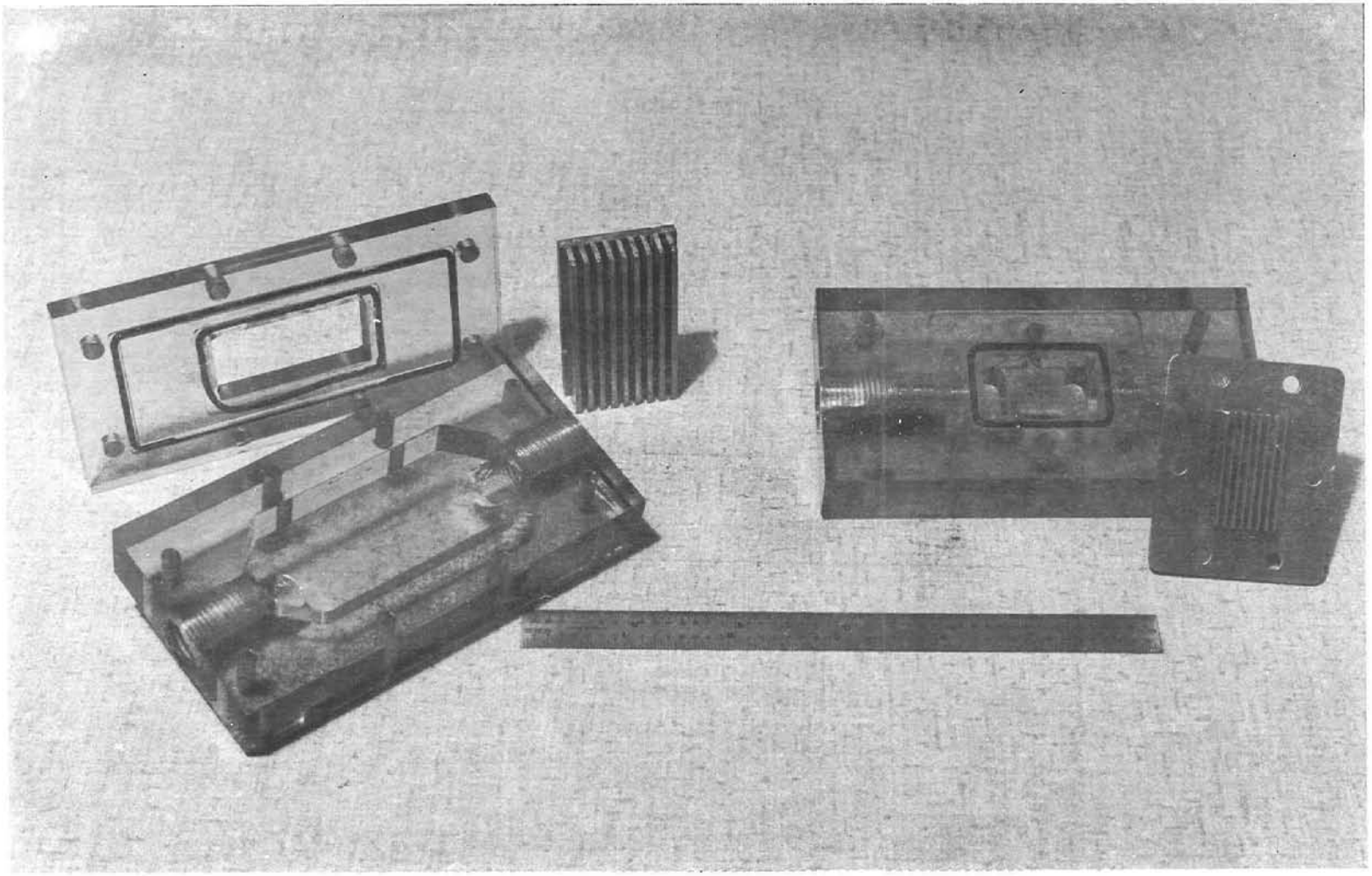

Figure 6.9 Finned Heat Sink

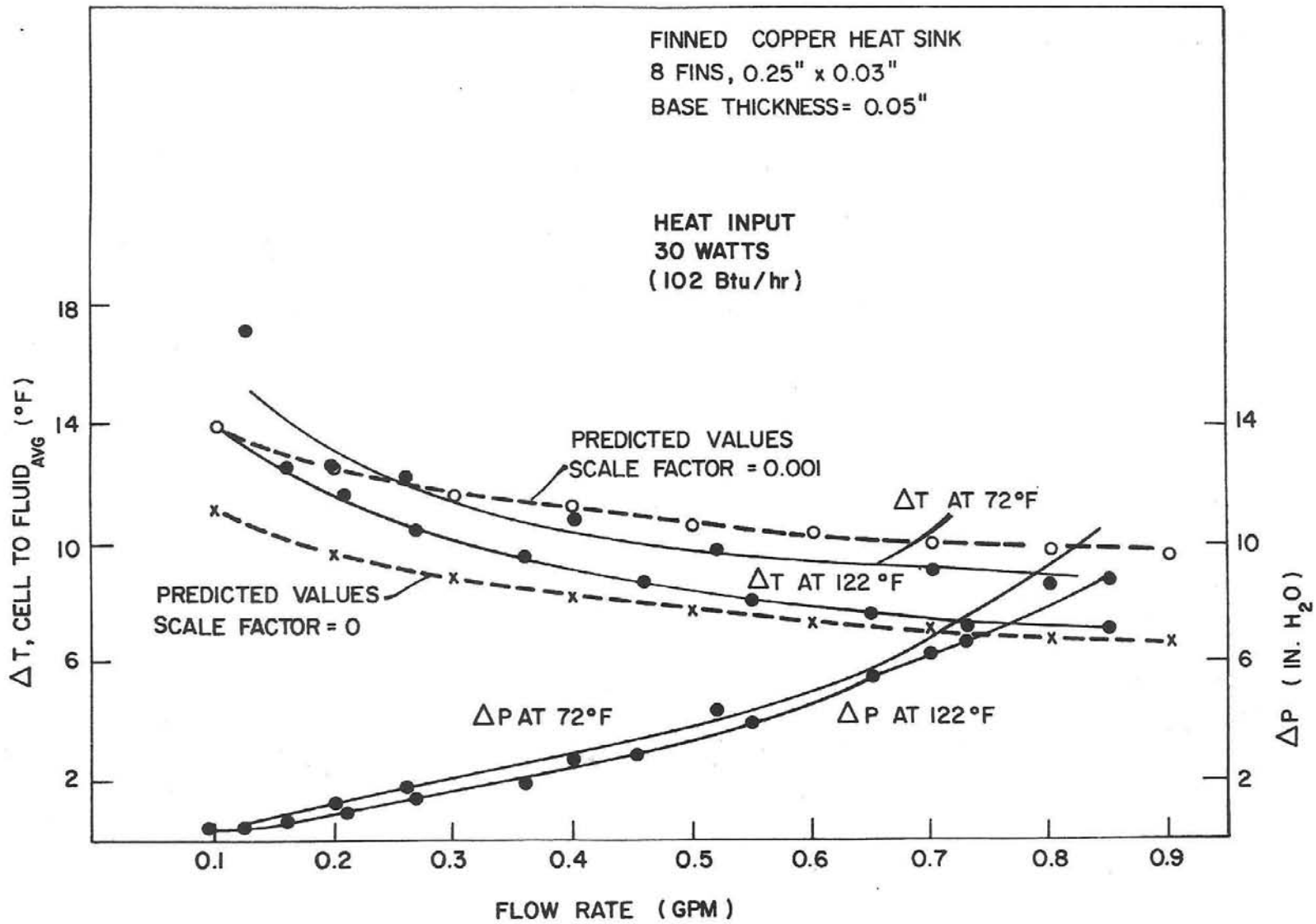

Figure 6.10 Finned Heat Sink Experimental Results and Predicted Values

A-6054

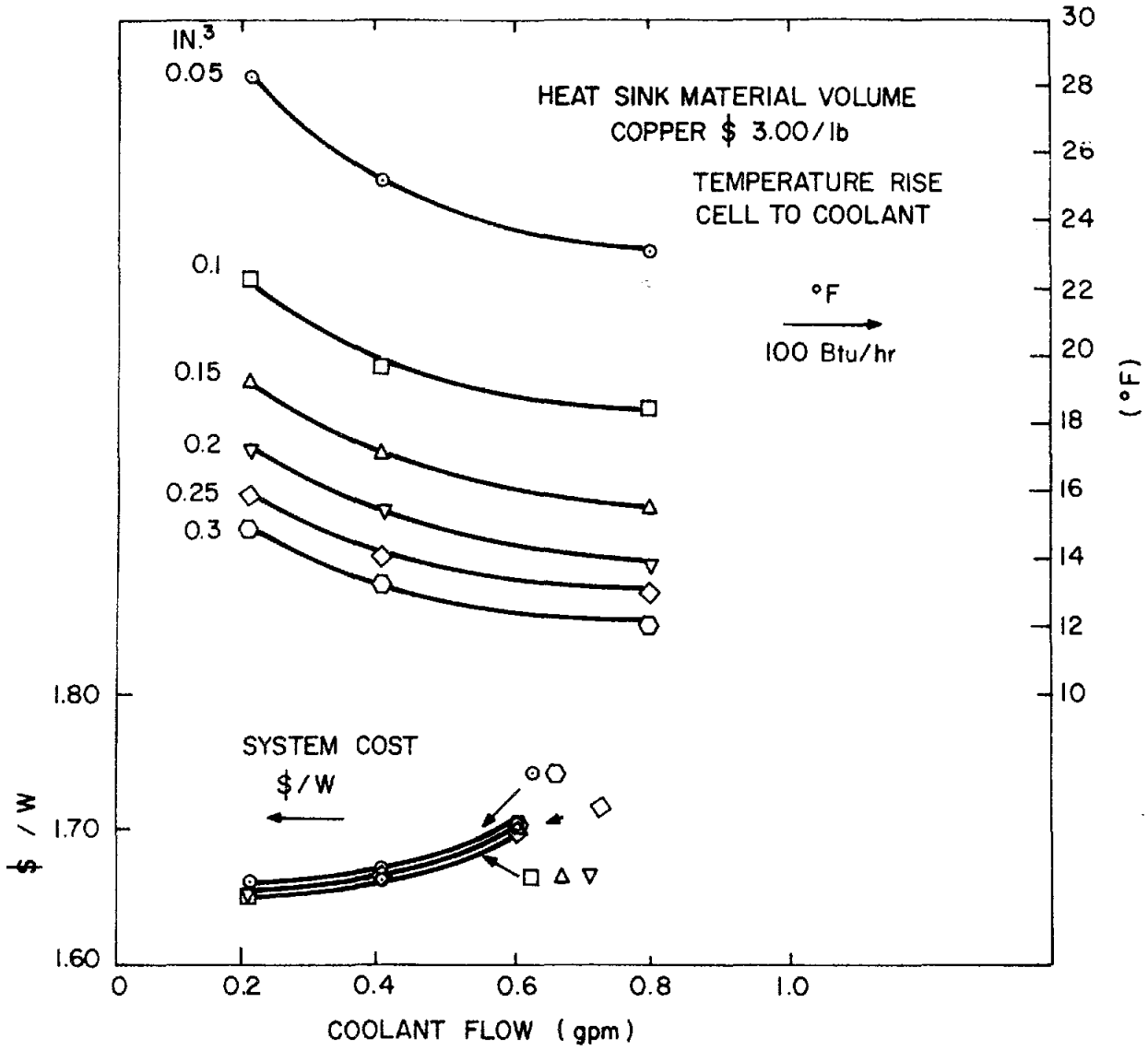

Figure 6.11 Flat Tube Cell Heat Transfer

A-5792

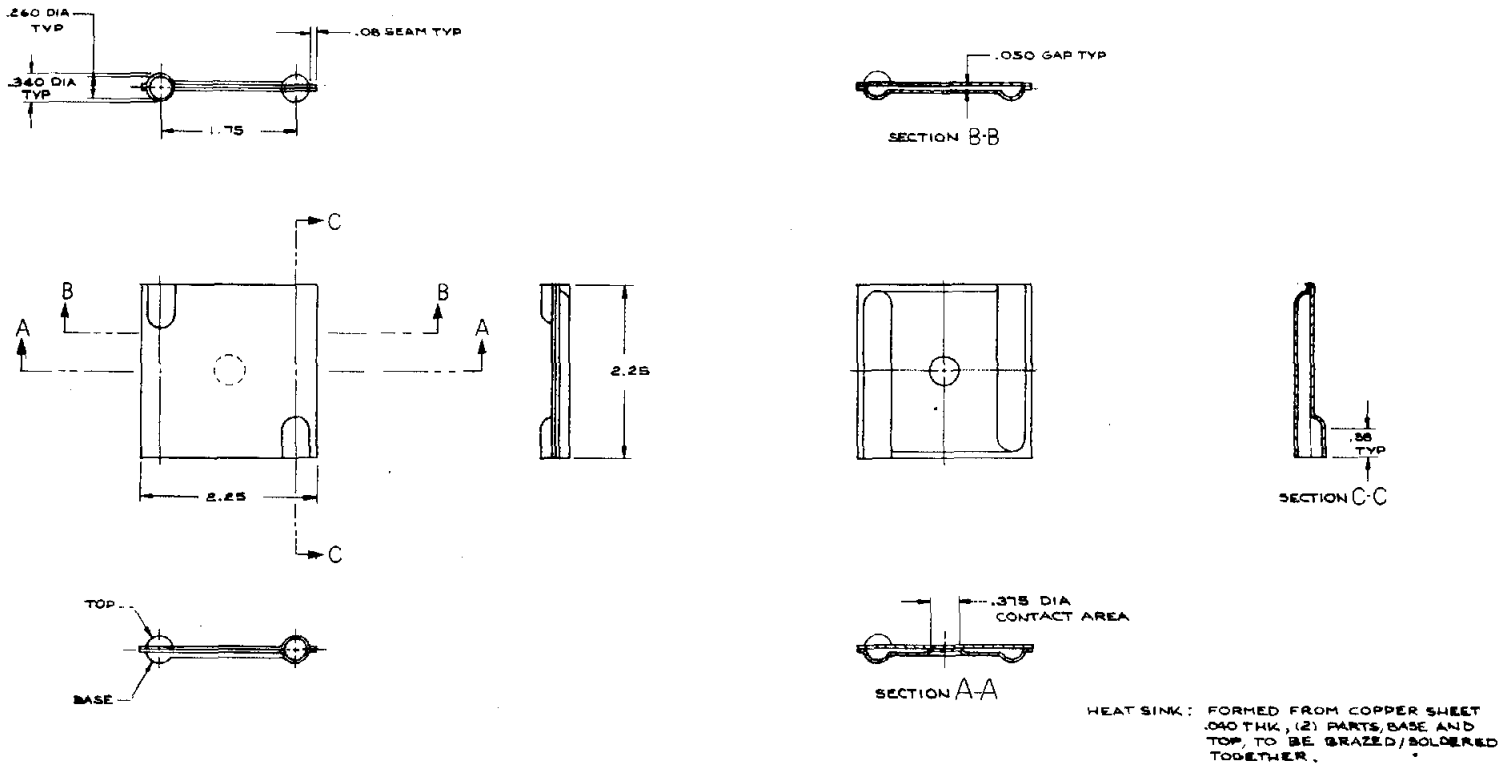

Figure 6.12 Flat Tube Heat Sink Stamped Configuration

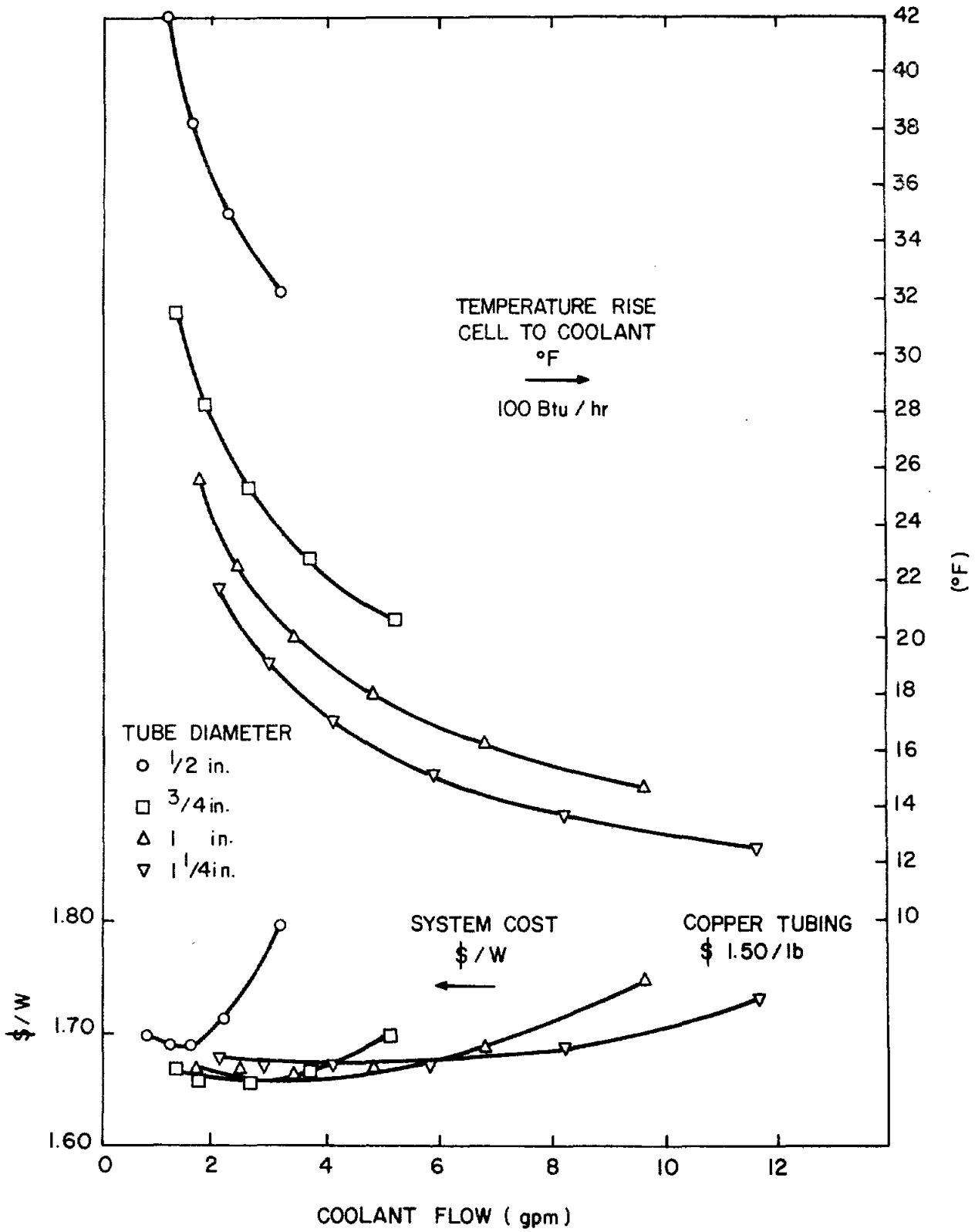

Figure 6.13 Round Tube Cell Heat Transfer

in part be met by utilizing a saddle to help distribute the heat over a larger area. An example of the approximate temperature distribution for one quarter of the tube on which the cell is mounted is shown in Figure 6.14. Each point represents the temperature of a square 0.1 in. on a side. This result was derived by a relaxation process.

6.5 PASSIVE HEAT SINK

The passive heat sink was designed using the criterion of minimizing the cost of energy produced instead of minimizing the cost of power produced, as was used for the active heat sinks. The weather data from TMY data tapes were used to determine the insolation and wind conditions, during which the array is producing power. Then, employing a cell and heat sink model, the power and energy produced was estimated. The design process, by which the heat sink was optimized, employed a reduced form of the weather data in order to simplify the design process. The weather data were reduced to provide a probability matrix based upon insolation and wind velocity for two separate locations. This probability matrix was then used to generate a normalized energy availability matrix which provides the fraction of energy available under each wind and insolation condition. Various volumes of heat sink material are adjusted for thickness and surface area to obtain the maximum delivered energy at that heat sink volume. The desired design can be selected by examining the cost of delivered energy which will be a function of heat sink volume. Figure 6.15 shows the energy matrix with percentages for each insolation and wind condition and the design results for three air temperature conditions. The design results are fairly insensitive to air temperature since only changes in cell temperature and heat sink cost are important. Figure 6.16 shows a suggested design configuration for the passive heat sink. This bent sheet design shortens the heat sink length over which the thermal boundary layer builds and provides a combination of surface orientations

```
RUN THFINDIS

ENTER THE FOLLOWING INFORMATION:
MATERIAL (1-COPPER, 2-ALUMINUM)
THICKNESS IN INCHES
WIDTH IN 0.1 INCHES
LENGTH IN 0.1 INCHES
FILM COEF. IN BTU/HR/FT2/DEG F
HEAT INPUT IN BTU/HR
CELL DIMENSION IN 0.1 INCHES
1 .045 12 30 224 25 3

ENTER THE ADDITIONAL INFORMATION:
LENGTH OF AREA OF ADDED THICKNESS
WIDTH OF AREA OF ADDED THICKNESS
THICKNESS MULTIPLIER
INITIAL TEMPERATURE

6    6 2 8

WITH  THE ABOVE PARAMETERS THE FOLLOWING  DISTRIBUTION WAS OBTAINED

TOTAL HEAT WAS  25.3
MAX TEMP CHANGE WAS   0.0
NUMBER OF ITERATIONS WAS 1001
```

22.7	22.0	20.5	18.0	16.2	14.8	12.8	11.3	10.2	9.5	9.0	8.8
22.0	21.3	19.9	17.6	15.9	14.6	12.6	11.2	10.2	9.4	9.0	8.7
20.4	19.8	18.6	16.7	15.2	14.1	12.3	11.0	10.0	9.3	8.8	8.6
17.9	17.5	16.6	15.5	14.4	13.4	11.9	10.7	9.8	9.1	8.7	8.5
16.0	15.7	15.1	14.3	13.5	12.7	11.4	10.3	9.5	8.9	8.5	8.3
14.5	14.3	13.8	13.2	12.6	12.0	10.9	9.9	9.2	8.6	8.3	8.1
12.2	12.1	11.8	11.4	11.0	10.6	9.8	9.1	8.5	8.0	7.7	7.6
10.4	10.3	10.1	9.9	9.6	9.3	8.7	8.2	7.7	7.4	7.2	7.0
9.0	8.9	8.8	8.6	8.4	8.2	7.8	7.4	7.0	6.8	6.6	6.5
7.7	7.7	7.6	7.5	7.4	7.2	6.9	6.6	6.4	6.2	6.0	6.0
6.7	6.7	6.7	6.6	6.5	6.4	6.2	5.9	5.7	5.6	5.5	5.4
5.9	5.9	5.8	5.8	5.7	5.6	5.5	5.3	5.2	5.1	5.0	4.9
5.2	5.2	5.1	5.1	5.0	5.0	4.9	4.7	4.6	4.6	4.5	4.5
4.5	4.5	4.5	4.5	4.5	4.4	4.3	4.2	4.2	4.1	4.1	4.0
4.0	4.0	4.0	4.0	4.0	3.9	3.9	3.8	3.7	3.7	3.7	3.6
3.6	3.6	3.5	3.5	3.5	3.5	3.4	3.4	3.4	3.3	3.3	3.3
3.2	3.2	3.2	3.1	3.1	3.1	3.1	3.0	3.0	3.0	3.0	3.0
2.8	2.8	2.8	2.8	2.8	2.8	2.8	2.7	2.7	2.7	2.7	2.7
2.5	2.5	2.5	2.5	2.5	2.5	2.5	2.5	2.4	2.4	2.4	2.4
2.3	2.3	2.3	2.3	2.3	2.3	2.2	2.2	2.2	2.2	2.2	2.2
2.1	2.1	2.1	2.1	2.1	2.0	2.0	2.0	2.0	2.0	2.0	2.0
1.9	1.9	1.9	1.9	1.9	1.9	1.9	1.8	1.8	1.8	1.8	1.8
1.7	1.7	1.7	1.7	1.7	1.7	1.7	1.7	1.7	1.7	1.7	1.7
1.6	1.6	1.6	1.6	1.6	1.6	1.6	1.6	1.6	1.6	1.6	1.6
1.5	1.5	1.5	1.5	1.5	1.5	1.5	1.5	1.5	1.5	1.5	1.5
1.4	1.4	1.4	1.4	1.4	1.4	1.4	1.4	1.4	1.4	1.4	1.4
1.3	1.3	1.3	1.3	1.3	1.3	1.3	1.3	1.3	1.3	1.3	1.3
1.3	1.3	1.3	1.3	1.3	1.3	1.3	1.3	1.3	1.3	1.3	1.3
1.2	1.2	1.2	1.2	1.2	1.2	1.2	1.2	1.2	1.2	1.2	1.2
1.2	1.2	1.2	1.2	1.2	1.2	1.2	1.2	1.2	1.2	1.2	1.2

```
FORTRAN STOP
$
```

Figure 6.14 Temperature Distribution for One Quarter of a Tube Heat Sink

A-6068a

ENERGY DISTRIBUTION, KWH'S (NORMALIZED)

DIRECT INSOL.	<0.1	0.1-1	1-2	2-3	3-4	4-5	5-6	6-7	7-8	>8
0.001 - 0.1	0.2	0.0	0.1	0.3	0.2	0.2	0.2	0.1	0.0	0.0
0.1 - 0.2	0.3	0.0	0.2	0.4	0.4	0.4	0.3	0.2	0.1	0.1
0.2 - 0.3	0.5	0.0	0.3	0.3	0.4	0.3	0.3	0.2	0.1	0.1
0.3 - 0.4	0.5	0.0	0.2	0.4	0.5	0.4	0.4	0.4	0.2	0.3
0.4 - 0.5	0.5	0.0	0.4	0.6	0.9	0.8	0.9	0.4	0.3	0.4
0.5 - 0.6	0.9	0.0	0.5	0.8	1.0	1.2	1.0	0.9	0.3	0.5
0.6 - 0.7	1.2	0.0	0.9	1.5	1.6	1.9	1.9	1.8	0.6	1.2
0.7 - 0.8	1.3	0.0	1.4	2.4	2.8	4.4	4.0	2.8	1.8	2.0
0.8 - 0.9	0.9	0.0	1.3	3.2	5.1	5.8	6.5	5.2	2.9	3.5
0.9 - 1.0	0.1	0.0	0.3	0.9	1.2	1.3	1.6	1.4	0.8	0.7

WIND SPEED, M/S

```
FORTRAN STOP
$
```

Figure 6.15 Energy Distribution and Passive Design Results

```
$ RUN PASSIVE

PASSIVE HEAT SINK PROGRAM

 0.2     0.3     0.5     0.5     0.5     0.9     1.2     1.3     0.9     0.1
 0.0     0.0     0.0     0.0     0.0     0.0     0.0     0.0     0.0     0.0
 0.1     0.2     0.3     0.2     0.4     0.5     0.9     1.4     1.3     0.3
 0.3     0.4     0.3     0.4     0.6     0.8     1.5     2.4     3.2     0.9
 0.2     0.4     0.4     0.5     0.9     1.0     1.6     2.8     5.1     1.2
 0.2     0.4     0.3     0.4     0.8     1.2     1.9     4.4     5.8     1.3
 0.2     0.3     0.3     0.4     0.9     1.0     1.9     4.0     6.5     1.6
 0.1     0.2     0.2     0.4     0.4     0.9     1.8     2.8     5.2     1.4
 0.0     0.1     0.1     0.2     0.3     0.3     0.6     1.8     2.9     0.8
 0.0     0.1     0.1     0.3     0.4     0.5     1.2     2.0     3.5     0.7


AIR TEMPERATURE = 30.00 DEGREES F
H.S. VOLUME          1.000    2.000    3.000    4.000    5.000    6.000    7.000    8.000    9.000   10.000
H.S. THICK           0.030    0.040    0.050    0.055    0.060    0.065    0.070    0.075    0.075    0.080
H.S. WIDTH           5.774    7.071    7.746    8.528    9.129    9.608   10.000   10.328   10.954   11.180
MEAN FIN EFF.        0.458    0.455    0.474    0.464    0.461    0.462    0.465    0.469    0.451    0.458
MEAN TEMP. DIFF.    60.589   45.154   38.032   33.652   30.616   28.340   26.550   25.094   23.879   22.829
FRAC. ENERGY DEL.    0.899    0.925    0.936    0.944    0.949    0.953    0.956    0.958    0.960    0.962
PERF. FACTOR        11.841   11.666   11.670   11.731   11.819   11.922   12.035   12.153   12.277   12.403


AIR TEMPERATURE = 60.00 DEGREES F
H.S. VOLUME          1.000    2.000    3.000    4.000    5.000    6.000    7.000    8.000    9.000   10.000
H.S. THICK           0.030    0.040    0.050    0.055    0.060    0.065    0.070    0.075    0.080    0.080
H.S. WIDTH           5.774    7.071    7.746    8.528    9.129    9.608   10.000   10.328   10.607   11.180
MEAN FIN EFF.        0.457    0.454    0.473    0.463    0.460    0.461    0.464    0.468    0.474    0.457
MEAN TEMP. DIFF.    60.508   45.096   37.981   33.610   30.578   28.305   26.517   25.063   23.851   22.802
FRAC. ENERGY DEL.    0.899    0.925    0.937    0.944    0.949    0.953    0.956    0.958    0.960    0.962
PERF. FACTOR        11.839   11.664   11.669   11.730   11.819   11.922   12.034   12.153   12.276   12.402


AIR TEMPERATURE = 90.00 DEGREES F
H.S. VOLUME          1.000    2.000    3.000    4.000    5.000    6.000    7.000    8.000    9.000   10.000
H.S. THICK           0.030    0.040    0.050    0.055    0.060    0.065    0.070    0.075    0.080    0.080
H.S. WIDTH           5.774    7.071    7.746    8.528    9.129    9.608   10.000   10.328   10.607   11.180
MEAN FIN EFF.        0.456    0.453    0.472    0.462    0.459    0.460    0.463    0.468    0.473    0.456
MEAN TEMP. DIFF.    60.441   45.050   37.940   33.575   30.548   28.277   26.490   25.037   23.827   22.780
FRAC. ENERGY DEL.    0.899    0.925    0.937    0.944    0.949    0.953    0.956    0.958    0.960    0.962
PERF. FACTOR        11.838   11.663   11.668   11.730   11.818   11.921   12.033   12.152   12.275   12.402

FORTRAN STOP
$
```

Figure 6.15 Energy Distribution and Passive Design Results (continued)

A-6064

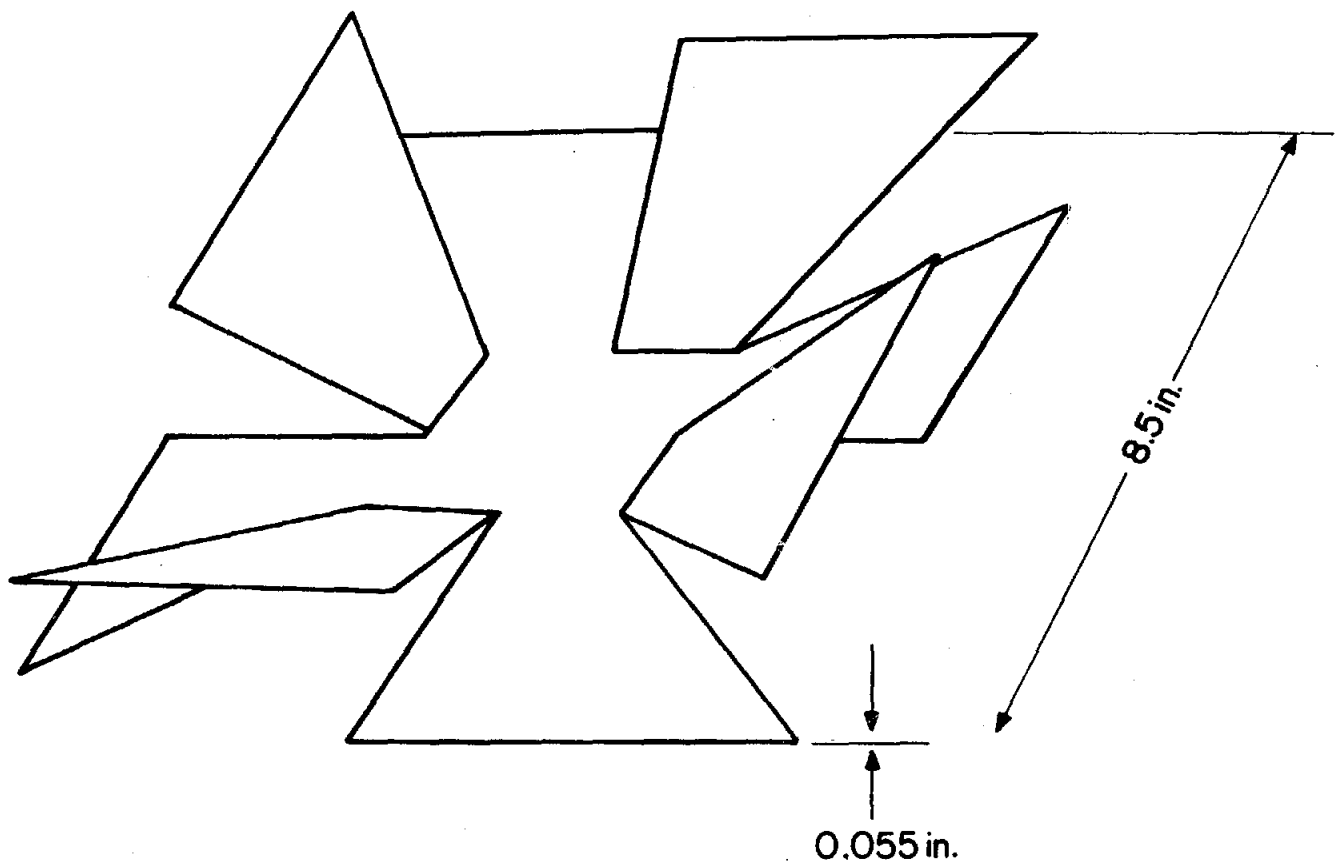

Figure 6.16 Rear View of Passive Heat Sink

to ensure good natural convection regardless of module position. The cell would be soldered directly to a 2 in. x 2 in. heat spreader of 0.072 in. copper. The heat spreader can then be either adhesively bonded to the passive heat sink, or mechanically attached utilizing a silicone grease loaded with metallic oxides to improve the conductance.

6.6 GENERAL

The design results are summarized in Figure 6.17. This graph shows the best results are for the finned heat sink although fabrication difficulties may make this choice less attractive. The flattened tube and the round tube have comparable performance factors and the temperature rise of the round tubes can be considerably improved by the addition of a heat spreader on the smaller diameter tubes. The addition of copper, at a lower cost due to lower fabrication cost, will also significantly improve the performance of the flattened tube heat sink. The flattened tube and round tube heat sinks appear to be the best choices, although use of the rigid round tube configuration will be limited to larger cells and lower concentration ratios because of thermal expansion.

6.7 HEAT SINK MANUFACTURING OPTIONS

A number of candidate manufacturing methods for producing heat sinks have been evaluated, both for their contribution to the overall system cost and their influence on the heat sink/cell mount design. Other issues addressed in this evaluation included:

- Thermal expansion mismatch between the cooling loop and the module case, from both a structure and a tracking accuracy viewpoint
- Number of parts required per module, and assembly methods
- Temperature rise/flow rate operating range
- Potential for series/parallel connection

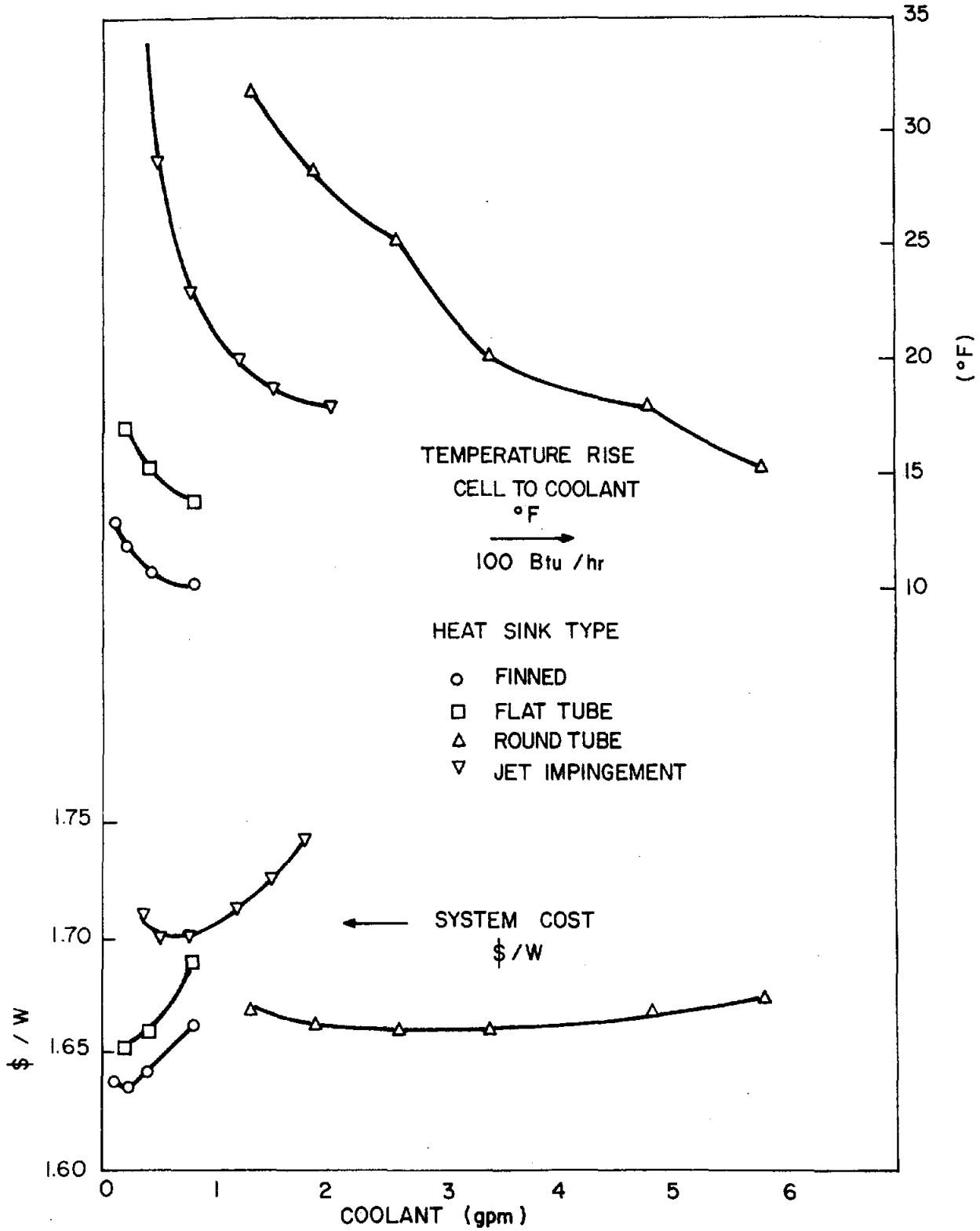

Figure 6.17 Heat Transfer for Various Design Configurations

The base line finned heat sink design (Figure 6.18) specified the use of a molded heat sink housing and polymeric tubing for fluid interconnection. This concept required assembly and several parts. It did provide a good substrate for handling the cell assembly, and alleviated thermal expansion mismatch problems. Cell temperature/flow rate characteristics were good, and the design was amenable to series/parallel connection.

Soldering or brazing of folded fins, machining, copper extrusion, and impact extrusion were considered as potential methods for producing the finned heat sink. Copper bar stock could be machined to the desired configuration using ganged saws. This process is both time and materials intensive. Resale of the copper filings to the bar supplier improves the economics, but the cost remains unfavorable.

Copper extrusion appeared to be an appropriate technique for manufacturing the heat sink, however, of several extrusion houses contacted, none felt capable of forming the profile. Fins with a large height/width ratio apparently exceed the capabilities of this technology at the present time.

Impact extrusion is a process currently used to produce certain types of heat sinks. Its rapid cycle time and good materials utilization imply economic production. The company we contacted felt that they could form the finned heat sink, however, a certain amount of development work would be required.

The soldering and brazing of fins formed by bending thin sheet is a production-worthy process, but cost estimates by companies in this business exceeded the level that would make this design cost effective. Since the material cost is not a dominant cost in the quotation we received, there is potential for cost reduction in this method.

Since the production of heat sinks with multiple fins involves relatively expensive manufacturing methods, a flattened tube laminar flow

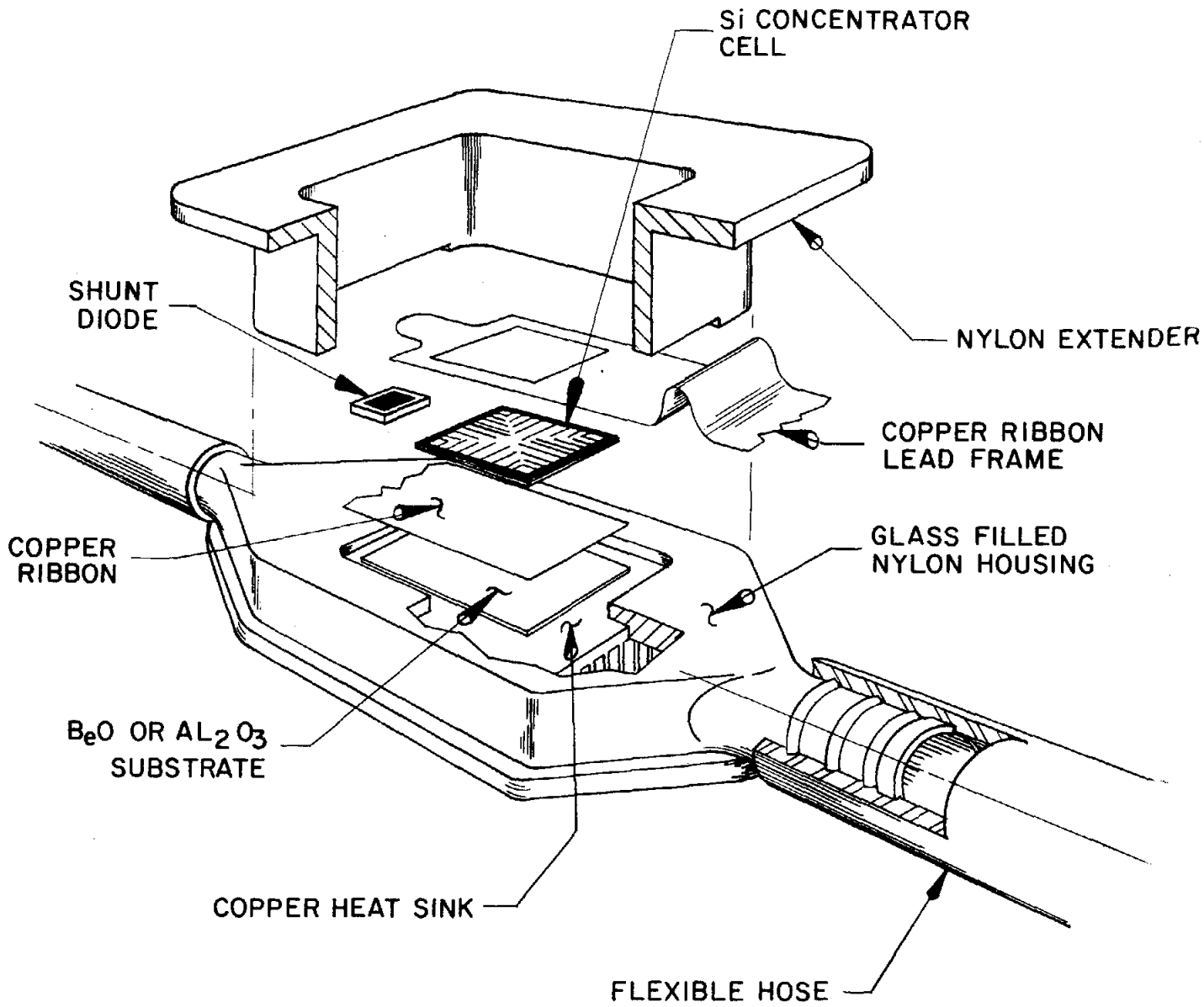

Figure 6.18 Photovoltaic Cell Assembly and Base Line Cooling Subsystem

heat sink design was developed. Variations of this concept are indicated in Figures 6.19, 6.20, and 6.21. Each of these designs utilizes a single central stud directly below the photovoltaic cell to conduct heat to the back side of the flattened tube. In this manner both sides of the tube act as fins to conduct heat into the coolant fluid. Computer modeling of the heat transfer characteristics, temperature, and pressure drops expected with this type of heat sink indicated acceptable performance.

Several methods of manufacturing were considered for the flattened tube design. Pressure welding, typified by the Roll-Bond process of Olin Brass, was considered as a potential method for forming heat sinks with integral fluid interconnections. Figure 6.19 indicates the concept.

Conversations with Olin Brass uncovered problems with this approach. The length and width limits of their process would not permit a useful number of heat sinks to be fabricated as a unit. Separating the strips of heat sinks and tubing would be extremely difficult. In addition, parallel fluid circuits would introduce problems in manifolding. For these reasons, the pressure welding design was not pursued further.

The flattened tube design for the heat sink is amenable to several other manufacturing methods. One alternative utilizes tube drawing technology followed by stamping and furnace brazing, as indicated in Figure 6.20. The tubing mill we contacted is capable of performing the required operations, and of assembling the heat sinks and interconnecting copper tubing into module cooling subassemblies. (See Figure 6.22.) A curved connecting tube is utilized between the heat sinks to reduce the effects of differential thermal expansion between the all copper fluid loop and the acrylic module case. Calculations and experimental measurements indicate that the worst case thermal expansion mismatch forces at a cell assembly will be on the order of 1.0 pound for this configuration. The development of a more detailed design is required to accurately determine the cost of this approach; however, the ballpark figure of $2.50 to $3.00

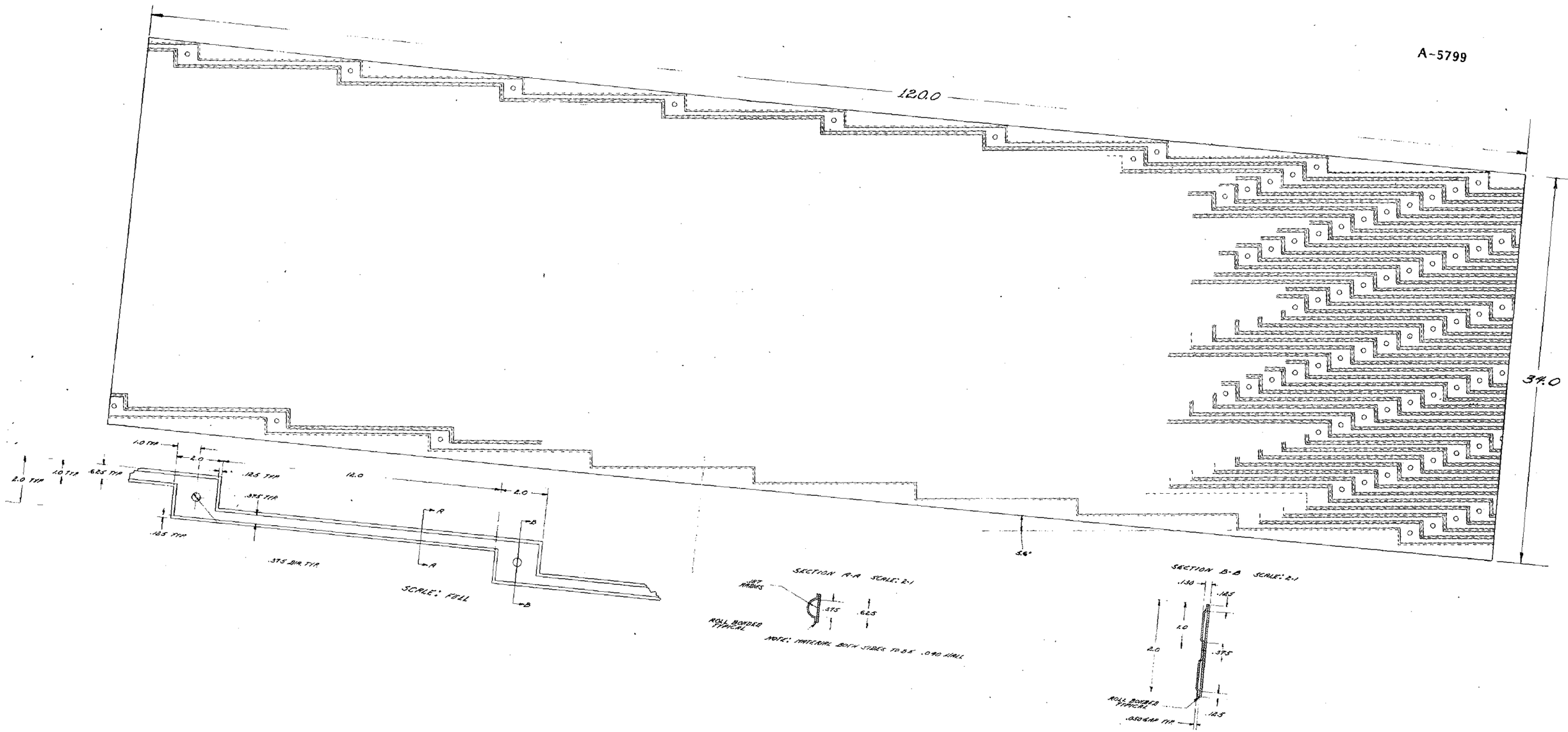

Figure 6.19 Pressure Welded Heat Sinks

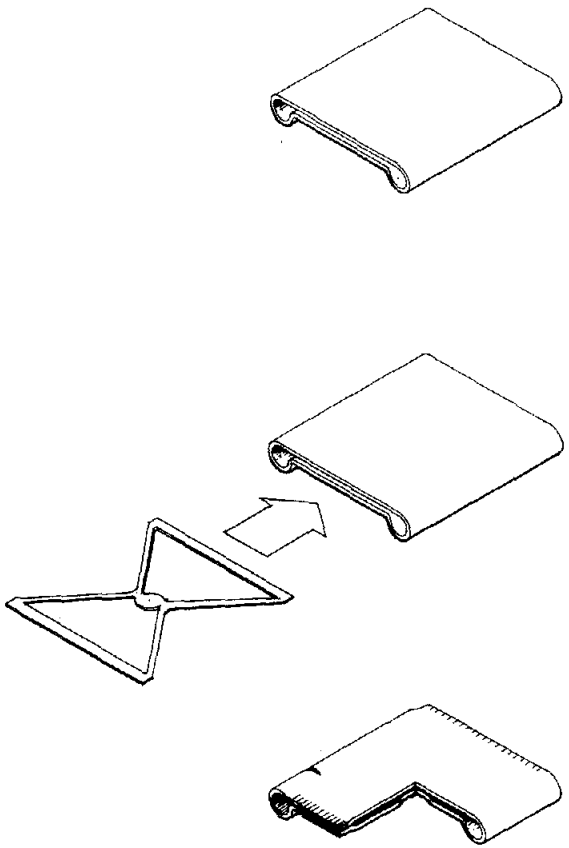

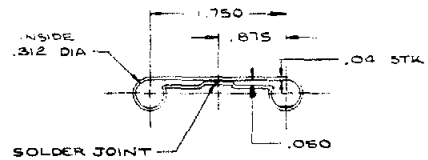

SECTION A-A

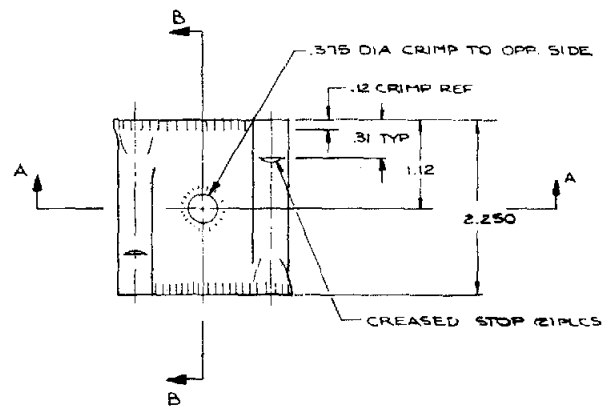

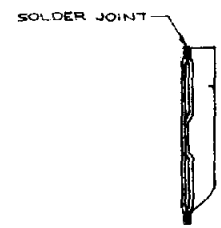

SECTION B-B

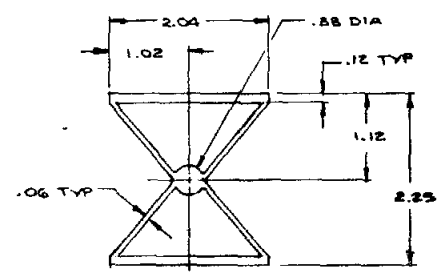

SOLDER PREFORM

Figure 6.20 Drawn Tube Heat Sink Design

A-5792

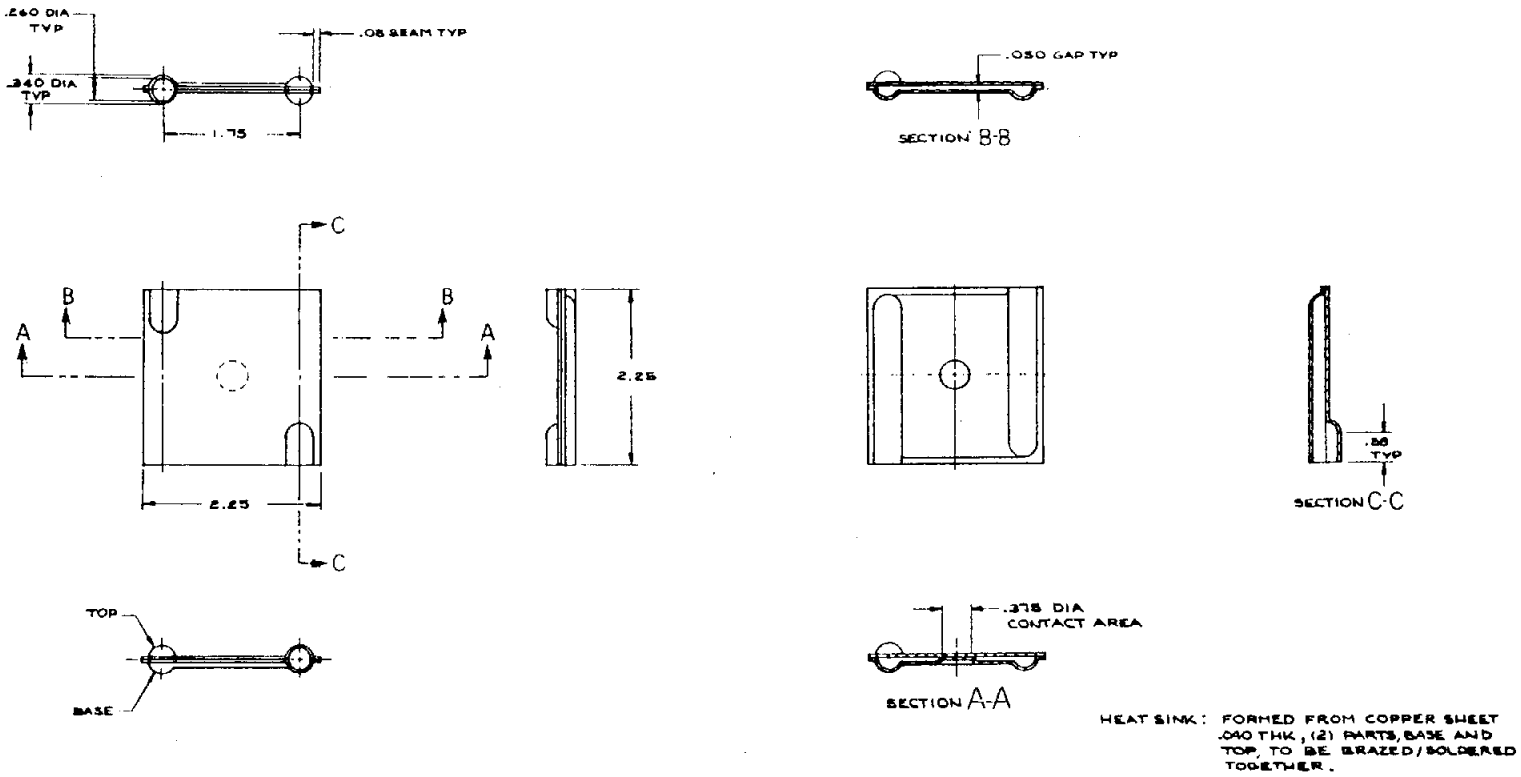

Figure 6.21 Stamped Heat Sink Design

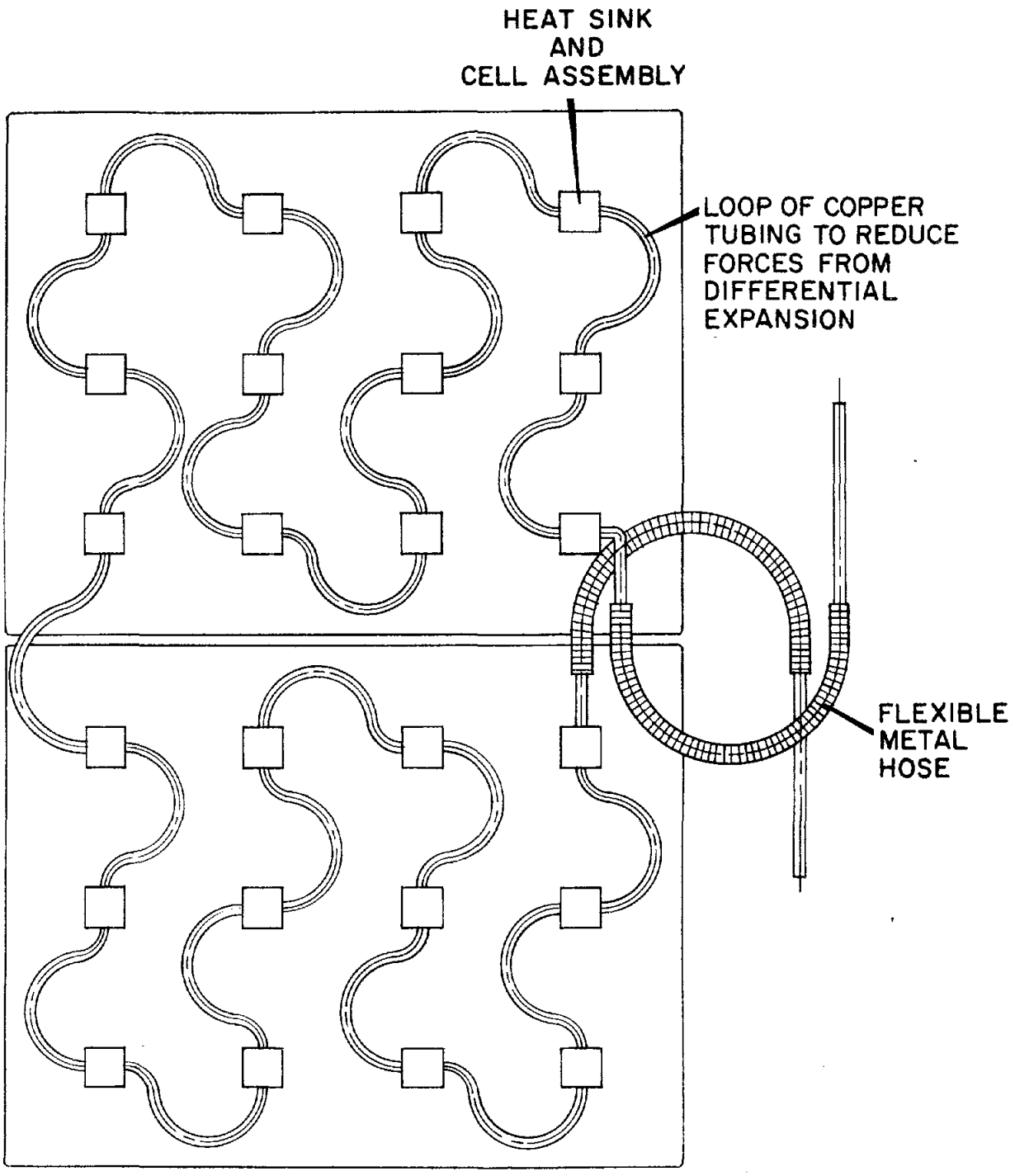

Figure 6.22 Configuration for All-Copper Cooling Subassembly for Photovoltaic Module Pair

per pound for drawn copper products provided by the tubing mill is within the feasible range.

A heat sink design closely related to the drawn tube alternative is shown in Figure 6.21. This two-part heat sink could be formed by hydroforming, stamping, or drawing. Each of these processes would be appropriate at a given production level; hydroforming for low volume production, stamping and drawing for large scale production. These heat sinks would be put together into module cooling subassemblies in the same manner as the drawn tube version. The flattened tube design requires somewhat higher fluid flow rates to achieve a cell/fluid temperature drop comparable to the finned design. This does not signficantly alter the total system cost.

Parallel fluid connections would require the use of a manifold. Although this would increase the amount of copper needed for the cooling loop, it could easily be accommodated since the connecting tubing has a circular cross section compatible with standardly produced copper headers. This arrangement could also be incorporated into the furnace brazing assembly step.

The use of copper tubing itself as a part of the heat sink was explored. The concept can be envisioned as saddle-shaped copper cell mounts placed at intervals on ½-in. diameter copper tubing. Although this design can achieve acceptable cell operating temperatures, it requires the use of larger diameter tubing, significantly more copper, and higher flow rates than the flattened tube designs. One reason for this is that although the copper in the tubing adjacent to a saddle is utilized as a fin, copper in the tubing between the saddles is not effectively utilized. This design precludes the use of curved connecting tubing between heat sinks to alleviate thermal expansion mismatch problems, because the larger diameter tubing is too rigid. The copper tubing is mass produced, and the saddle-shaped cell mounts can be produced by copper extrusion.

The final active heat sink manufacturing method evaluated is indicated in Figure 6.23. Inexpensive ¼-in. diameter copper tubing is formed into a compressed "S" shape, and a flat copper heat spreader is soldered or brazed to the tubing. This allows the loops of tubing to act as fins, while the heat spreader provides improved conductance near the cell. The configuration is similar to the round tubing with the saddle cell mount.

The flow rates required to achieve acceptable cell operating temperatures are similar to those required for the flattened tube heat sink. Differential thermal expansion and series/parallel flow connections are also handled in the same manner as for the flattened tube design.

This concept avoids high tooling costs and uses components that are already mass produced. The cost to form the copper tubing into the desired shape has not yet been determined, but it is anticipated that the manufacturing potential is favorable.

A-6083

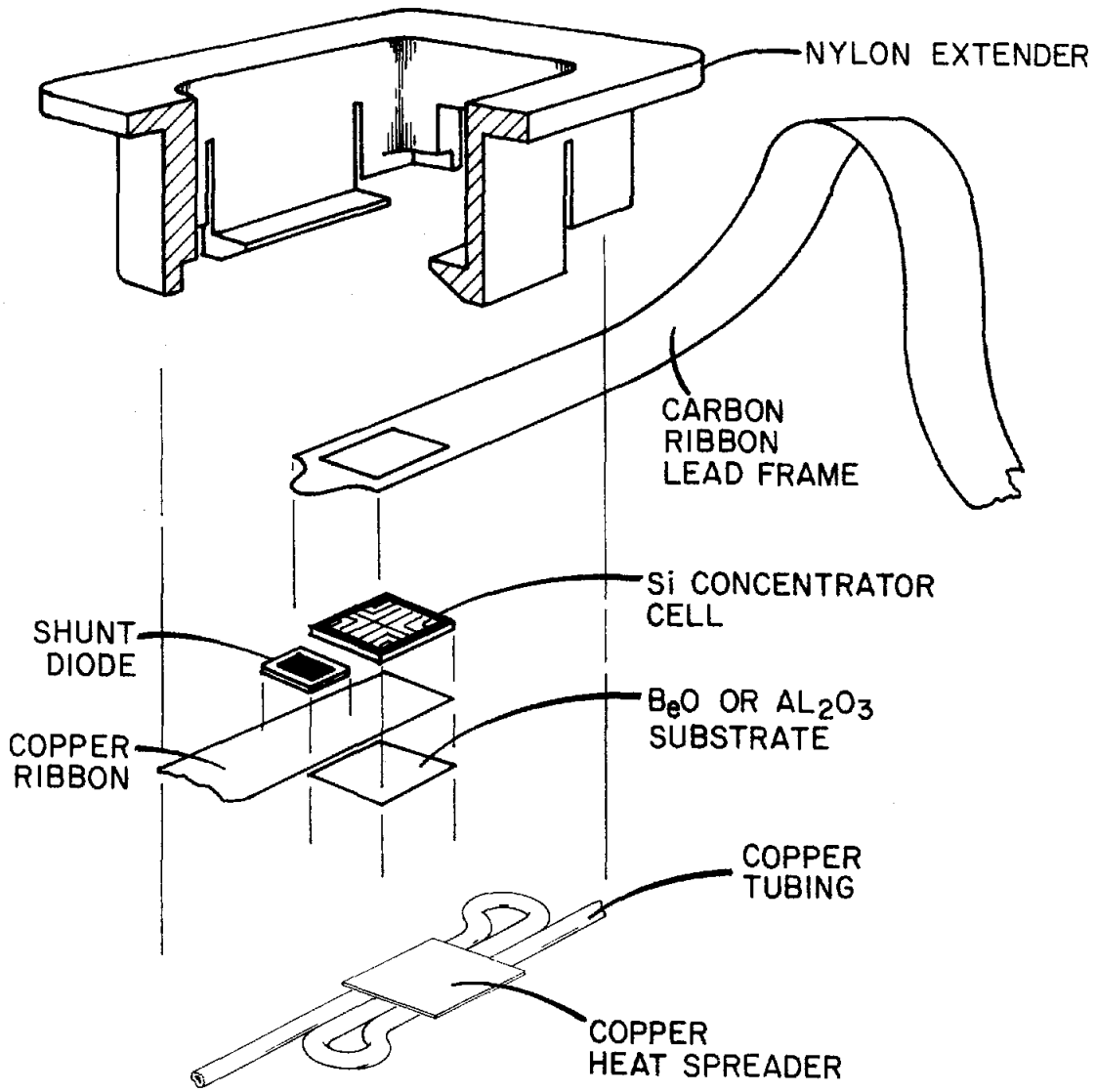

Figure 6.23 Serpentine Tube With Heat Spreader Design

7. MODULE DESIGN

7.1 DESIGN CRITERIA

The module case was designed with the criteria that the lens/case assembly would maintain the proper optical alignment, within the allowed tolerances, over the full range of possible environmental conditions. Furthermore, the assembly was designed to withstand the maximum wind stress in an unstowed worst case angle of attack position. After the first design iteration these critiera were deemed too severe since only a small fraction of available energy occurs under extreme environmental conditions. Furthermore, the original wind loading of 40 psi, used in the design, is beyond the requirement for most locations. The peak wind load experienced by an array can also be reduced by building "boundary layer trips" around the array, which effectively create a "wind shadow" in the same way that adjacent collector rows "shadow" each other. The ability of a thermoplastic module to withstand short-term high stresses is more than one order of magnitude higher than its ability to withstand sustained stress levels. Therefore, the array can be stowed under extreme conditions, reducing the design requirements for a sustained load.

Additional design criteria placed upon the module included the ability to operate the module in an off-axis condition without module damage. Such a condition could occur if the tracking sensors become misaligned with respect to the optical axis of the module. Another criterion allowed for a continuous cell assembly temperature of 100°C without module damage. Because we intended to use a low-temperature thermoplastic for the module, direct attachment of the cell assembly to the module was not acceptable. Two overriding criteria for the module were that the design be low in cost and amenable to current, large volume production techniques.

7.2 MODULE CASE

The module case was designed as a monocoque, where the lenses, module bottom, and sides are all stressed components. This type of design

places the minimum stress on the material, and therefore allows for a lighter and less costly module. The design does require that the lenses be rigidly attached to the module case so that the lenses and module bottom are in effect made the top and bottom of a beam. Under these conditions, either the lens assembly or the module bottom is in compression and therefore must not exhibit a buckling instability. Furthermore, the module sides are subject to web buckling and the edges of the module are subject to failure from excessive shear stress.

Lens assembly buckling is inhibited by the shape of the domed lenses which create stiffening ribs between lenses. The bottom of the module can be prevented from buckling by adding stiffening ribs. Such free-standing ribs are also subject to buckling and must be designed to avoid catastrophic failure. The module sides can also be stiffened by vertical ribs to avoid web buckling.

The original design assumed acrylic for the module material and utilized 300 psi as the long-term design working stress and 300,000 psi as the modulus of elasticity. The 300-psi figure was used to avoid long-term creep problems. The actual fatigue limit for acrylic is above 4000 psi at 25°C and the momentary modulus is approximately 450,000 psi at that temperature. The original design was for a square module with 16 lenses, but the molding limitation of most injection molding machines induced us to reduce the module to a 3 lens x 4 lens configuration. An artist's conception of this design is shown in Figure 7.1 and a detailed drawing is shown in Figure 7.2.

The design was revised later in the program and the new design reflects both reduced stress requirements and the desire to reduce the size of the molded part. The new design is for one-quarter of the module, which can be adhesively bonded to three identical pieces to form the square 16 lens module. The reduction of the size of the molded part reflects both the desire to reduce initial tooling cost and the desire to allow

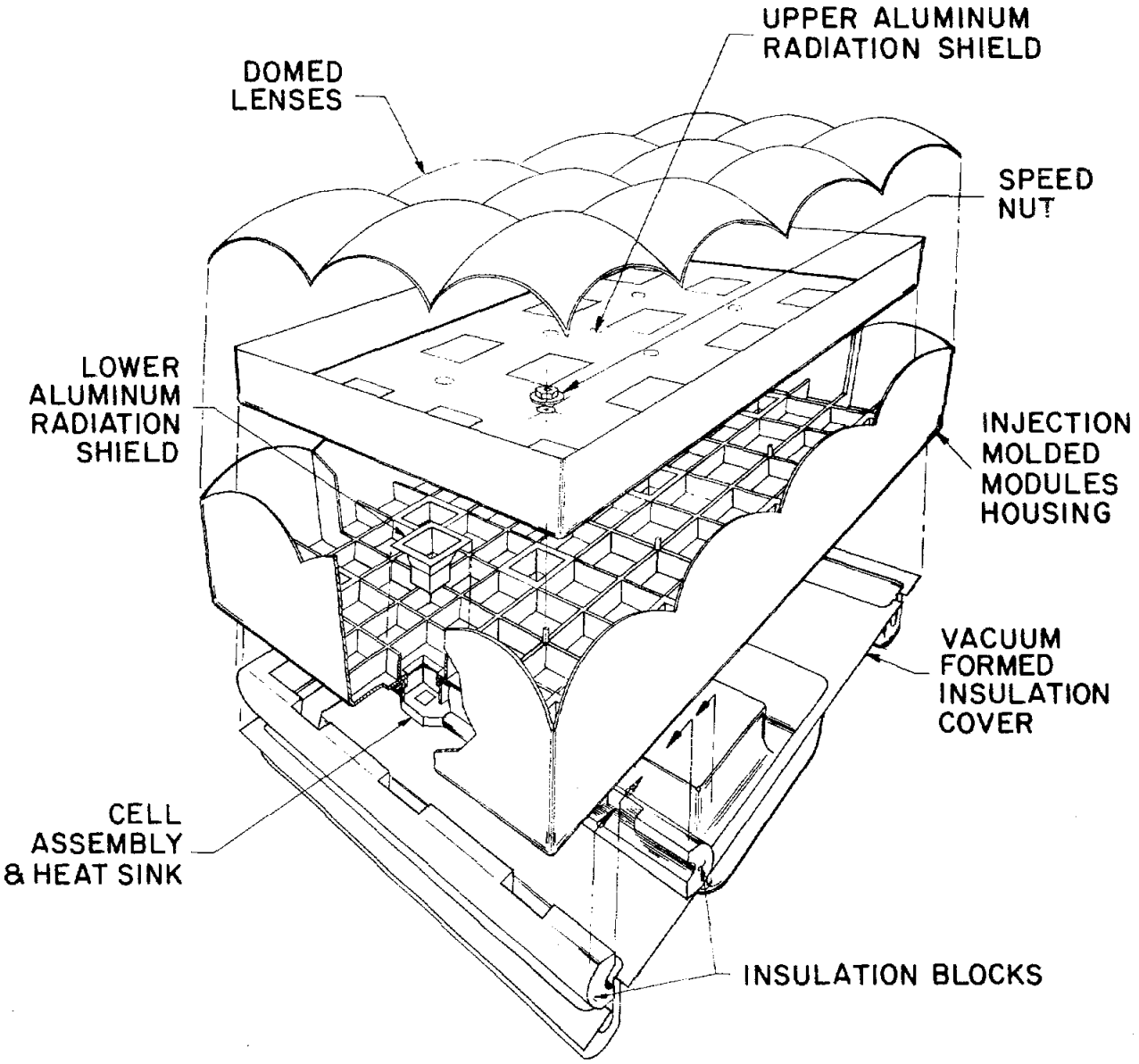

Figure 7.1 Original Photovoltaic Module

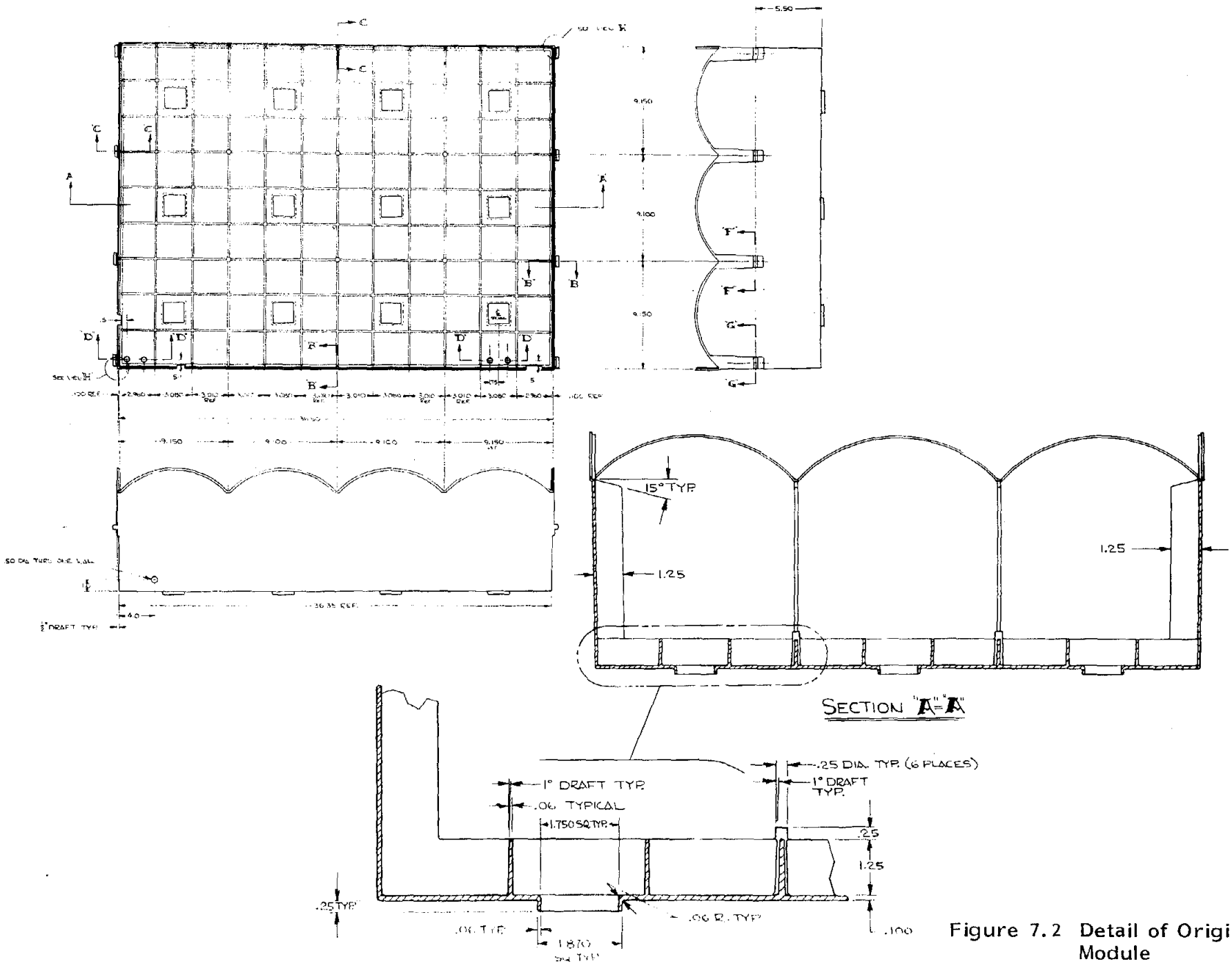

Figure 7.2 Detail of Original Module

the part to be molded on a smaller size machine. This design is shown in Figure 7.3 and includes edge details to permit adhesive bonding of the module quadrants and of the lens assembly to the completed module.

7.3 RADIATION SHIELD

Protection for the acrylic module case in the event of off-axis operation is provided by the radiation shield. The shield is arranged such that sunlight concentrated by the lenses cannot strike any portion of the case. Figure 7.1 indicates an early design iteration. Relatively thick (0.012-in. aluminum) lower radiation shields are utilized in the immediate vicinity of the lens targets, where the intensity of an off-axis beam would approach that seen by the PV cell under normal operation. The upper radiation shield protects the remaining area. This part is formed of 0.003-in. aluminum foil, as it is located well above the target plane of the lens and cannot see the high sunlight concentrations observed near the target.

Computer modeling of heat transfer and temperature profiles in thin plates subjected to very localized heating suggested that thin aluminum foil (0.0015 in.) would provide appropriate protection for the module case, although the foil itself might attain local high temperatures near the concentrated beam. Several experiments were performed to test this information, and to establish the temperature profile generated by an off-axis beam from the domed lens in the area around the lens target.

Sample radiation shields, 4-in. square, were positioned near the lens target of an operating single lens module. A thin film thermocouple was bonded to the back of each sample with a thermally conductive epoxy. The back of each thermocouple was insulated with a ¼-in. square piece of adhesive foam. The single lens module was oriented such that the off-axis concentrated beam produced the maximum temperature on the sample shield directly above the thermocouple. This was repeated, moving the sample shield by ½-in. increments both horizontally and vertically. The

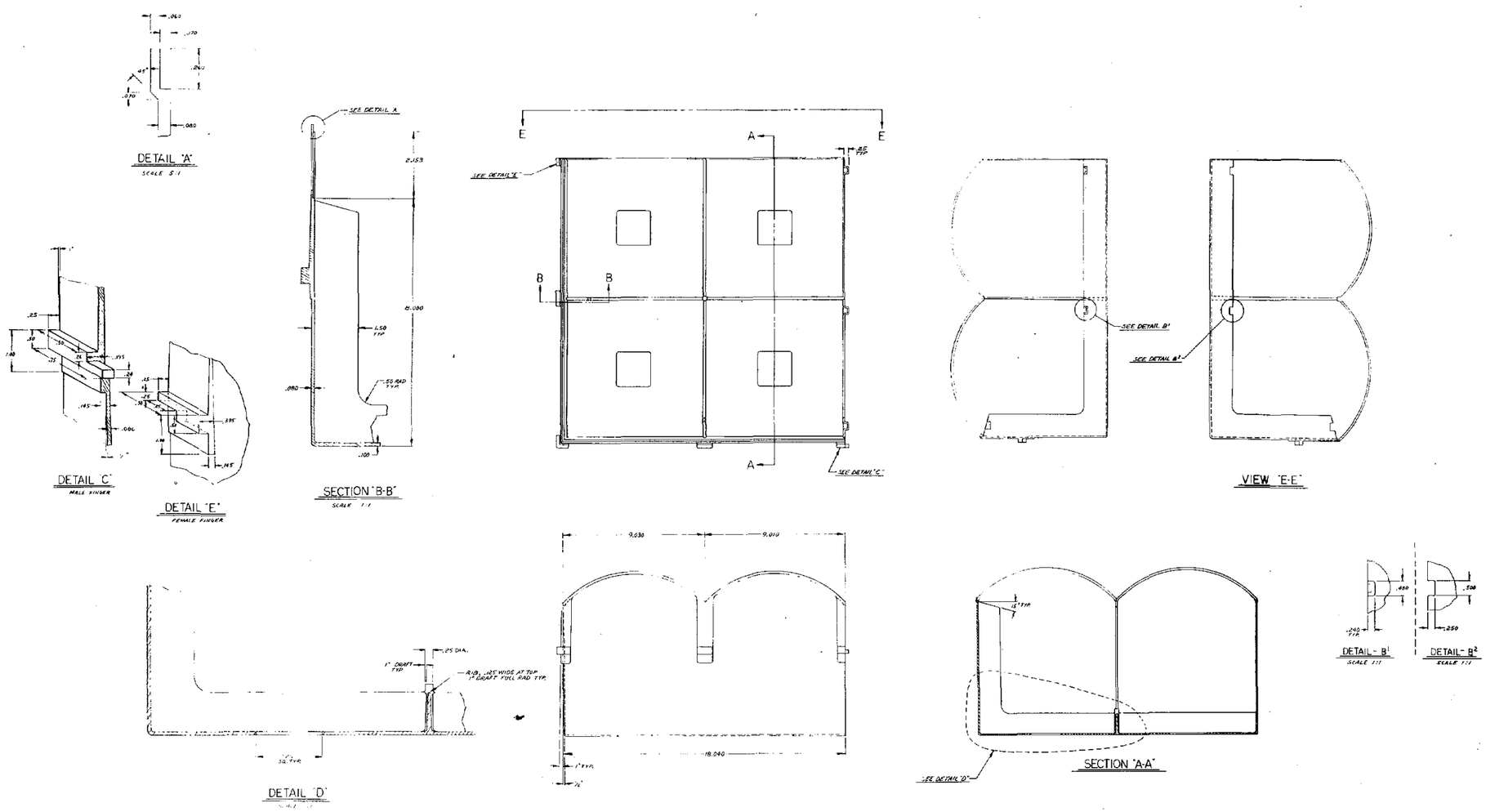

Figure 7.3 New Design for a Module Quadrant

temperatures achieved using 0.0015-in. aluminum foil, and 0.012-in. aluminum sheet are indicated in Figure 7.4. These are in good agreement with our computer model.

Based on these temperature profiles, a single piece radiation shield formed of 1.5-mil aluminum foil will provide protection for the module case in the unlikely event of prolonged off-axis operation. The exact configuration of the shield will be determined after the manufacturing process has been selected. Foil forming, such as used to fabricate TV dinner trays and other food packages, is being investigated. The final radiation shield design will incorporate integral stiffening ribs, and will be attached to the module case only at those points that would remain below the heat distortion temperature of acrylic, even when exposed to the off-axis beam from a lens.

7.4 CELL ASSEMBLY ATTACHMENT

The attachment of the cell assembly to the module case was designed to meet several requirements. First, it had to provide a thermal break between the cell assembly, which may attain temperatures up to 100°C, and the acrylic module case. Second, it had to provide for precise alignment of the cell assembly beneath the associated lens.

The extenders indicated in Figures 6.18 and 6.23 fulfill these criteria. Intended to be injection molded of glass filled nylon, this part can withstand the operating temperatures of the cell/heat sink assembly. Since nylon is a poor conductor of heat, the thermal break requirement is also satisfied. This design also allows the lens-to-cell distance of the module to be varied by changing the length of the extender. This permits different PV cell sizes and/or concentration ratios to be accommodated without requiring changes in the remainder of the module. Ultrasonic welding, adhesive bonding, mechanical fastening, and snap fit attachment have been considered as means to affix the extender to the module case.

0.0015-IN. ALUMINUM FOIL

Vertical Distance Above Target Plane (in.)										
2.5	180	179	170	167	172	195	227	232	232	240
2.0	193	197	201	206	210	237	249	264	265	264
1.5	219	220	224	237	251	273	279	282	271	269
1.0	251	262	269	287	315	327	327	312	306	272
0.5	329	339	360	370	374	379	361	342	311	275
0	441	437	435	417	401	357	340	296	269	259
	0	0.5	1.0	1.5	2.0	2.5	3.0	3.5	4.0	4.5

Horizontal Distance from Target (in.)

0.012-IN. ALUMINUM SHEET

Vertical Distance Above Target Plane (in.)										
2.5	183	181	181	183	188	189	198	207	208	209
2.0	190	189	190	193	196	204	214	219	218	219
1.5	197	198	199	205	214	221	229	234	234	227
1.0	217	218	222	227	238	245	247	245	241	230
0.5	239	242	247	255	260	265	262	252	243	232
0	290	285	281	277	270	256	250	240	217	189
	0	0.5	1.0	1.5	2.0	2.5	3.0	3.5	4.0	4.5

Horizontal Distance from Target (in.)

Figure 7.4 Experimental Results for Radiation Shields

7.5 LENS ASSEMBLY TECHNIQUES

The domed Fresnel lenses were initially intended to be bonded to each other and to the module case by means of ultrasonic welding. Investigation of this bonding technique uncovered a major technical difficulty for this application. While ultrasonic welding can produce high strength and weather-tight welds, it is difficult to produce high quality welds on a long curved surface. At the current state of the technology, the size of ultrasonic horns that can be manufactured is limited to about 4 in. Welds larger than this are produced by scanning a smaller horn across the desired bond area.

Sample domed lenses were sent to several ultrasonic welding houses to be scan welded. One company was able to bond the lenses, but with very poor results. Branson Sonic Power Company evaluated the lenses as being poor candidates for ultrasonic welding.

Adhesive bonding was considered for the lens assembly method, with more favorable results. Rohm & Haas Company provided information on adhesives that they had found suitable for use with acrylic. Solvent-based cements, such as Cement II, do not have setup times consistent with high volume production, and can exhibit stress crazing under outdoor conditions. Two-part curing adhesives, such as PS-30 and epoxies, were considered but these presented either pot life or setup time problems. A family of two-part cements known as "second generation acrylic adhesives" look quite promising. The two parts are not mixed, but are applied separately to the two substrates to be joined. Setup time is less than 5 minutes. Weathering data are limited, but are positive to date. Tensile, shear, and weathering tests performed at Thermo Electron are all favorable. Use of this assembly method will require a new edge detail on the domed lenses, and the mating portion of the module box. This is indicated in the expanded details in Figure 7.5 and in detail "A" of Figure 7.3.

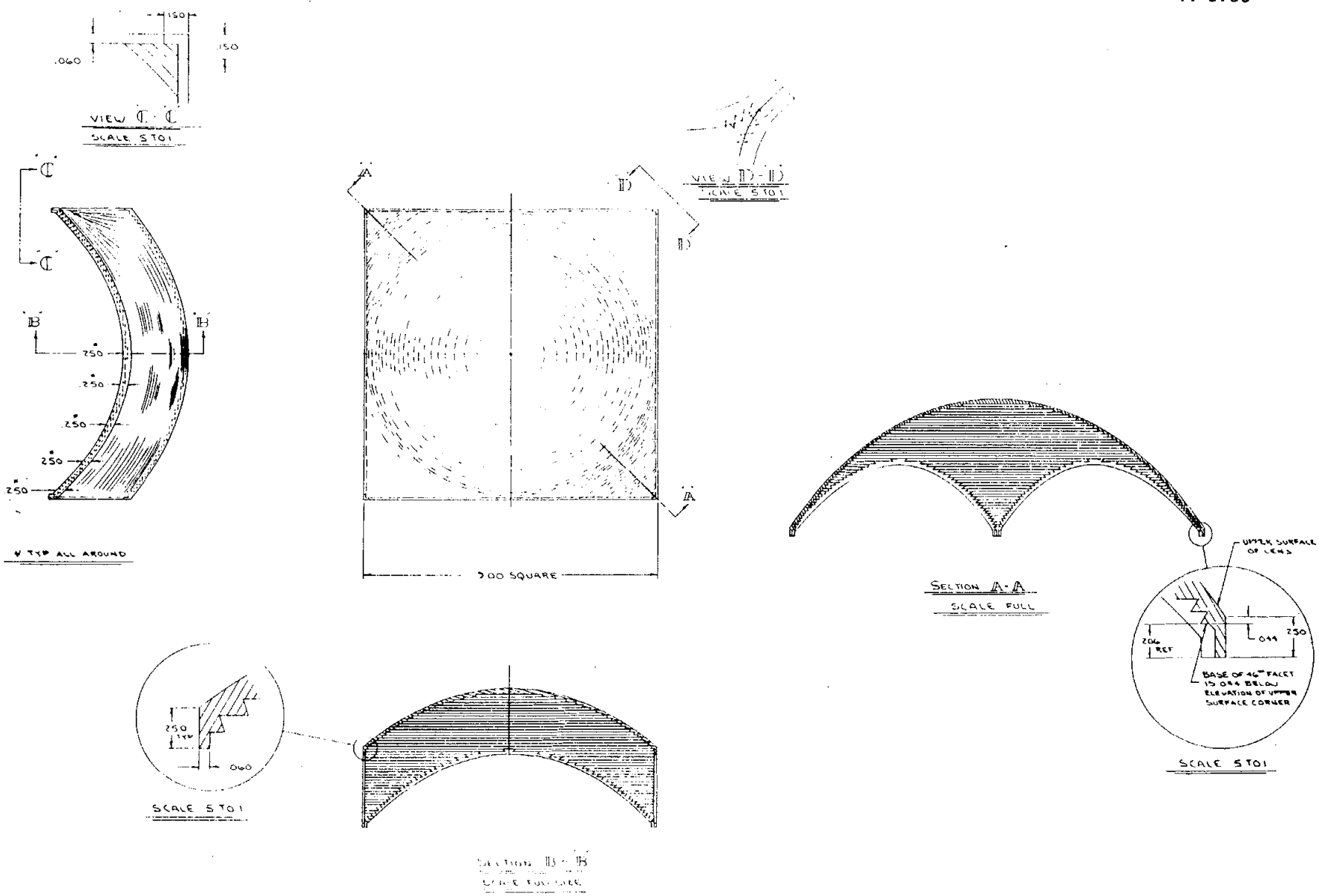

Figure 7.5 Domed Fresnel Lens - Adhesive Bonding Edge Detail

8. INSTRUMENTATION

Instrumentation to support the development work of the program was designed, fabricated, and has been utilized during experiments. This instrumentation includes a laser lens analyzer, an electronic load, a direct/diffuse/total radiation monitor, and adaptations to the electronic load to allow measurement of cell junction temperature when the cell is being heated either electrically or by light. The laser lens analyzer was described in Chapter 4 but the remaining instrumentation is described in the following sections.

8.1 ELECTRONIC LOAD

The electronic load, shown in Figure 8.1 (the schematic is shown in Figure 8.2), was designed to test both cells and modules with voltages up to 15 volts and currents up to 35 amps. Minor modifications will allow the instrument to measure module voltages up to 35 volts. The present full-scale values are 1 volt, 10 volts, 2 amps, and 20 amps, with independent current and voltage ranges. Voltage, current, and power outputs are available in a 0 to 10 V analog output and from a digital readout. Operation of the load can be extended into all four quadrants if desired. Circuitry has been provided to locate and track the peak power point of a cell or module. A speed selectable ramp is provided for data acquisition and x-y recorder plots. The ramp is configured to maintain a constant pen speed for x-y recorders.

8.2 DIRECT/DIFFUSE RADIATION MONITOR

An improvement over the conventional method for measuring direct radiation, by using a collimator, was sought because of the intrinsic potential for measurement error with that method. The instrument that was developed measures total radiation with a silicon photodiode, then blocks the direct radiation by an opaque disk to obtain a measurement of diffuse radiation. The difference between these two measurements is the direct

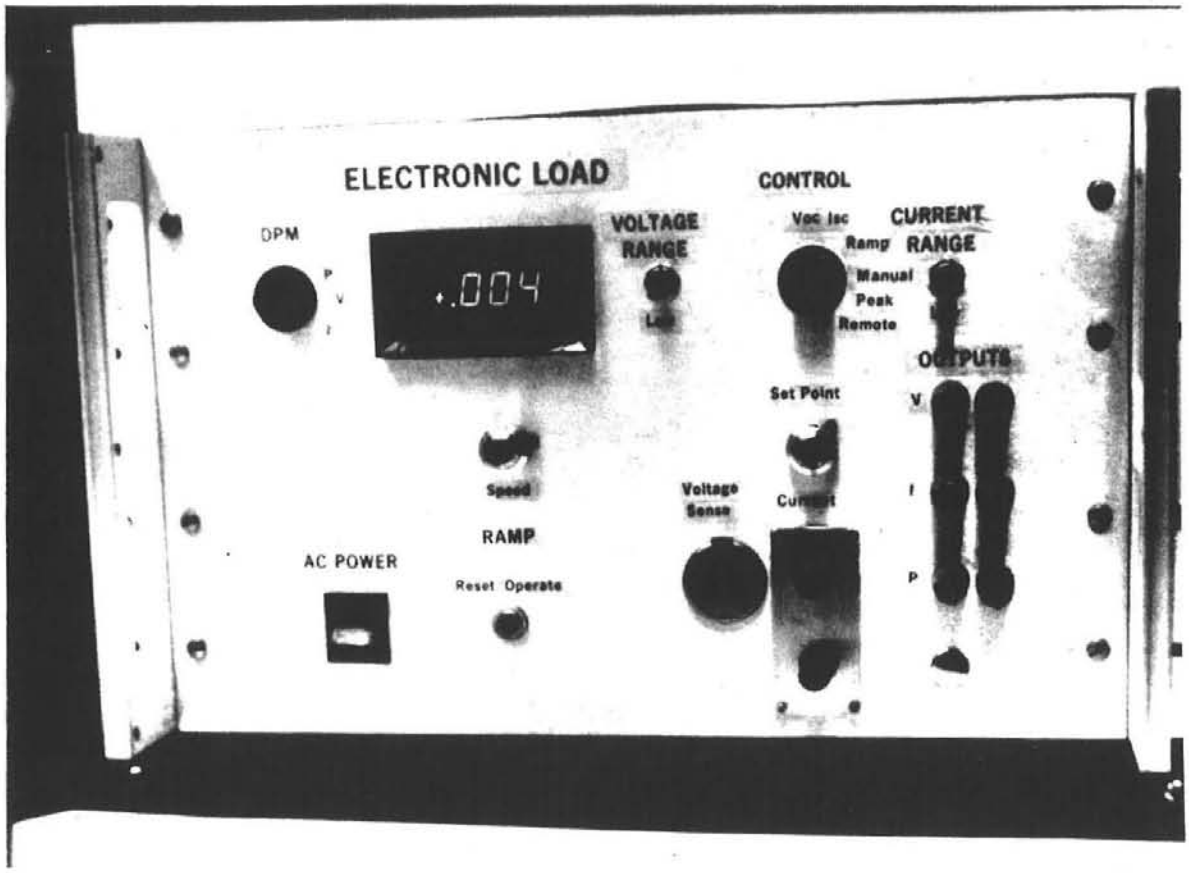

Figure 8.1 Electronic Load

A-6058

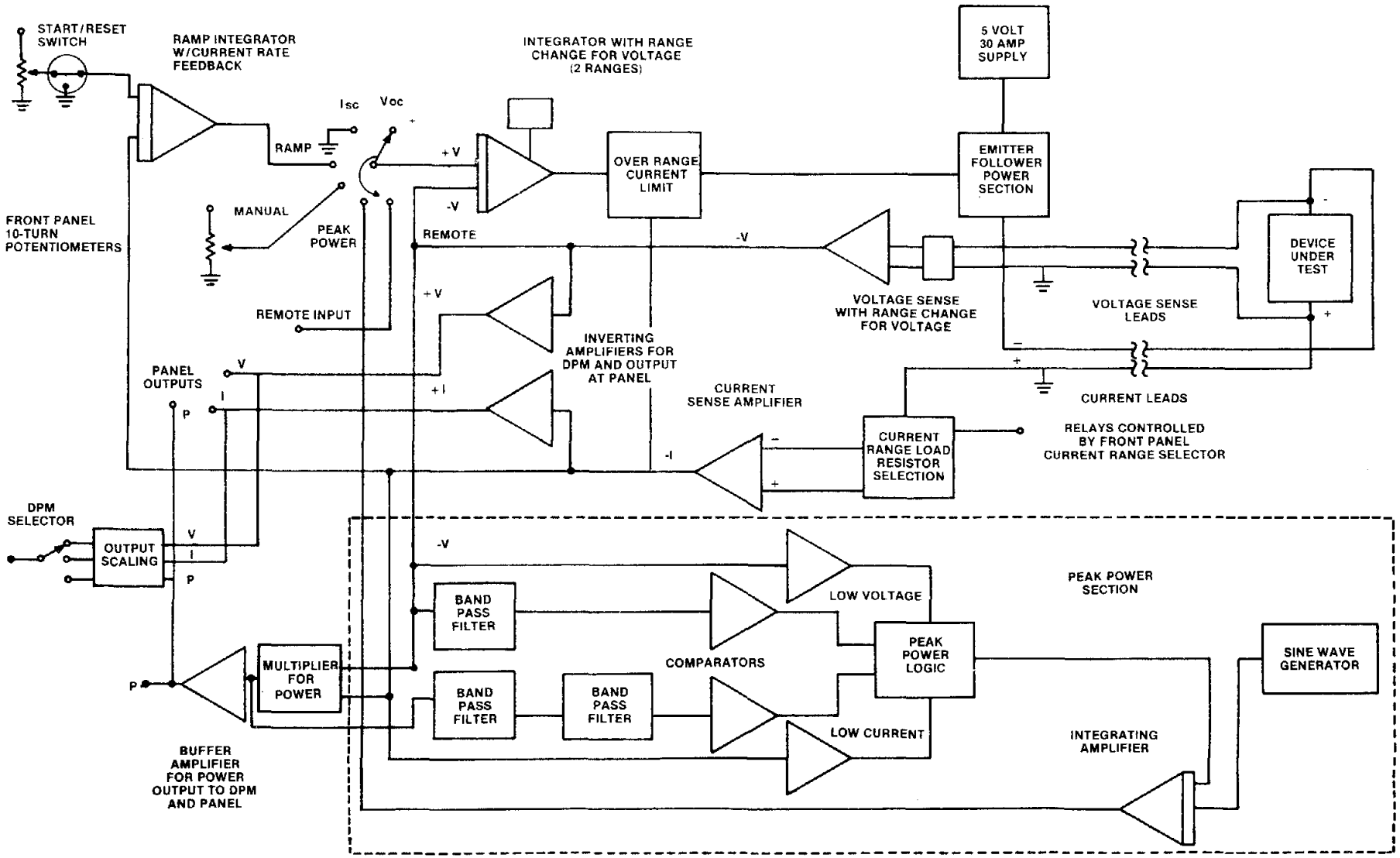

Figure 8.2 Electronic Load

radiation. A schematic of the instrument is shown in Figure 8.3, and a schematic of the circuitry is shown in Figure 8.4. The total and diffuse measurements are updated every 2 seconds and held by sample and hold circuits to allow a continuous monitoring of their values as well as their difference - the direct radiation. The photodiode current is temperature compensated by a temperature sensitive resistor mounted in close thermal contact with the photodiode. The time between total and diffuse measurements is minimized by the quick return action of the mechanization. This configuration was selected because it minimizes the error of measuring direct radiation. The instrument cover is removed for data taking to further reduce errors. The size and height of the shading disk can be selected to match the acceptance angle of a particular collector if desired. Figure 8.5 shows a photograph of this instrument.

8.3 CELL JUNCTION TEMPERATURE MEASUREMENT

The junction temperature of a photovoltaic cell can be measured directly by observing the forward voltage under conditions of constant junction current. The open circuit voltage is a linear function of temperature and the junction current can be maintained at a constant level by either maintaining constant illumination or by passing a constant current through the cell.

The electronic load was adapted to allow cell junction temperature to be measured under two modes of steady-state heating conditions. The first mode realized the heating by inducing a forward current through the cell. This heating current was interrupted for 1.5 msec, during which a forward measurement current of 1 amp was induced. A sample and hold circuit was activated after the forward voltage achieved steady-state conditions (approximately 1 msec). During this measurement interval the temperature of the cell remains constant due to the thermal mass and the short time of the measurement transient. The cell is calibrated by setting the heating current to zero and flowing water of different temperatures

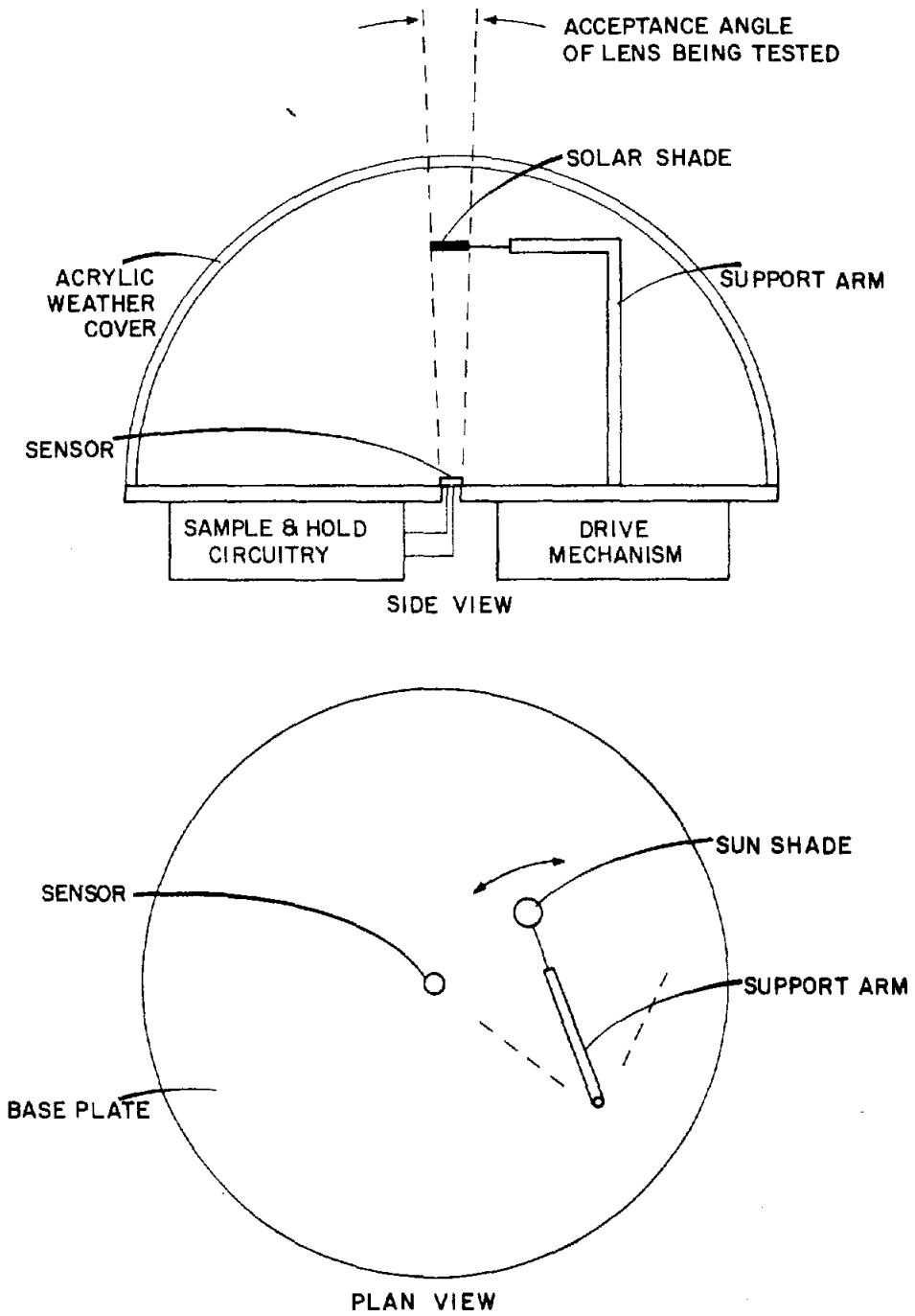

Figure 8.3 Schematic of Direct/Diffuse/Total Radiation Monitor

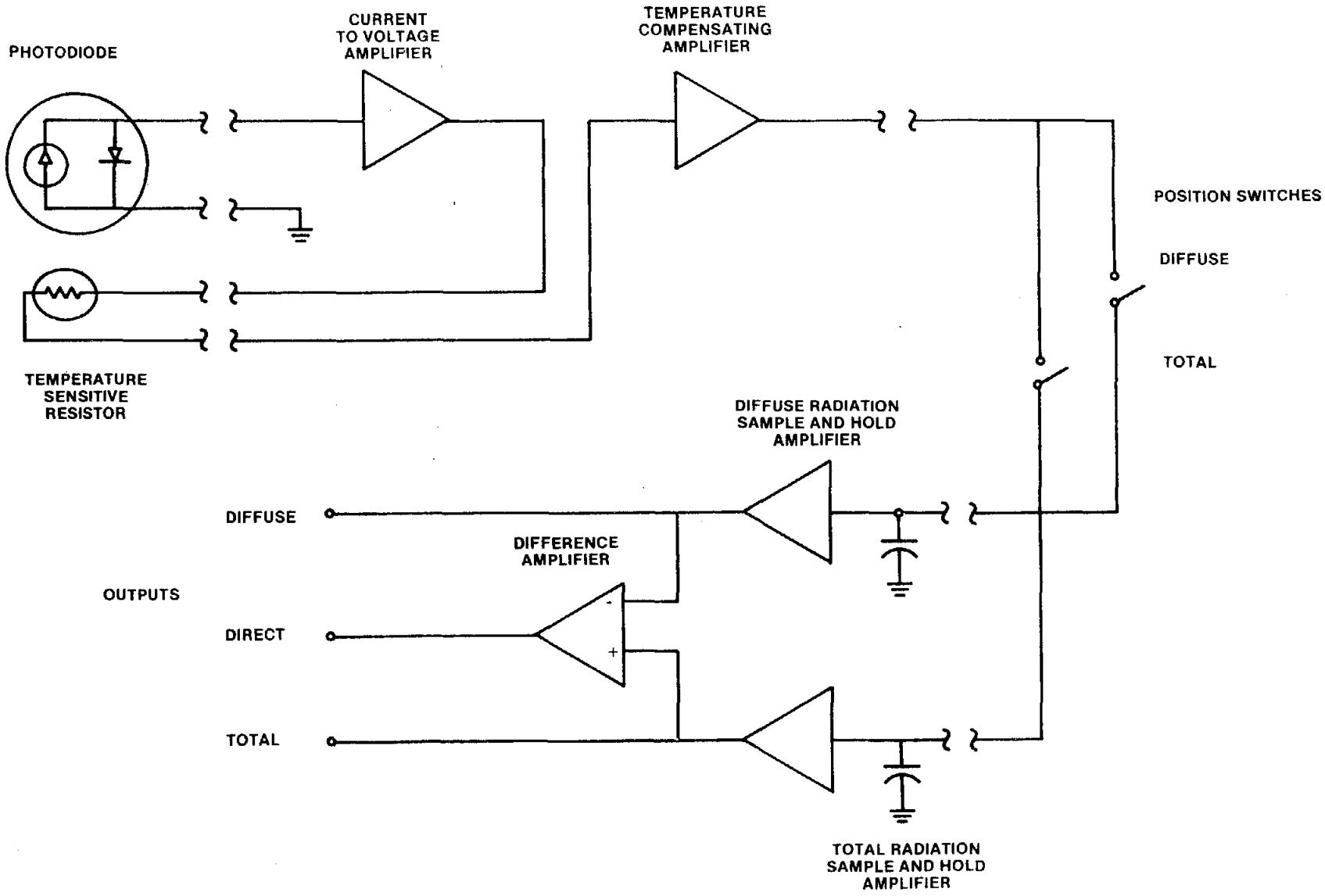

Figure 8.4 Schematic of Direct/Diffuse/Total Radiation Monitor

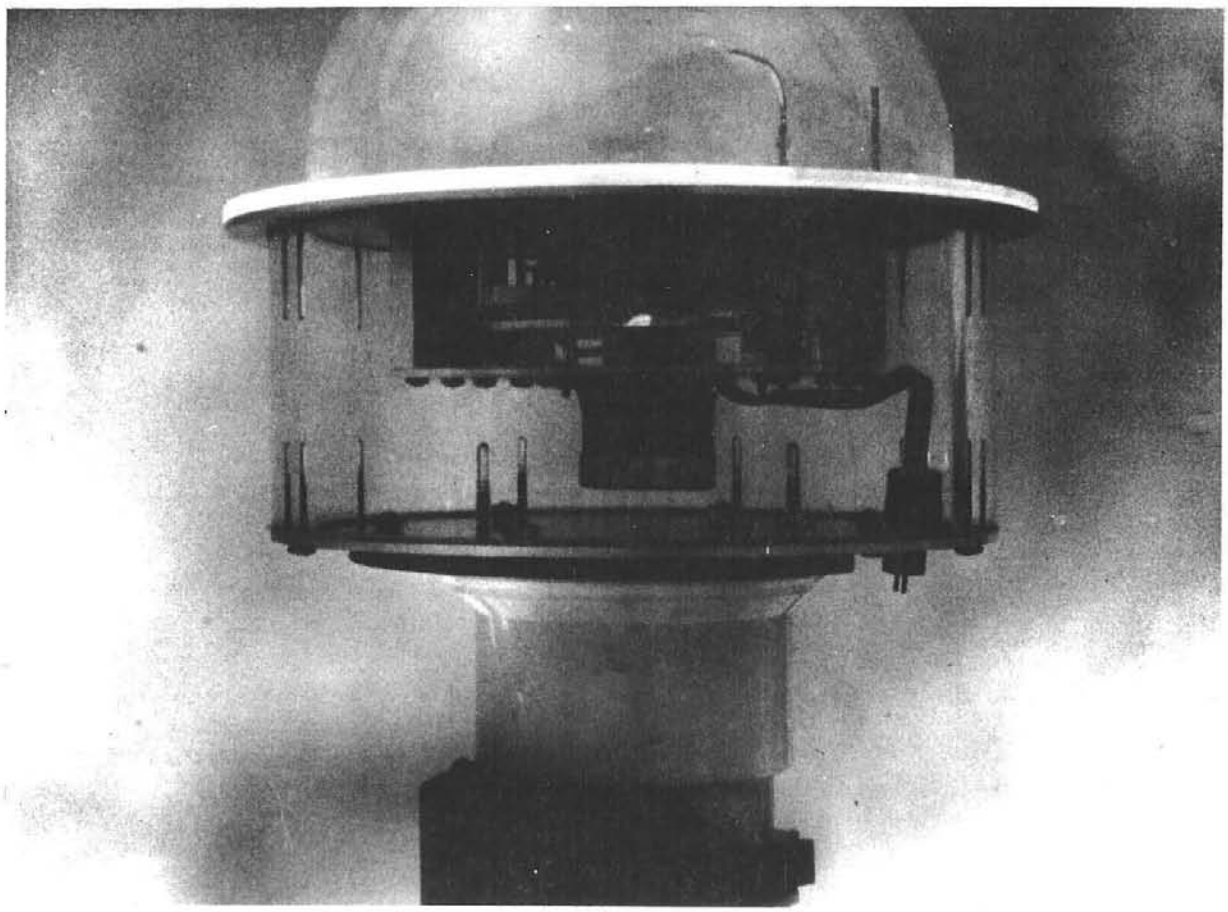

Figure 8.5 Direct/Diffuse/Total Radiation Monitor

through the heat sink. Figure 8.6 shows the calibration curve, oscilloscope traces of the current and voltage during the measurement transient, and the results during cell heating. Figure 8.7 shows the schematic for system operation.

The second mode of thermal impedance measurement involves the use of concentrated sunlight and an optical chopper, as shown in Figure 8.8. Two photodiodes, which are positioned on the housing of the optical chopper, serve as position encoders to control operation of the electronic load and sample and hold circuitry. When the cell under test is fully illuminated by the concentrated light, the electronic load operates in a short circuit current mode so that the level of incoming heat can be measured. When the cell becomes shaded, the electronic load operates in an open circuit mode and a 1 amp forward current is induced in the cell to measure the forward voltage. The light is chopped at a 10-Hz rate and the duty cycle is 95 percent. Figure 8.7 shows a schematic of the electronics and Figure 8.9 shows the oscilloscope waveforms for the position sensors and for the cell voltages and currents.

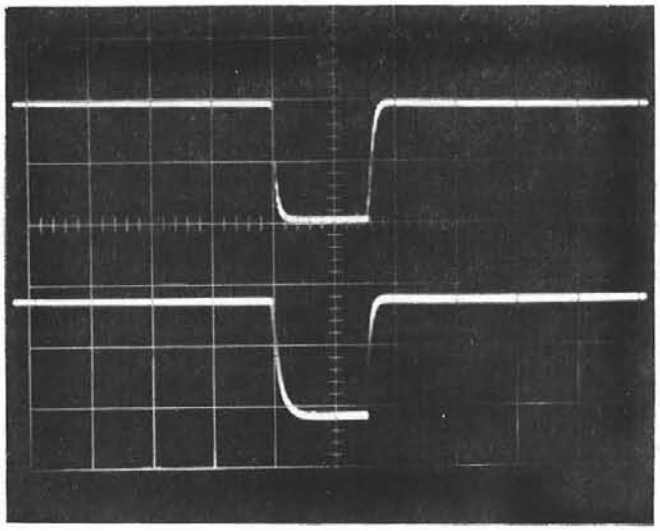

CELL CURRENT (UPPER TRACE)
10 AMPS/DIV.
CELL VOLTAGE (LOWER TRACE)
0.2 VOLTS/DIV.
TIME BASE = 1 MSEC./DIV.

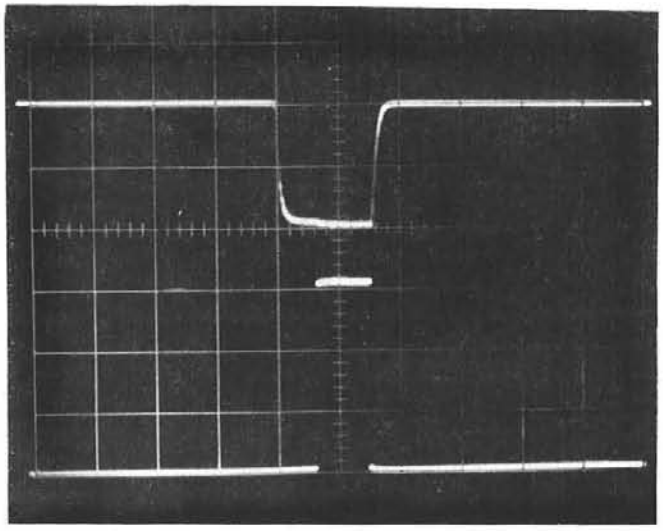

CELL CURRENT (UPPER TRACE)
10 AMPS/DIV.
SAMPLE + HOLD PULSE (LOWER TRACE)
5 VOLTS/DIV.
TIME BASE = 1 MSEC/DIV.

CALIBRATION CURVE

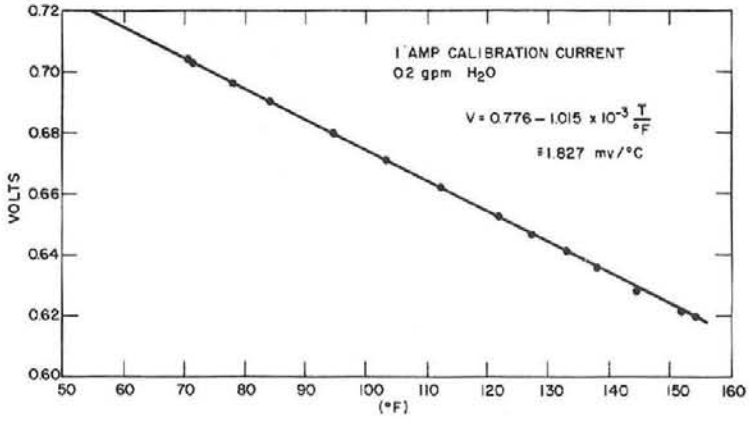

THERMAL IMPEDANCE CURVE

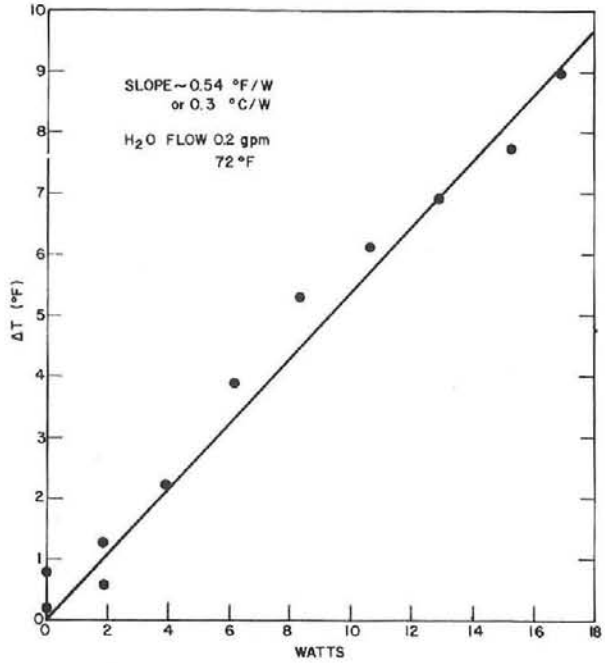

Figure 8.6 Thermal Impedance Measurement Technique
Resistive Heating Mode

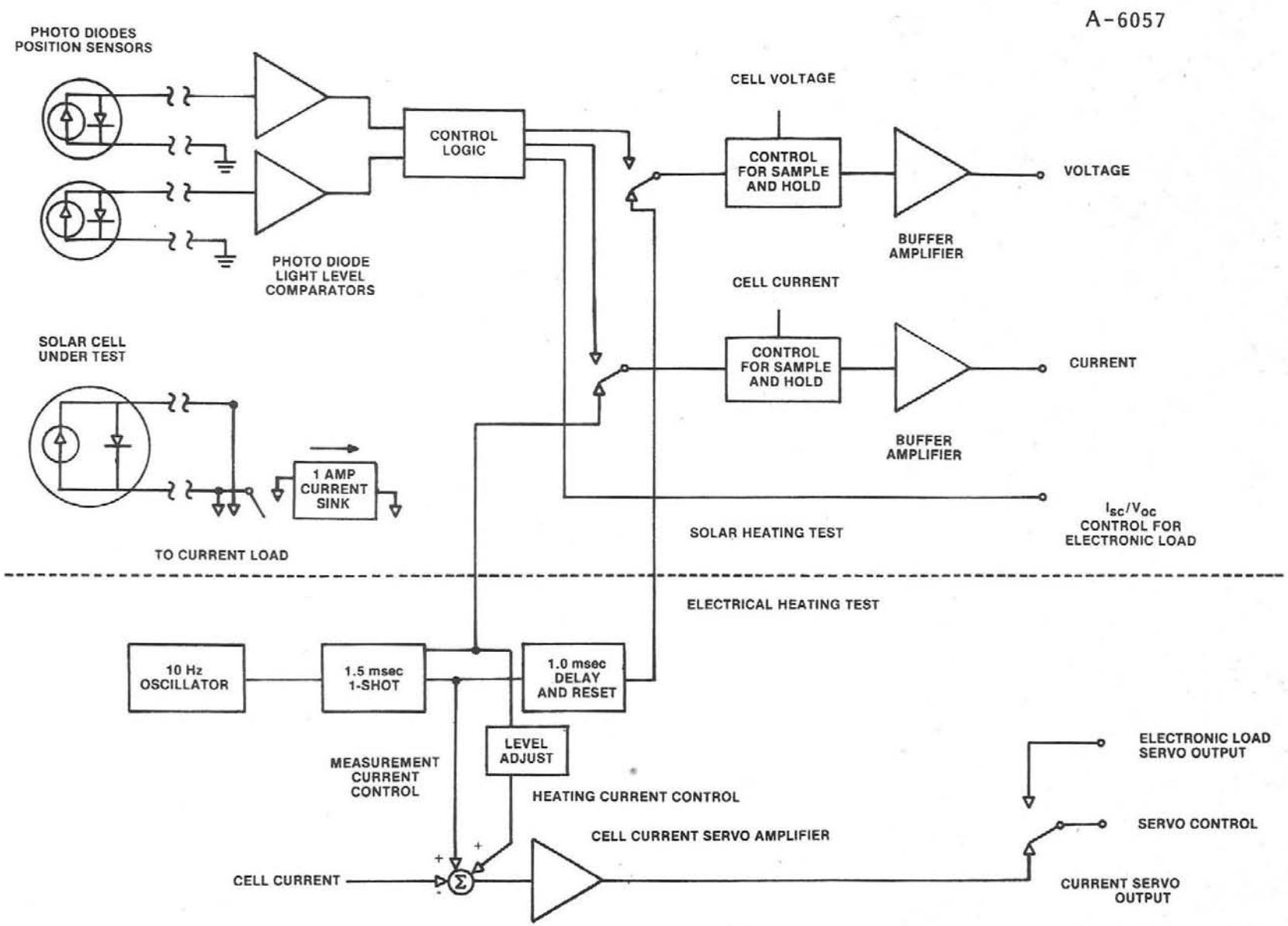

Figure 8.7 Schematic for Cell Junction Temperature Measurement

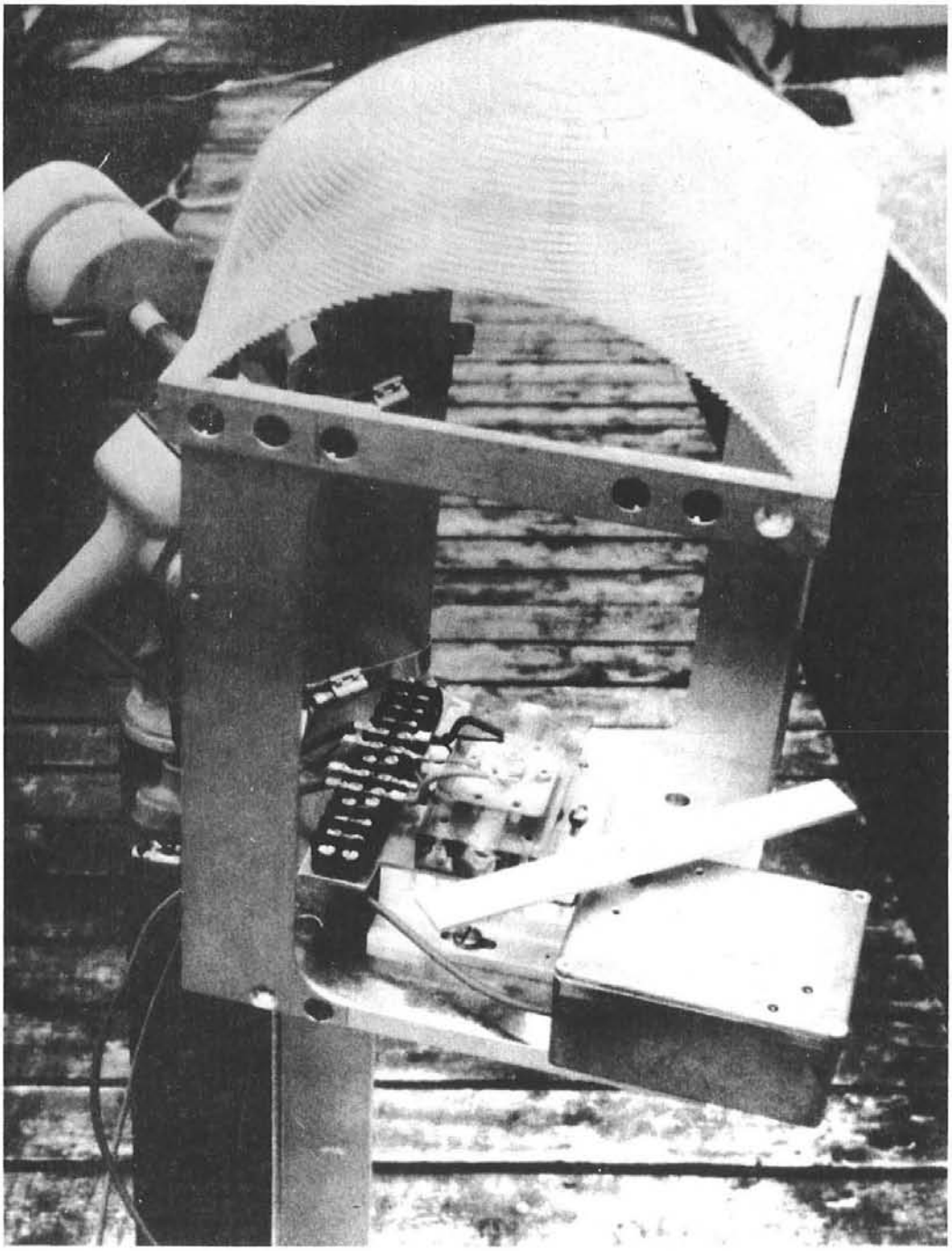

Figure 8.8 Optical Chopper for Cell Temperature Measurement

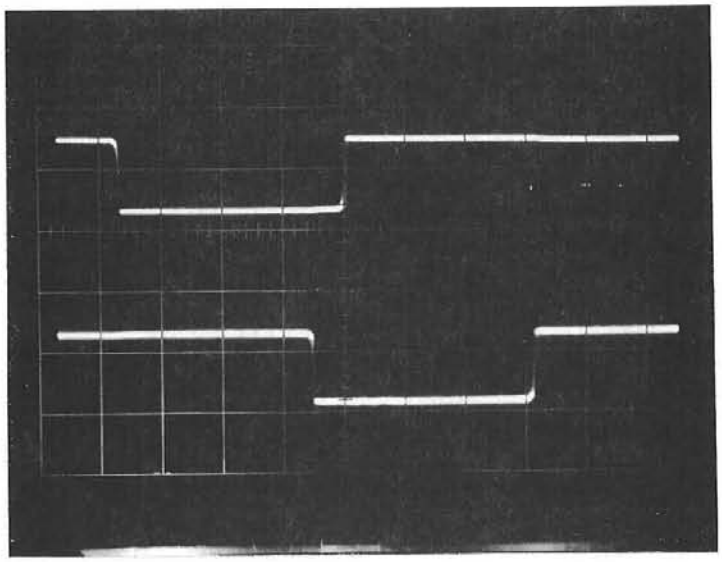

Signals from shade position sensors sample and hold circuit triggered when both are low. Time Base = 2.0 ms/Div.

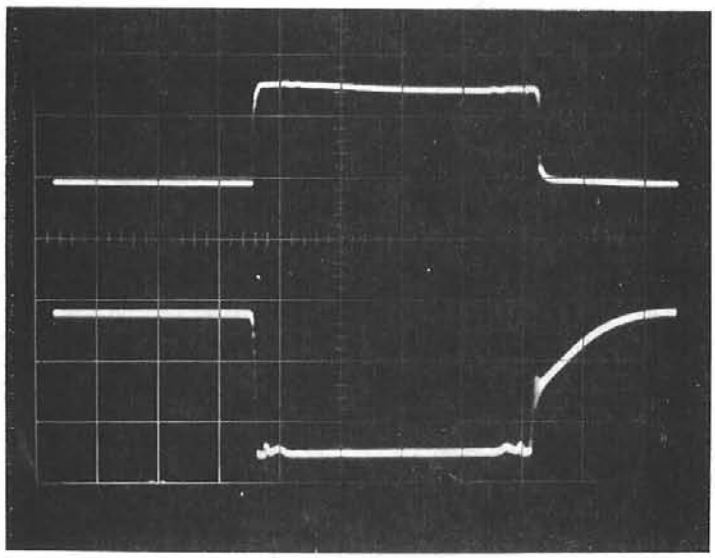

Cell Voltage (upper trace) 0.5 volts/Div.
O V at I_{sc} to 0.7V at I_{test}
Cell Current (lower trace) 2.0 amp/Div.
3.5A at I_{sc} to -1.0A at I_{test}
Time Base = 2.0 ms/Div.

Figure 8.9 Oscilloscope Waveforms During Cell Junction Temperature Measurement Under Solar Heating

9. ANNUAL ENERGY EVALUATION

In order to assess the effects of the various parameters that influence module performance, a computer model of module operation was developed. Tracking angle limits, local latitude, lens and PV cell performance characteristics, and thermal system parameters can be varied to represent a diversity of system configurations. Both active and passive cooling schemes are accommodated.

Realistic module operation is simulated using hourly data from the Typical Meteorological Year (TMY) weather tapes as input.

The overall program structure consists of an initialization and parameter input section; three nested loops which step through the hours, days, and months of the year; and a data output section. Performance data can be generated in the following formats:

- Hourly, for any day of the year
- Daily, for any month of the year
- Monthly, for the whole year
- Annual summary only

Examples of these for Albuquerque, N.M. are reproduced in Figures 9.1 through 9.3. All energy inputs and outputs are kWh/m^2, time is hours and decimal fractions, and temperatures are degrees Celsius. The energy outputs are slightly conservative as the simulation currently allows no energy collection after the first intermodule shading in the afternoon, and until intermodule shading completely ends the following morning.

A pass through the program for a single hour encompasses the following steps. The direct normal radiation received in the last hour is read from the TMY data array. The array is four dimensional, and uses the month, day, hour, and type of data as its subscripts. If the direct normal radiation is less than 1 W/m^2, the hour loop parameter is incremented and program execution passes to the next hour.

1

DATE	HOUR	DIRECT INSOL.	AVAIL. TO COL.	LIMITED BY	LIMIT TIME	SUNRISE/ SUNSET	ELEC. OUTPUT	THERMAL OUTPUT	CELL TEMP.	DB TEMP.	DELTA T CELL-DB	WB TEMP.	H2O TEMP.	DELTA T CELL-H2O
7/ 2	5	0.00	0.00	MTA			0.00	0.00	14.1	21.1	-7.0	9.1	14.1	0.00
7/ 2	6	0.31	0.00	MTA	6.02	4.85	0.00	0.00	14.1	21.1	-7.0	9.1	14.1	0.00
7/ 2	7	0.48	0.47	MTA	6.02	4.85	0.08	0.28	21.1	21.1	0.0	10.1	16.2	4.84
7/ 2	8	0.71	0.71				0.12	0.42	25.4	24.4	1.0	11.4	18.1	7.29
7/ 2	9	0.79	0.79				0.13	0.46	28.2	27.2	1.0	13.2	20.1	8.07
7/ 2	10	0.83	0.83				0.14	0.49	30.5	30.0	0.5	15.0	22.0	8.50
7/ 2	11	0.84	0.84				0.14	0.49	29.8	32.2	-2.4	14.2	21.2	8.60
7/ 2	12	0.82	0.82				0.14	0.49	30.5	35.0	-4.5	15.0	22.0	8.47
7/ 2	13	0.78	0.78				0.13	0.46	32.1	37.2	-5.1	17.2	24.1	8.00
7/ 2	14	0.82	0.82				0.14	0.48	32.6	37.2	-4.6	17.2	24.2	8.44
7/ 2	15	0.82	0.82				0.14	0.48	32.3	38.9	-6.6	16.9	23.9	8.39
7/ 2	16	0.77	0.77				0.13	0.46	31.8	38.9	-7.1	16.9	23.8	7.96
7/ 2	17	0.70	0.70				0.12	0.41	31.2	38.3	-7.1	17.3	24.0	7.19
7/ 2	18	0.76	0.75	MTA	17.98	19.15	0.12	0.44	31.2	36.7	-5.5	16.7	23.5	7.67
7/ 2	19	0.19	0.00	MTA	17.98	19.15	0.00	0.00	22.0	35.0	-13.0	17.0	22.0	0.00
7/ 2	20	0.00	0.00	MTA			0.00	0.00	21.8	32.8	-11.0	16.8	21.8	0.00

DO YOU WISH TO CONTINUE ?

:

DATE	HOUR	DIRECT INSOL.	AVAIL. TO COL.	LIMITED BY	LIMIT TIME	SUNRISE/ SUNSET	ELEC. OUTPUT	THERMAL OUTPUT	CELL TEMP.	DB TEMP.	DELTA T CELL-DB	WB TEMP.	H2O TEMP.	DELTA T CELL-H2O
7/ 3	5	0.00	0.00	MTA			0.00	0.00	19.0	25.0	-6.0	14.0	19.0	0.00
7/ 3	6	0.25	0.00	MTA	6.02	4.85	0.00	0.00	18.9	23.9	-5.0	13.9	18.9	0.00
7/ 3	7	0.25	0.25	MTA	6.02	4.85	0.04	0.15	23.3	26.1	-2.8	15.1	20.7	2.55
7/ 3	8	0.87	0.87				0.15	0.52	32.0	28.9	3.1	15.9	23.0	8.99
7/ 3	9	0.96	0.96				0.16	0.57	34.0	31.7	2.3	16.7	24.1	9.94
7/ 3	10	0.99	0.99				0.16	0.59	34.6	33.9	0.7	16.9	24.3	10.22
7/ 3	11	0.99	0.99				0.16	0.59	35.1	34.4	0.7	17.4	24.8	10.26
7/ 3	12	1.00	1.00				0.16	0.59	35.3	35.6	-0.3	17.6	25.0	10.28
7/ 3	13	0.99	0.99				0.16	0.59	35.9	37.2	-1.3	18.2	25.6	10.25
7/ 3	14	1.00	1.00				0.17	0.59	35.6	37.8	-2.2	17.8	25.3	10.36
7/ 3	15	0.99	0.99				0.16	0.59	33.7	40.0	-6.3	16.0	23.4	10.23
7/ 3	16	0.93	0.93				0.15	0.55	33.2	39.4	-6.2	16.4	23.7	9.56
7/ 3	17	0.75	0.75				0.12	0.44	31.4	38.9	-7.5	16.9	23.7	7.69
7/ 3	18	0.61	0.60	MTA	17.98	19.15	0.10	0.35	29.3	36.7	-7.4	16.7	23.2	6.11
7/ 3	19	0.09	0.00	MTA	17.98	19.15	0.00	0.00	21.6	35.6	-14.0	16.6	21.6	0.00
7/ 3	20	0.00	0.00	MTA			0.00	0.00	20.9	33.9	-13.0	15.9	20.9	0.00

DO YOU WISH TO CONTINUE ?

1

DATE	HOUR	DIRECT INSOL.	AVAIL. TO COL.	LIMITED BY	LIMIT TIME	SUNRISE/ SUNSET	ELEC. OUTPUT	THERMAL OUTPUT	CELL TEMP.	DB TEMP.	DELTA T CELL-DB	WB TEMP.	H2O TEMP.	DELTA T CELL-H2O
7/ 4	5	0.00	0.00	MTA			0.00	0.00	16.6	25.6	-9.0	11.6	16.6	0.00
7/ 4	6	0.10	0.00	MTA	6.02	4.86	0.00	0.00	16.4	24.4	-8.0	11.4	16.4	0.00
7/ 4	7	0.62	0.61	MTA	6.02	4.86	0.10	0.36	26.4	26.7	-0.3	13.7	20.2	6.23
7/ 4	8	0.77	0.77				0.13	0.45	28.0	27.2	0.8	13.2	20.1	7.89
7/ 4	9	0.93	0.93				0.15	0.55	31.8	30.0	1.8	15.0	22.3	9.55
7/ 4	10	0.98	0.98				0.16	0.58	32.7	32.2	0.5	15.2	22.6	10.13
7/ 4	11	0.99	0.99				0.16	0.59	33.9	33.3	0.6	16.3	23.7	10.21
7/ 4	12	0.99	0.99				0.16	0.59	34.7	36.1	-1.4	17.1	24.5	10.21
7/ 4	13	0.98	0.98				0.16	0.58	35.7	37.2	-1.5	18.2	25.6	10.12
7/ 4	14	0.89	0.89				0.15	0.53	34.6	38.3	-3.7	18.3	25.5	9.17
7/ 4	15	0.13	0.13				0.02	0.08	24.9	37.2	-12.3	18.2	23.5	1.36
7/ 4	16	0.57	0.57				0.10	0.34	31.0	36.7	-5.7	18.7	25.1	5.88
7/ 4	17	0.00	0.00				0.00	0.00	23.0	35.0	-12.0	18.0	23.0	0.01
7/ 4	18	0.00	0.00	MTA	17.98	19.14	0.00	0.00	22.7	31.7	-9.0	17.7	22.7	0.00
7/ 4	19	0.00	0.00	MTA			0.00	0.00	21.2	27.2	-6.0	16.2	21.2	0.00
7/ 4	20	0.00	0.00	MTA			0.00	0.00	21.2	27.2	-6.0	16.2	21.2	0.00

DO YOU WISH TO CONTINUE ?

Figure 9.1 Hourly Performance Data

DATE	DIRECT INSOL.	AVAIL. TO COL.	LIMITED BY	LIMIT TIME	SUNSET HOUR	ELEC OUTPUT	% OF AVAIL.	THERMAL OUTPUT	% OF AVAIL.	TOTAL OUTPUT	% OF AVAIL.
7/ 1	10.72	10.35	MTA	17.98	19.16	1.72	16.6	6.11	59.1	7.83	75.7
7/ 2	9.61	9.10	MTA	17.98	19.15	1.52	16.7	5.36	59.0	6.89	75.7
7/ 3	10.69	10.34	MTA	17.98	19.15	1.71	16.6	6.11	59.1	7.82	75.7
7/ 4	7.96	7.85	MTA	17.98	19.14	1.31	16.6	4.64	59.1	5.95	75.7
7/ 5	8.45	8.02	MTA	17.98	19.14	1.33	16.6	4.74	59.1	6.07	75.7
7/ 6	11.39	10.86	MTA	17.98	19.13	1.80	16.6	6.42	59.1	8.22	75.7
7/ 7	8.12	8.09	MTA	17.98	19.13	1.35	16.7	4.78	59.0	6.13	75.7
7/ 8	7.20	6.93	MTA	17.98	19.12	1.15	16.6	4.10	59.1	5.24	75.7
7/ 9	9.39	9.20	MTA	17.98	19.11	1.54	16.7	5.43	59.0	6.97	75.7
7/10	4.54	4.51	MTA	17.98	19.10	0.76	16.8	2.66	58.9	3.41	75.7
7/11	8.32	8.25	MTA	17.98	19.10	1.37	16.6	4.87	59.1	6.24	75.7
7/12	5.76	5.69	MTA	17.84	19.09	0.95	16.7	3.36	59.0	4.31	75.7
7/13	8.32	8.19	MTA	17.76	19.08	1.36	16.5	4.85	59.1	6.20	75.7
7/14	8.67	8.40	MTA	17.70	19.07	1.40	16.6	4.96	59.1	6.36	75.7
7/15	4.04	4.03	MTA	17.65	19.06	0.67	16.7	2.38	59.1	3.05	75.7
7/16	6.77	6.26	MTA	17.61	19.05	1.04	16.6	3.70	59.1	4.74	75.7
7/17	10.00	9.38	MTA	17.57	19.04	1.55	16.5	5.55	59.2	7.10	75.7
7/18	8.30	7.97	MTA	17.53	19.03	1.32	16.6	4.72	59.1	6.04	75.7
7/19	5.97	5.42	MTA	17.49	19.02	0.90	16.6	3.20	59.1	4.10	75.7
7/20	6.05	5.95	MTA	17.46	19.01	0.99	16.7	3.51	59.1	4.50	75.7
7/21	7.85	7.59	MTA	17.42	19.00	1.27	16.7	4.47	59.0	5.74	75.7
7/22	8.32	7.74	MTA	17.39	18.99	1.28	16.6	4.57	59.1	5.86	75.7
7/23	6.54	6.44	MTA	17.36	18.98	1.07	16.6	3.81	59.1	4.88	75.7
7/24	5.46	5.05	MTA	17.33	18.97	0.84	16.6	2.98	59.1	3.82	75.7
7/25	2.84	2.81	MTA	17.30	18.95	0.47	16.7	1.66	59.0	2.13	75.7
7/26	7.73	7.66	MTA	17.27	18.94	1.27	16.5	4.53	59.2	5.80	75.7
7/27	7.68	7.25	MTA	17.25	18.93	1.20	16.6	4.28	59.1	5.49	75.7
7/28	9.13	8.27	MTA	17.22	18.92	1.37	16.6	4.89	59.1	6.26	75.7
7/29	8.70	8.41	MTA	17.19	18.90	1.39	16.5	4.98	59.2	6.36	75.7
7/30	5.68	5.45	MTA	17.17	18.89	0.90	16.6	3.22	59.1	4.12	75.7
7/31	8.46	7.54	MTA	17.14	18.88	1.25	16.6	4.46	59.1	5.71	75.7

DO YOU WISH TO CONTINUE ?

Figure 9.2 Daily Performance Data

MONTH ENDING	DIRECT INSOL.	AVAIL. TO COL.	% AVAIL.	# DAYS MTA HIT	# DAYS CRA HIT	# DAYS SSA HIT	ELEC. OUTPUT	% OF AVAIL.	THERMAL OUTPUT	% OF AVAIL.	TOTAL OUTPUT	% OF AVAIL.
1/31	165.6	149.1	90.0	0	0	31	26.1	17.5	86.9	58.3	113.1	75.8
2/29	174.1	165.4	95.0	11	0	18	28.9	17.5	96.5	58.4	125.4	75.8
3/31	203.4	184.2	90.6	31	0	0	32.0	17.4	107.6	58.4	139.6	75.8
4/30	238.9	215.1	90.0	30	0	0	36.9	17.1	126.1	58.6	163.0	75.8
5/31	266.2	239.9	90.1	31	0	0	40.7	17.0	141.0	58.8	181.7	75.7
6/30	265.1	251.1	94.7	30	0	0	42.3	16.8	147.9	58.9	190.2	75.7
7/31	238.7	229.0	95.9	31	0	0	38.0	16.6	135.3	59.1	173.3	75.7
8/31	243.1	215.6	88.7	31	0	0	35.9	16.7	127.3	59.0	163.2	75.7
9/30	218.8	193.2	88.3	30	0	0	32.5	16.8	113.8	58.9	146.3	75.7
10/31	229.3	219.0	95.5	23	0	8	37.3	17.1	128.6	58.7	165.9	75.8
11/30	191.5	177.3	92.6	0	0	30	30.8	17.4	103.6	58.4	134.4	75.8
12/31	181.5	153.2	84.4	0	0	31	26.9	17.5	89.3	58.3	116.1	75.8

********** ANNUAL SUMMARY **********

		# OF TIMES HIT DURING YR
EAST-WEST HORIZONTAL TRACKING LIMIT		
MODULE TILT ANGLE LIMIT OF +/-	68.00	248
COLUMN ROTATION ANGLE LIMIT OF +/-	90.00	0
SOUTHERLY SHADING ANGLE LIMIT OF +/-	20.00	118

DIRECT INSOL.	AVAILABLE TO COLLECTOR	% AVAIL.	ELECTRICAL OUTPUT	% OF AVAIL.	THERMAL OUTPUT	% OF AVAIL.	TOTAL OUTPUT	% OF AVAIL.
2616.3	2392.1	91.4	408.3	17.1	1404.0	58.7	1812.3	75.8

Figure 9.3 Monthly and Annual Performance Data

If the direct insolation is greater than 1 W/m^2, the program checks for intermodule shading. Shading can occur if the sun's position relative to the collector exceeds the module tilt angle limit (MTA), the column rotation angle limit (CRA), or the southerly shading angle limit (SSA). If one of these limits is encountered, a counter for that limit is incremented. Only one limit can be encountered in a day, and it can only be incremented once per day. If the current hour is before the morning limit hour (or after the afternoon limit hour) the hour loop parameter is incremented and execution passes to the next hour.

Direct insolation received in the limit hour, either in the morning or in the afternoon, is assumed to have a triangular distribution. That is, it increases (or decreases) linearly from the value for the previous hour to the value for the limit hour. The simulation distinguishes six limit hour cases, and determines the appropriate distribution and the amount of insolation available to the collector for that limit hour. The six cases are:

1. Sunrise Hour = Morning Limit Hour
2. Sunset Hour = Afternoon Limit Hour
3. Sunrise Hour = Morning Limit Hour -1
4. Sunset Hour = Afternoon Limit Hour +1
5. Sunrise Hour = Morning Limit Hour -2
6. Sunset Hour = Afternoon Limit Hour +2

In this manner, energy available to the collector in the partial hours at the beginning and end of the collecting day is credited.

After the amount of energy available to the collector in the hour has been determined, it is multiplied by the lens efficiency to calculate the energy available at the cell in that hour. Next, the thermal and electrical outputs are developed. This is an iterative process as the cell temperature affects the electrical output and the electrical output affects the amount of energy remaining as heat.

If the collector being modeled has active cooling, the cell temperature is based on the energy input, the ambient wet bulb temperature, the conductivities of the cell mount and heat sink, the number of cells in fluid series, the coolant flow rate, and the heat removal capacity of the thermal load. Since wet bulb temperature is not provided on the TMY tapes, it must be iteratively calculated from the dry bulb temperature and the dew point temperature.

For passively cooled systems, the cell temperature is based on the energy input, the dry bulb temperature, and the conductivities of the cell mount and heat sink. The heat sink conductivity is a function of energy input, ambient dry bulb temperature, and wind speed.

After energy and temperature balances have been achieved by the iterative subroutines, the electrical and thermal outputs for the current hour are printed and/or summed into the daily energy output totals, depending on the output format selected by the program user. Program execution then passes to the next hour.

9.1 RESULTS

One result of note is that there is very little loss in electrical output between an actively cooled module and a passively cooled one, other factors being equal. This is due in part to the fact that most of the energy is available at wind speeds above 1 m/sec. Figure 9.4 shows energy availability matrices for Albuquerque, New Mexico, and Santa Maria, California. Passive heat sinks designed to operate at the thermal flux and wind speed associated with the maximum energy distribution point result in annual module electrical outputs on the order of 4½ percent lower than their actively cooled counterparts.

Energy Distribution for Albuquerque, New Mexico										
Direct Insol.	Percent of Total Direct Normal									
0.001 - 0.1	0.0	0.0	0.1	0.2	0.1	0.1	0.1	0.1	0.0	0.1
0.1 - 0.2	0.0	0.0	0.2	0.4	0.3	0.2	0.1	0.1	0.1	0.1
0.2 - 0.3	0.1	0.0	0.3	0.4	0.3	0.3	0.1	0.1	0.1	0.2
0.3 - 0.4	0.1	0.0	0.5	0.5	0.5	0.3	0.3	0.1	0.2	0.4
0.4 - 0.5	0.1	0.1	0.4	0.9	0.6	0.2	0.2	0.2	0.2	0.3
0.5 - 0.6	0.2	0.0	0.6	1.1	0.9	0.7	0.3	0.3	0.2	0.5
0.6 - 0.7	0.3	0.0	0.9	1.6	1.4	0.6	0.4	0.3	0.2	0.7
0.7 - 0.8	0.3	0.0	1.5	3.0	2.9	1.3	1.1	0.7	0.7	1.2
0.8 - 0.9	0.9	0.1	3.1	6.1	4.9	2.6	1.5	1.0	0.6	1.2
0.9 - 1.0	1.8	0.3	7.3	11.4	7.4	4.8	3.5	2.3	1.7	3.1
Wind Speed, m/s	<0.1	0.1 - 1	1-2	2-3	3-4	4-5	5-6	6-7	7-8	>8

Energy Distribution for Santa Maria, California										
Direct Insol.	Percent of Total Direct Normal									
0.001 - 0.1	0.2	0.0	0.1	0.3	0.2	0.2	0.2	0.1	0.0	0.0
0.1 - 0.2	0.3	0.0	0.2	0.4	0.4	0.4	0.3	0.2	0.1	0.1
0.2 - 0.3	0.5	0.0	0.3	0.3	0.4	0.3	0.3	0.2	0.1	0.1
0.3 - 0.4	0.5	0.0	0.2	0.4	0.5	0.4	0.4	0.4	0.2	0.3
0.4 - 0.5	0.5	0.0	0.4	0.6	0.9	0.8	0.9	0.4	0.3	0.4
0.5 - 0.6	0.9	0.0	0.5	0.8	1.0	1.2	1.0	0.9	0.3	0.5
0.6 - 0.7	1.2	0.0	0.9	1.5	1.6	1.9	1.9	1.8	0.6	1.2
0.7 - 0.8	1.3	0.0	1.4	2.4	2.8	4.4	4.0	2.8	1.8	2.0
0.8 - 0.9	0.9	0.0	1.3	3.2	5.1	5.8	6.5	5.2	2.9	3.5
0.9 - 1.0	0.1	0.0	0.3	0.9	1.2	1.3	1.6	1.4	0.8	0.7
Wind Speed, m/s	<0.1	0.1 - 1	1-2	2-3	3-4	4-5	5-6	6-7	7-8	>8

Figure 9.4 Energy Distributions Correlated for Insolation and Wind Speed

10. CELL TESTING

Two different types of silicon cells were tested during the program. The module and lens were designed for EMVJ cells from Microwave Associates, but planar junction cells from ASEC were also tested for comparison. The test results for these two cell types are presented in the following sections.

10.1 MICROWAVE ASSOCIATES' EMVJ CELLS

The cell that was designed for this program was a 0.37 in. x 0.37 in. EMVJ cell described in Appendix 1. This cell is shown, mounted for testing, in Figure 10.1. Microwave Associates encountered difficulties fabricating these cells and, due to these problems, substituted their smaller 0.26-in. diameter cells. The 0.26-in. diameter cell is shown in Figure 10.2. Both cell types were tested with the lens designed for the larger cells. Test results for cell TE3-5, a 0.37-in. square cell with a secondary concentrator, are shown in Figure 10.3. The cell currents are low because the antireflection (AR) coating on the Microwave cells is SiO_2 with a quarter wavelength thickness. The glass secondary has the same refractive index as SiO_2, thereby eliminating the effectiveness of the quarter wavelength coating. This problem will be corrected when Microwave Associates completes their work on silicon nitride coatings, which have a higher refractive index. Figure 10.4 shows similar results for a 0.26-in.-diameter cell.

The peak intensities on these cells can reach 3000 suns yet the cells do not show excessively high resistances which would result in low cell fill factors. Fill factors do decrease at high insolation conditions, but the major consistent problem is an apparent shunt resistance probably caused by the loss of conductivity modulation due to high base resistivity (see Appendix 1).

10.2 PLANAR JUNCTION CELLS

Two planar junction cell sizes were tested during the program. The largest cell was an ASEC 2.05 cm x 2.05 cm (Sandia "Strawman" cell).

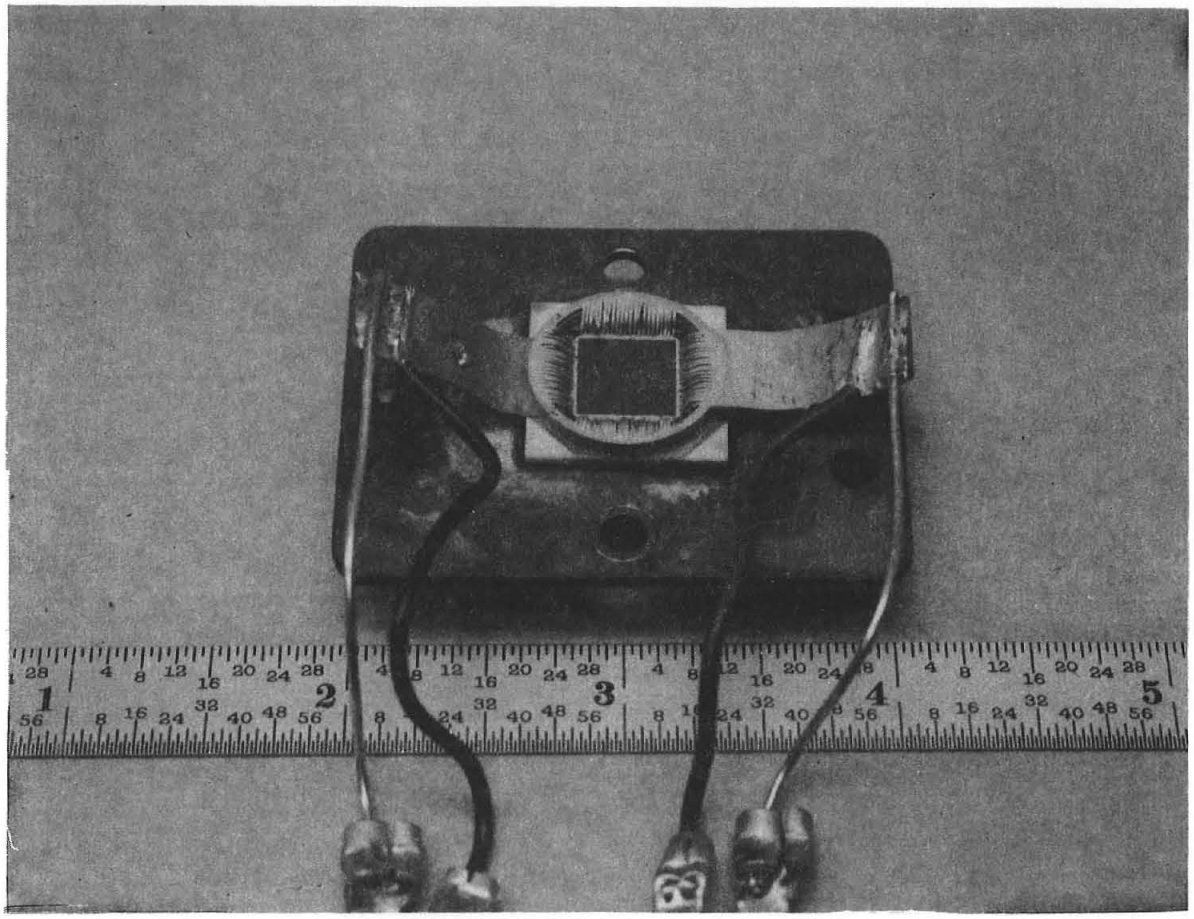

Figure 10.1 Microwave Associates' 0.37-Inch Cell

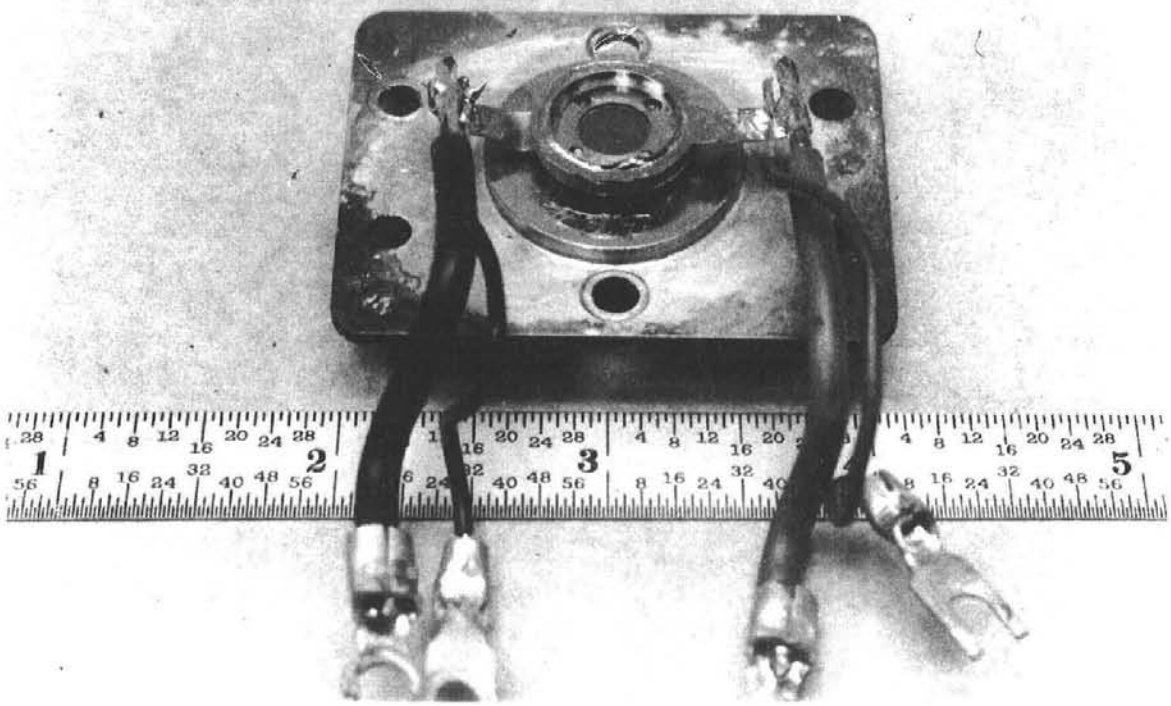

Figure 10.2 Microwave Associates'. 0.26-Inch Cell

A-6079

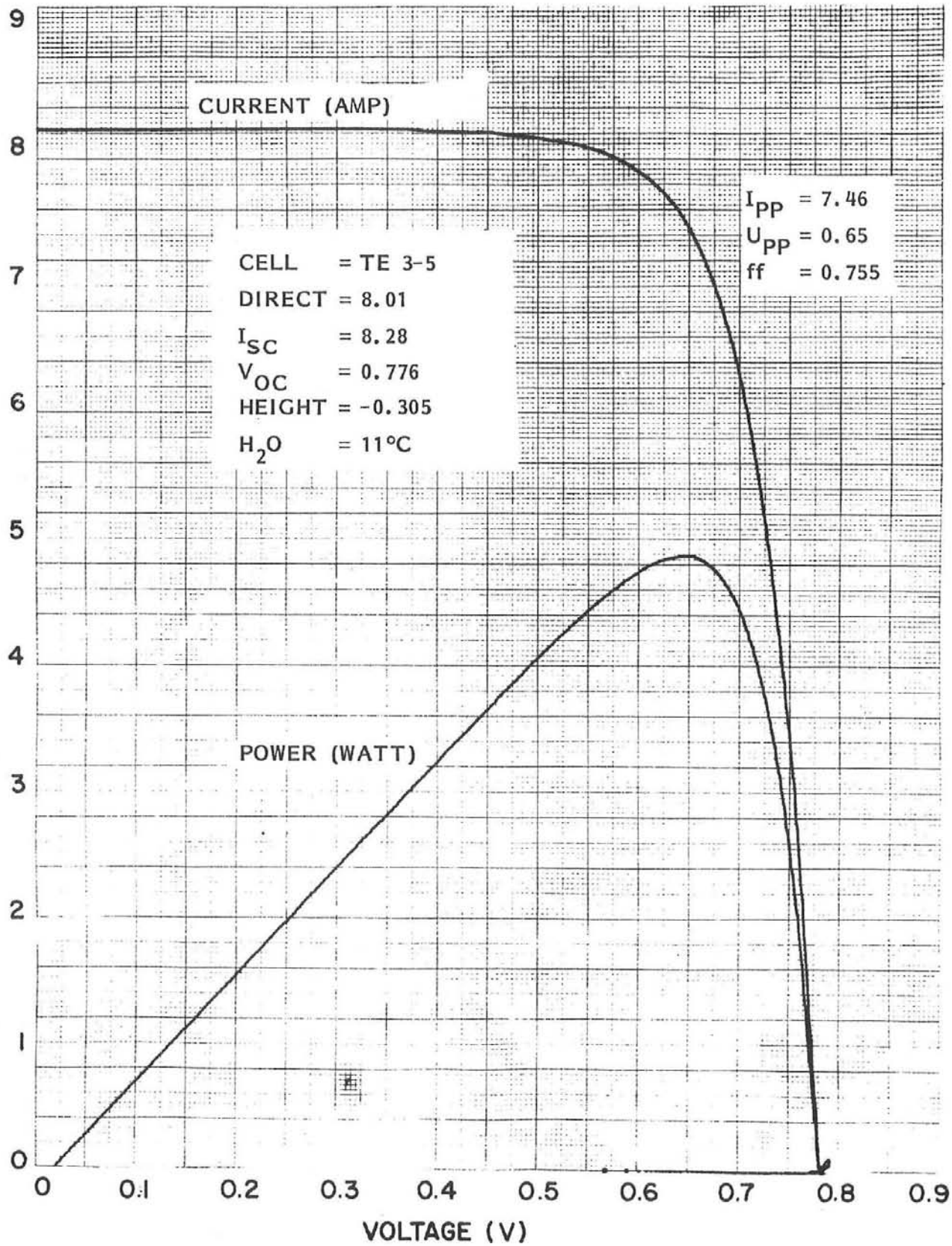

Figure 10.3 Microwave Associates 0.37-in. x 0.37-in. Cell

A-6078

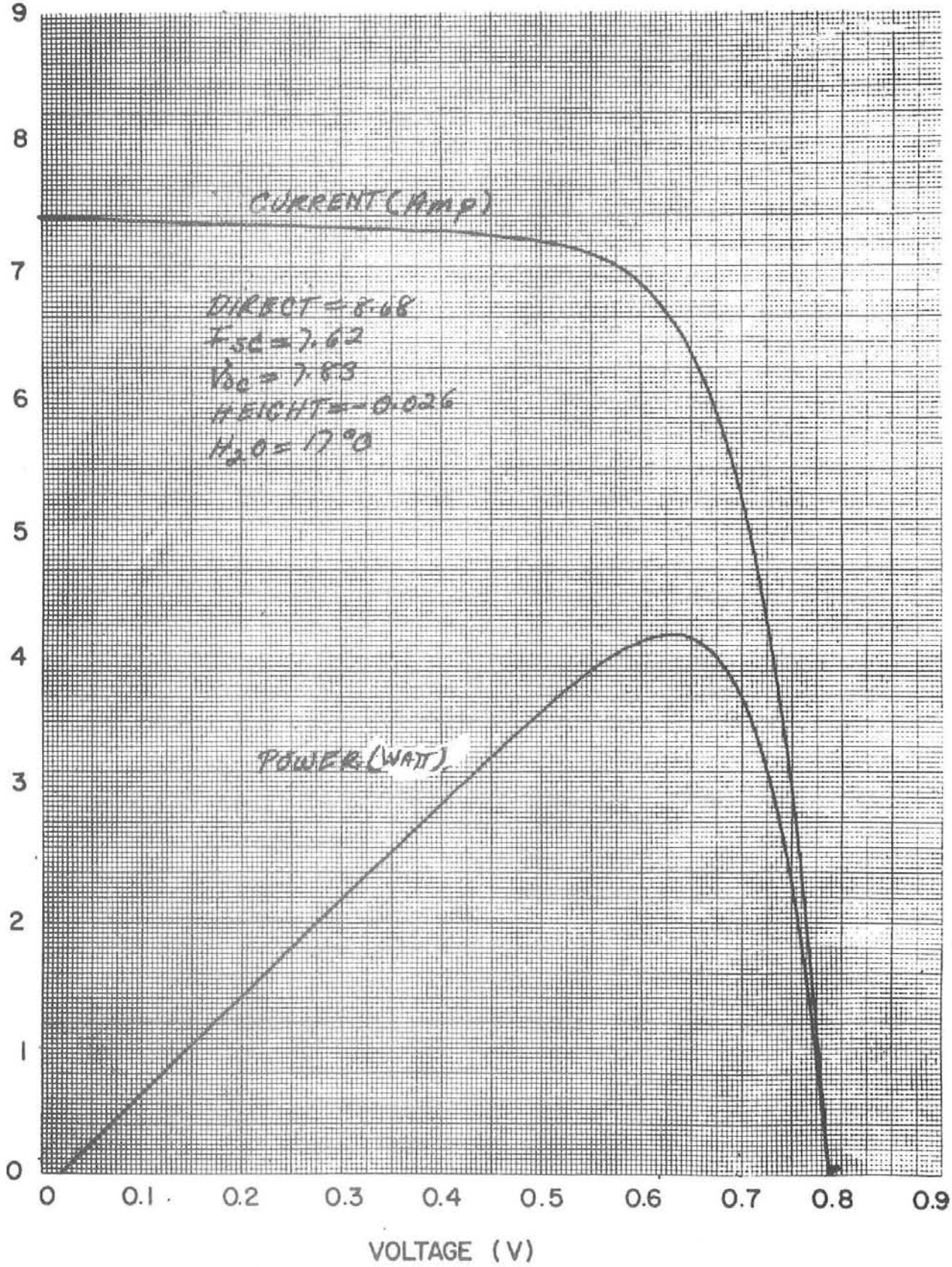

Figure 10.4 Microwave Associates 0.26-in.-Diameter Cell

Although the performance of this cell peaks between 40 and 50 suns, its efficiency decreases slowly so that it can be operated at the 90-sun level, which would be the approximate intensity with our lens. The test results for this cell are shown in Figure 10.5. A smaller ASEC cell, 1.55 cm in diameter, was also tested. This cell was designed to operate at 150 suns and we tested it at nearly 200 suns. The results for this cell are shown in Figure 10.6. The highest performance measured was obtained with this cell.

The various cells tested during the program are shown in Figure 10.7. The cells have both current and voltage leads (4-wire configuration) to minimize measurement errors. Cell configurations included the four basic types previously described and each type included cells with and without a secondary concentrator. The 0.37-in. square Microwave Associates' cells were tested with two types of secondary concentrators, and these are shown in Figure 10.8. A detail of one of the Microwave Associates' cells with a secondary is shown in Figure 10.9. The 1.55-cm diameter ASEC cell is shown with a secondary concentrator in Figure 10.10.

Lens efficiencies for various cell sizes can be estimated by taking the ratio of cell current under concentrated light to cell current at 1 sun after each has been corrected for intensity and temperature. Only an approximation is obtained since the ratio obtained may not be linear with intensity. The results for the cells tested are shown in Table 10.1.

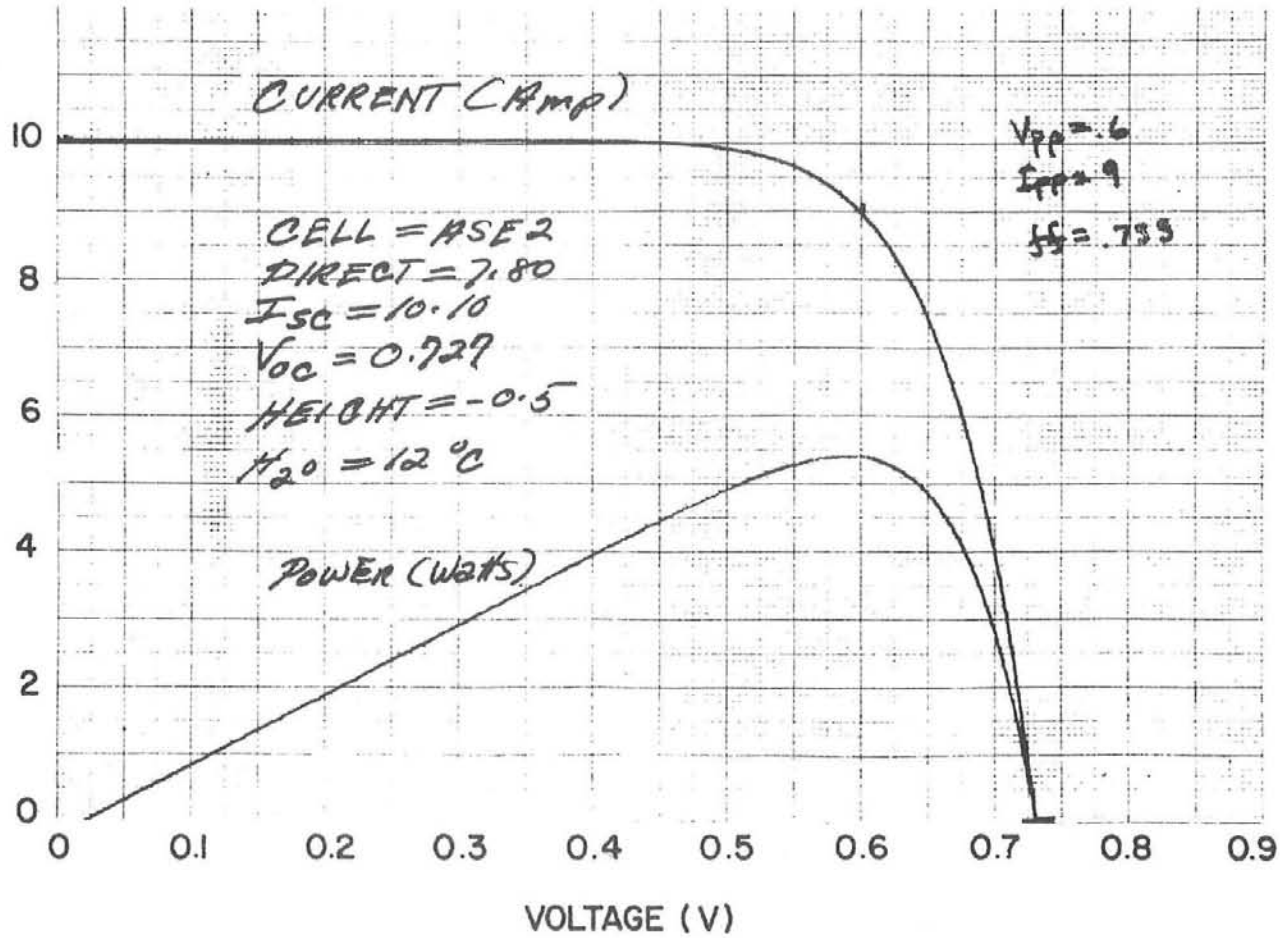

Figure 10.5 ASEC 2.05-cm x 2.05-cm Cell

A-6081

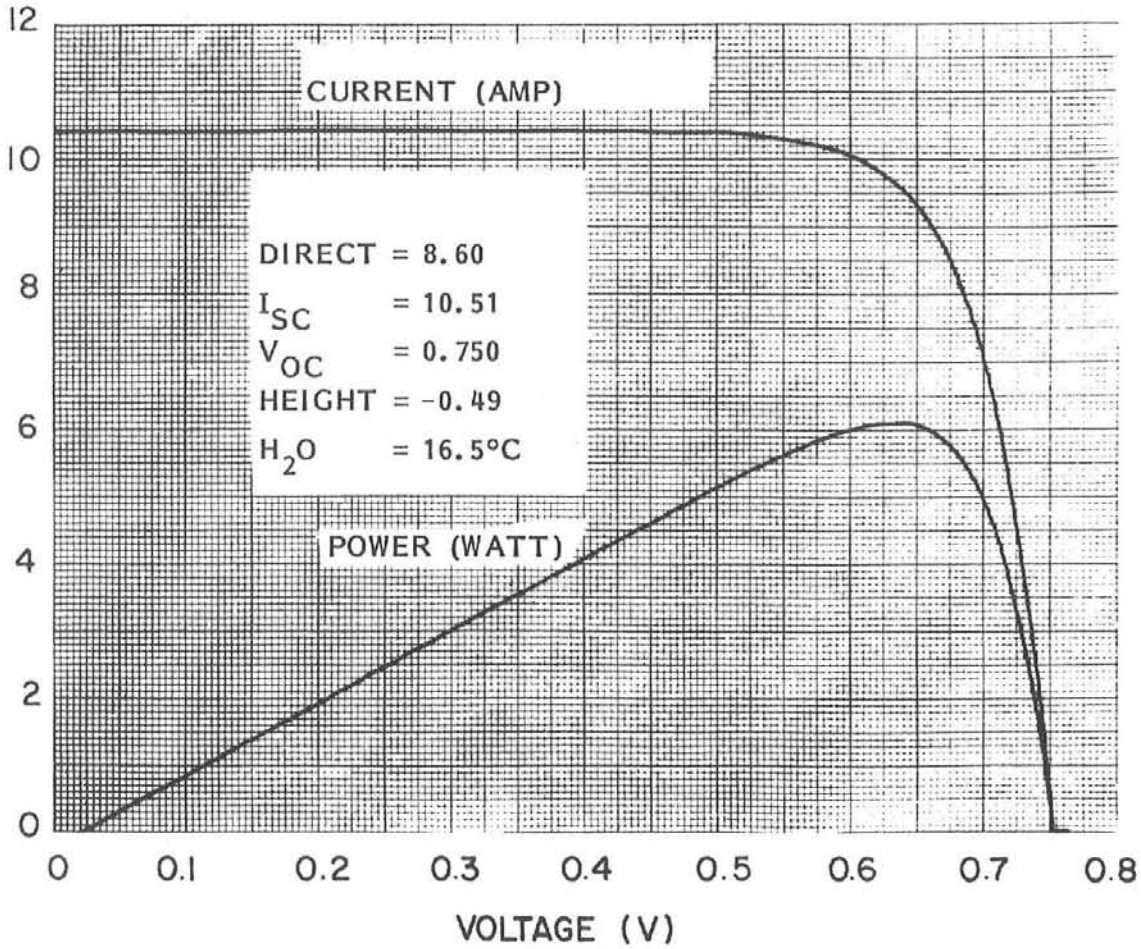

Figure 10.6 ASEC 1.55-cm-Diameter Cell

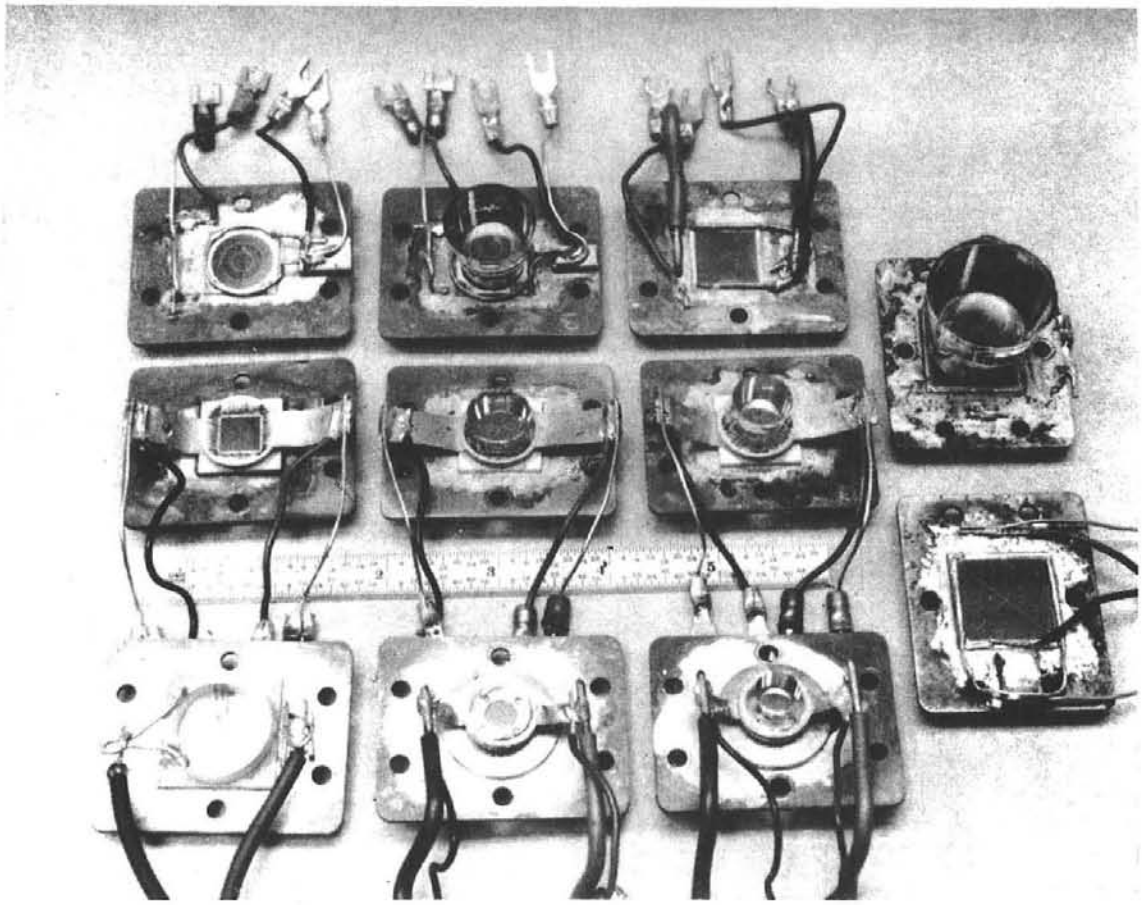

ASEC
1.55 cm

ASEC
1.55 cm
w/secondary

ASEC
1.75 cm

ASEC
2.05 cm
w/secondary

M/W
0.37 in.

M/W
0.37 in.
w/low secondary

M/W
0.37 in.
w/high secondary

ASEC
2.05 cm

M/W
0.090 in.

M/W
0.26 in.

M/W
0.26 in.
w/secondary

Figure 10.7 Various Cells Tested

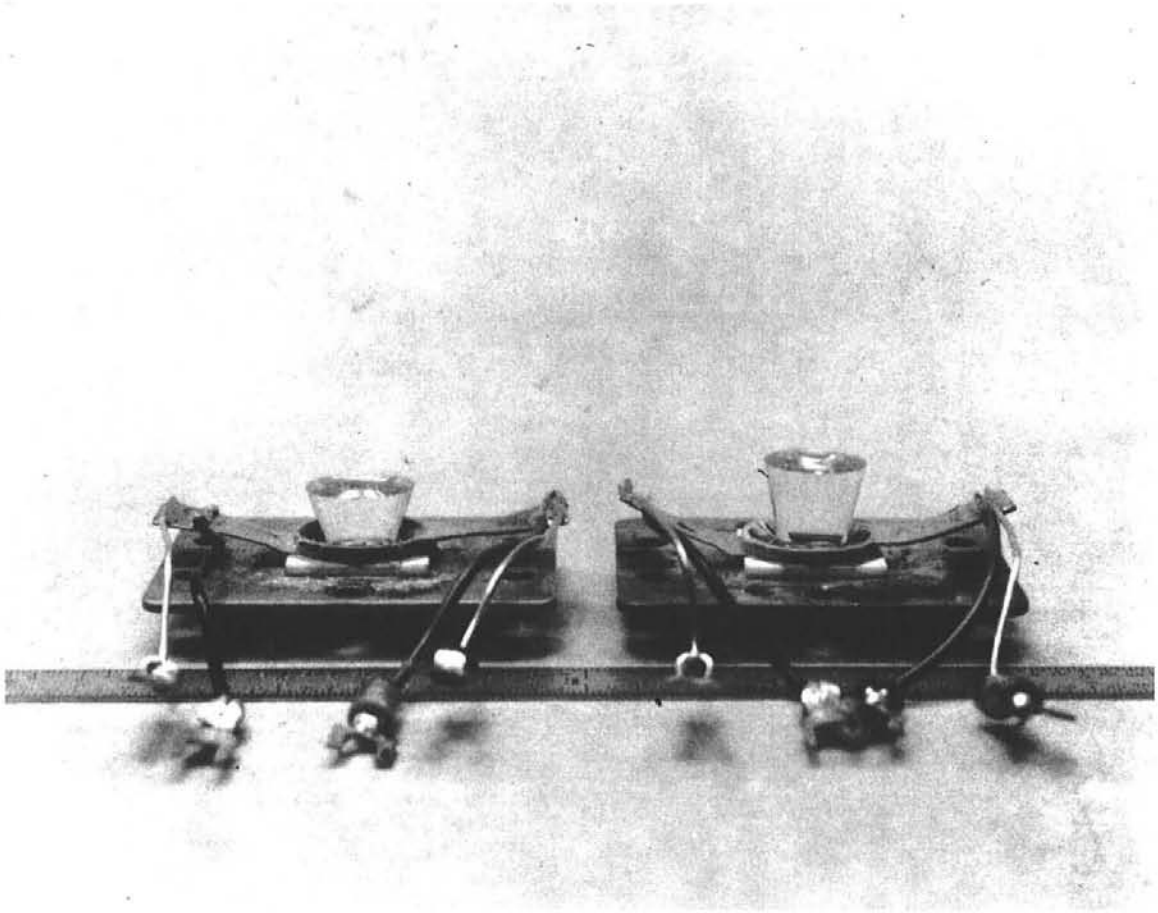

Figure 10.8 Microwave Associates' Cells with Secondary Concentrators

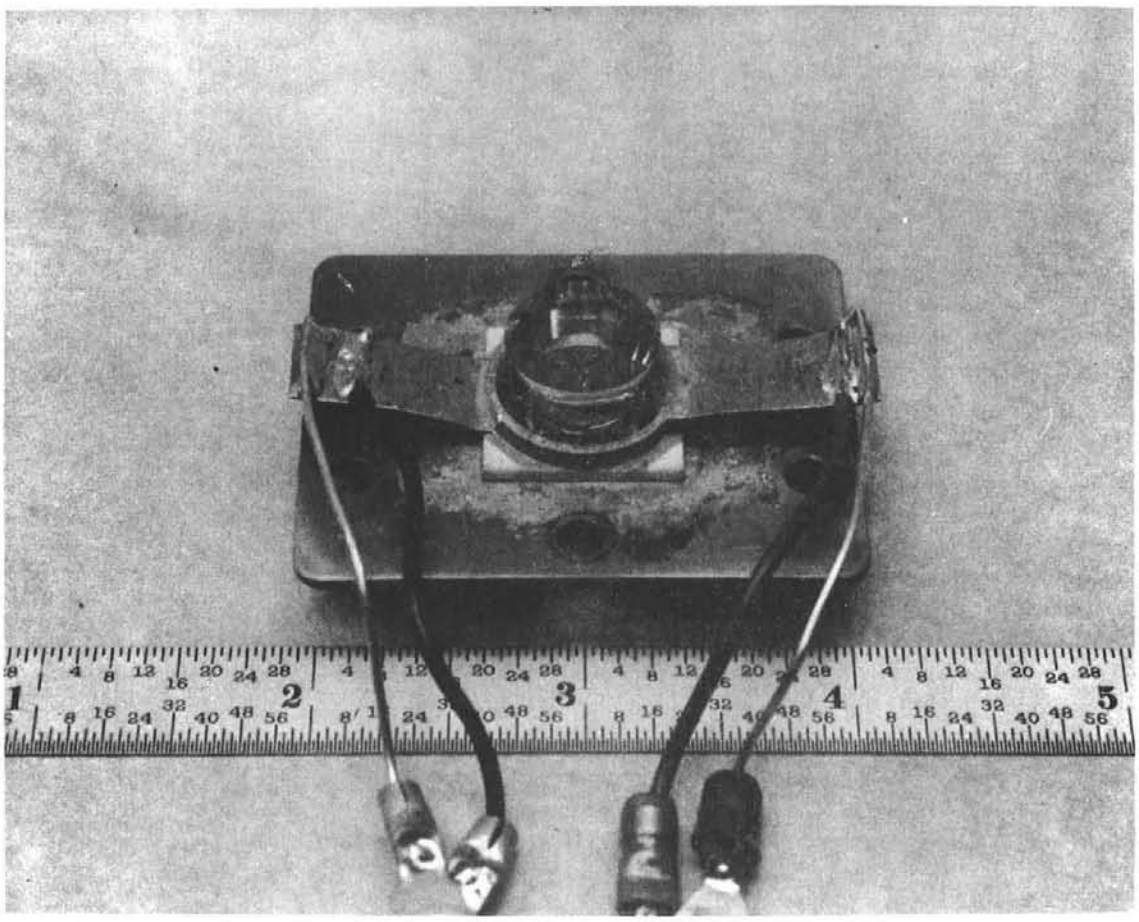

Figure 10.9 Detail of Microwave Associates' Cell with Secondary Concentrator

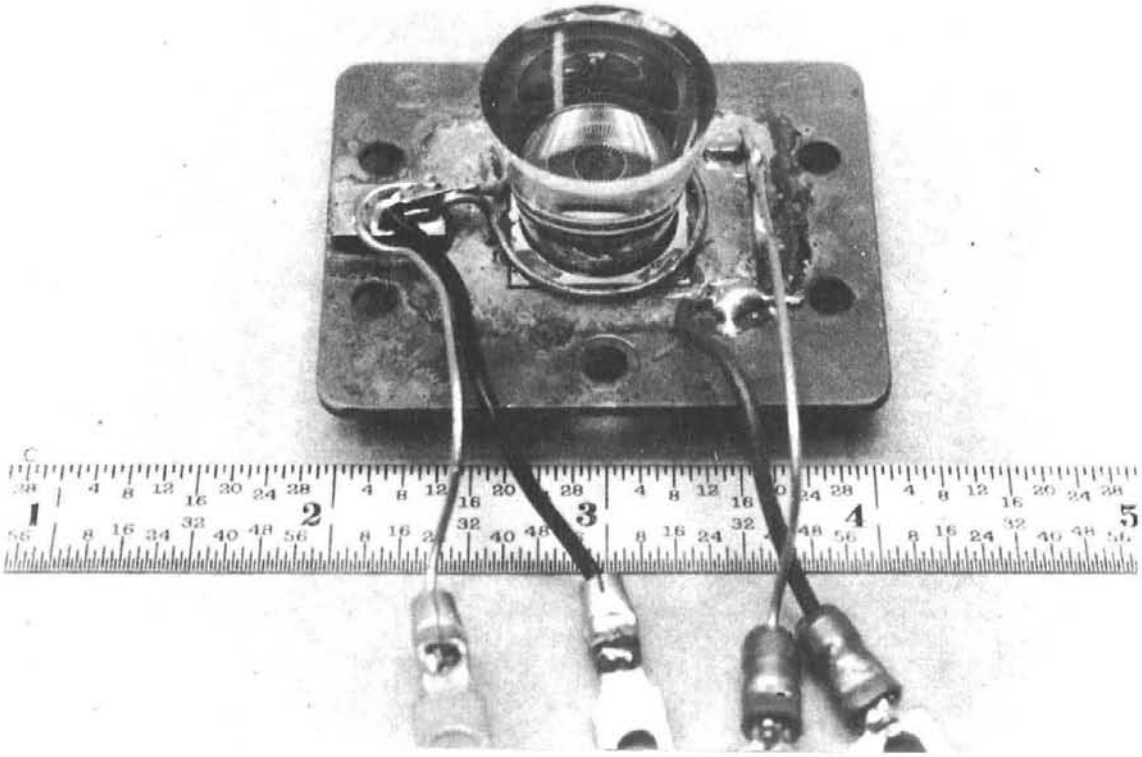

Figure 10.10 ASEC 1.55-cm Cell with Secondary Concentrator

TABLE 10.1
LENS EFFICIENCY BASED UPON CELL CURRENT RATIOS

Calibration of Direct Radiometer based upon
Eppley Radiometer - 10.7 volts/kW/m^2

Cell Type and Configuration	Lens Efficiency (%)	Geometric Concentration Ratio
Microwave Associates 0.26-in. diameter		
Without secondary	58.9	1526
With secondary	68.5	
Microwave Associates 0.37-in. square		
Without secondary	77.6	592
With secondary	82	
ASEC 1.55-cm diameter		
Without secondary	84.5 to 86.6	277
With secondary	84.8 to 87	
ASEC 2.05-cm square		
Without secondary	86.3	124
With secondary	86	

11. DESIGN RECOMMENDATIONS AND CONCLUSIONS

11.1 LENS TOOLING AND PRODUCTION

The results from the lens testing indicate that injection molding is a viable and low cost production method for manufacturing quality Fresnel lenses. Unfortunately, conventional mold tool fabrication techniques involving hard polishing do not readily lend themselves to generating a tool of the precision required. It is highly recommended that the present tooling be modified so that a diamond turned faceted surface can be substituted for the present surface which was ground and polished. It is further recommended that the lens details that permit ultrasonic welding of the lenses be removed and a new detail for adhesive bonding be applied to the mold, since adhesive bonding is more viable than ultrasonic bonding for the curved lenses.

11.2 HEAT REMOVAL

The heat removal designs generated during the program have been shown to provide adequate cell cooling. It is recommended that the flattened tube design and the round tube design be further refined because of their potential for improved performance at a lower cost. Passive cooling can provide adequate cell cooling even at high concentration ratios.

11.3 MODULE DESIGN AND FABRICATION

The present module housing design is based upon injection molding technology and is limited in size and minimum wall thickness. Alternative materials and production methods should be investigated to allow cost reduction of this part. Adhesives for the bonding of modules and lenses need to be investigated in greater detail.

11.4 SECONDARY CONCENTRATOR

Positive results, which include adequate cell/secondary bonding and decreased sensitivity to tracking and optics errors, were obtained during

the program. Further development with cells incorporating secondary concentrators should be pursued. Areas that required additional investigation include improved secondary designs and bonding materials and methods for attaching the secondary concentrator to the cell.

11.5 INSTRUMENTATION

The instrumentation developed during the program has been a great asset in the measurement and characterization of cells and lenses. Some minor modifications to this instrumentation will enhance its general use.

11.6 GENERAL

The viability of utilizing injection molded domed Fresnel lenses in combination with high concentration silicon cells has been adequately demonstrated during the program. Improved cells for use at intensities of 400 suns and greater, need to be developed.

A revised tradeoff study of cell, lens, and module sizing needs to be conducted with the constraints of array size and cost.

11.7 CONCLUSIONS

The results obtained during the program indicate that injection-molded, domed, acrylic lenses should be capable of obtaining efficiencies in the 87 to 89 percent range when used in conjunction with cells operated at a geometric concentration ratio of 600. The cells should have efficiencies in the range of 19 to 20 percent giving an overall module efficiency between 16.5 and 17.8 percent. To achieve these results, the mold tooling must be corrected utilizing diamond turning techniques to provide accurate surface contours. Cell cooling, either by active or passive techniques, can control the cell temperature and restrict the temperature rise to 10° to 15°C above the coolant or ambient temperature. The module case can be injection molded, although a mold for a single piece molding is expensive. The module case can be molded in four identical quadrants, and the cost of the mold for a molding this size is more reasonable.

APPENDIX 1

MICROWAVE ASSOCIATES FINAL REPORT

FINAL TECHNICAL REPORT

ENGINEERING SOLAR CELL SUPPORT FOR THE SANDIA HIGH CONCENTRATION MODULE DEVELOPMENT PROGRAM

PREPARED FOR

THERMO-ELECTRON CORPORATION
R&D/New Business Division
101 First Street
Waltham, Mass. 02154

PREPARED BY

Robert Frank
J. D. Chapple-Sokol

9 JUNE 1981

MICROWAVE ASSOCIATES, INC.
SOUTH AVENUE
BURLINGTON, MASSACHUSETTS 01803

TABLE OF CONTENTS

		PAGE #
1.0	INTRODUCTION	1
2.0	BRIEF REVIEW OF THE STRUCTURE AND OPERATION OF THE ETCHED MULTIPLE VERTICAL JUNCTION (EMVJ) CELL	3
	2.1 The Effect of Series Resistance on Cell Performance	3
	2.2 Baseline EMVJ Structure	3
3.0	DESIGN CONSIDERATIONS FOR THE T/E CELL	9
	3.1 Size and Intensity	9
	3.2 Description of the Cell Structure Designed for T/E	10
4.0	EXPERIMENTAL RESULTS	12
	4.1 Fabrication and Testing of Quadrant Cells	12
	4.2 Discussion	16
	4.3 Experiments with Secondary Concentrator	20
5.0	CONCLUSIONS	23

LIST OF ILLUSTRATIONS

		PAGE #
FIGURE 1	THE EFFECT OF SERIES RESISTANCE (R_S) ON EFFICIENCY FOR INCREASING INTENSITY (STRAIGHT LINE FOR $R_S = 0$ IS AN IDEALIZATION	4
FIGURE 2	BASIC STRUCTURAL FEATURES OF THE FRONT-GROOVED ETCHED MULTIPLE VERTICAL JUNCTION (EMVJ) CELL	5
FIGURE 3	TOP SURFACE LAYOUT AND SIZE OF BASELINE CELL	7
FIGURE 4	PERFORMANCE OF FRONT GROOVED EMVJ CELL	8
FIGURE 5	IMPROVED GRID DESIGN UTILIZES BOTH SETS OF ⟨111⟩ PLANES FOR LESS OBSCURED AREA OR LARGER CELL (AREA OF CELL SHOWN = 0.88 cm^2)	11
FIGURE 6	PERFORMANCE OF T/E QUADRANT CELL AS SHOWN IN FIGURE 5	13
FIGURE 7	PHOTOGRAPH OF THE QUADRANT CELL IN ITS MOUNT	14
FIGURE 8	PHOTOGRAPH OF BASELINE CELL IN PACKAGE WITH TOP CONTACT	15
FIGURE 9	MODIFIED QUADRANT GRID GEOMETRY	18
FIGURE 10	TEST OF BASELINE CELL WITH AND WITHOUT A SECONDARY STAGE CONCENTRATOR	22

1.0 INTRODUCTION

This report covers work performed by Microwave Associates (M/A) for Thermo-Electron (T/E) during the period December 1979 through May 1981. The major goal of this work was to provide T/E with EMVJ photovoltaic cells, especially designed to operate with the domed Fresnel lens optics module being fabricated by T/E for Sandia Laboratories. The work consisted of essentially three phases:

1. An engineering support phase during which information was provided to T/E on the operating characteristics of EMVJ cells under various conditions. In addition certain measurements and experiments were carried out by M/A at T/E's request, and various samples were provided to T/E for evaluation and measurement. At the end of this phase a particular cell size and operating concentration were mutually agreed upon.

2. A design phase then took place at M/A, resulting in a specific cell design intended to have a low series resistance with a cell of much larger area than had yet been fabricated at M/A. In addition, a metallized beryllia mount with brazed copper tabs for top and bottom electrodes was designed and approved by T/E. Materials and masks for both cell and mount were ordered and received by June 1980.

3. The final phase, fabrication and testing, resulted in cells which had excellent performance in the 1 to 100 sun range, but the efficiency began decreasing rapidly above 100-200 suns. A design change was made in the grid pattern in order to correct the problem, with only partial success. At this time the nature of the problem is not fully understood. In the meantime, the smaller "baseline" cell being fabricated for Sandia was tested with a secondary stage concentrator, and this combination appears to work well, so emphasis is being placed on this approach at present. Approximately 25 cells on specially designed mounts were delivered to T/E during this period, of both the quadrant and the baseline design.

2.0 BRIEF REVIEW OF THE STRUCTURE AND OPERATION OF THE ETCHED MULTIPLE VERTICAL JUNCTION (EMVJ) CELL

2.1 The Effect of Series Resistance on Cell Performance

The single most important factor which limits cell performance at high incident intensities is series resistance (R_s). The series resistance due to the cell (and its leads) must be very small, so that the total voltage drop due to R_s is less than ~20 mV at the operating point. This means that at 500 suns, a cell with an area of 1.0 cm^2 must have an R_s of less than a few milliohms in order that the effect on efficiency be negligible. There are four major sources of series resistance in horizontal junction solar cells: the metallization grid, the thin surface diffusion, non-ohmic contacts, and carrier depletion in the base region. Since it is virtually impossible to reduce R_s to a sufficiently low value in a horizontal junction cell, the efficiency of these cells, even when modified for improved high intensity performance, begins to decrease around 50-100 suns. Furthermore, since the effect of the internal voltage drop on efficiency is highly nonlinear, efficiency decreases very rapidly with further increases in intensity. The effect is illustrated in Figure 1.

2.2 Baseline EMVJ Structure

By making a radical alteration in cell configuration, a sufficiently low R_s to allow efficient cell operation at ~1000 suns has been achieved. The basic structure is shown in Figure 2. The starting material is silicon with a ⟨110⟩ surface orientation to permit the anisotropic etching of a series of narrow vertical-walled grooves normal to the surface. The groove walls contain a p+ diffused region which acts as the emitter, and the back of the wafer has a continuous n+ diffusion. The groove walls are heavily plated with gold, which conducts the collected carriers to a bus which surrounds the active area. The basic structure virtually eliminates

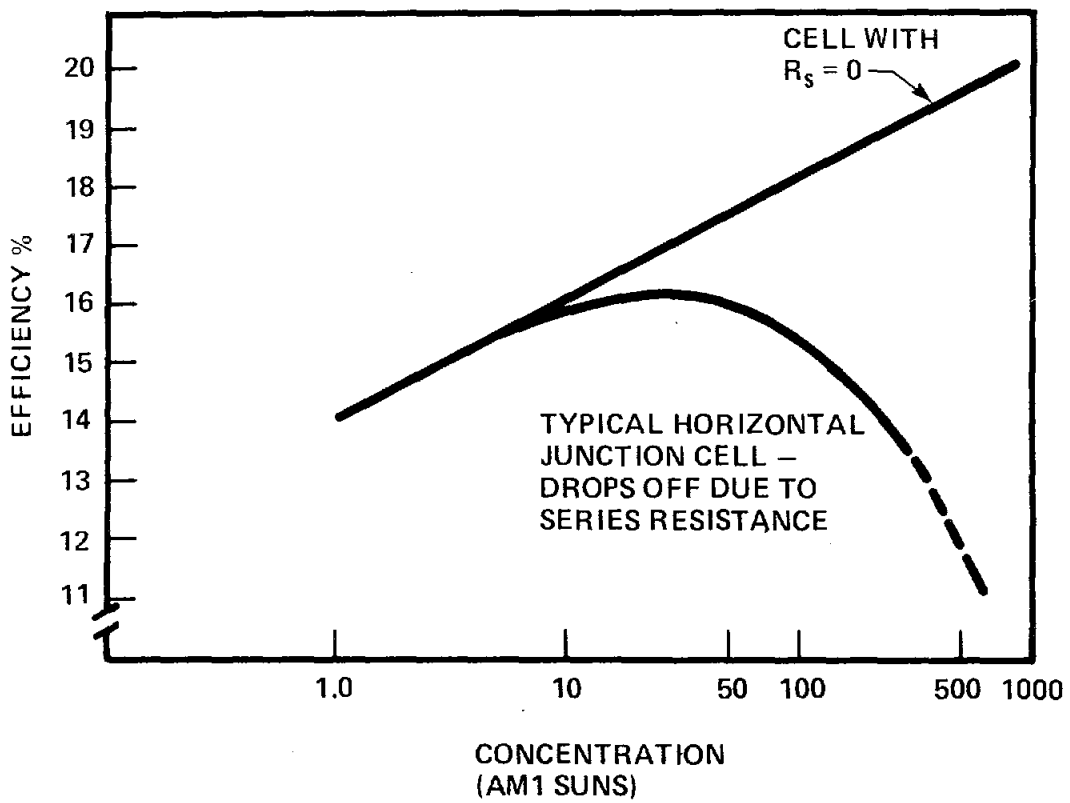

FIGURE 1 THE EFFECT OF SERIES RESISTANCE (R_S) ON EFFICIENCY FOR INCREASING INTENSITY.

D-18537B

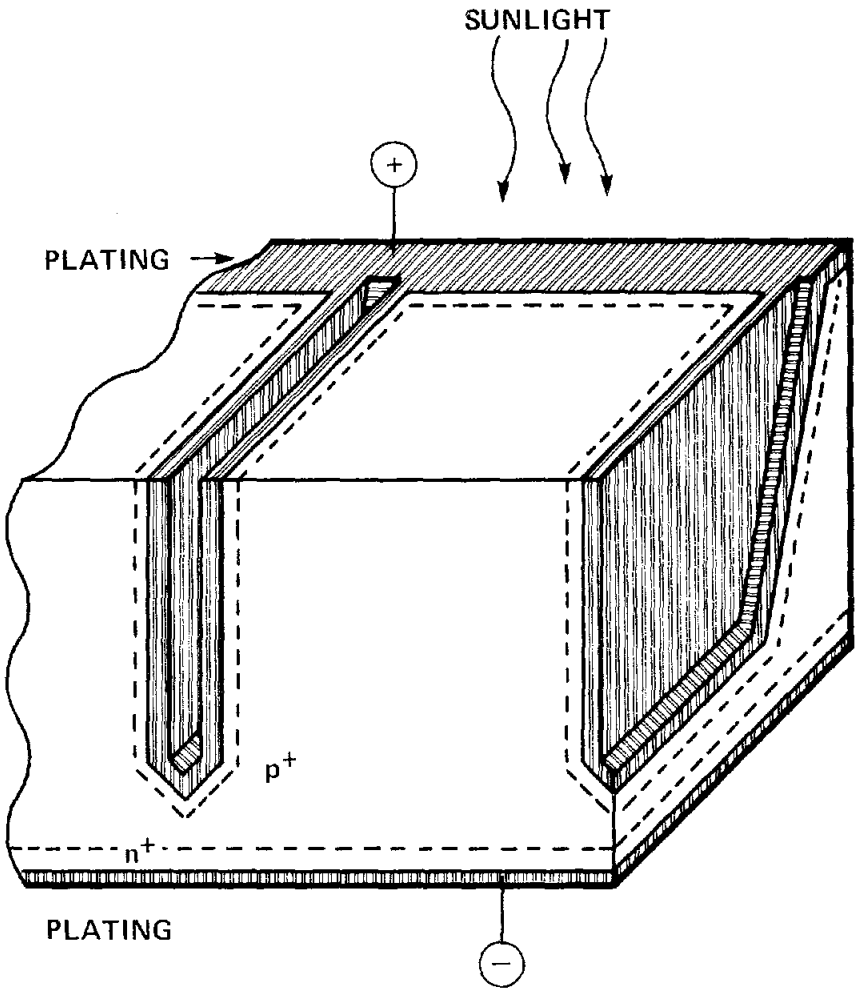

FIGURE 2 THE EMVJ CELL (ETCHED MULTIPLE VERTICAL JUNCTION)

D-19106

the internal voltage drops which arise in horizontal junction cells at high concentration from current flow in the thin surface diffusions, from the grid metallization, and from contact resistance. In this device, current flows directly through the p+ junction diffusions into the metallization on the groove walls, so there is no current flow in the plane of the diffused layer. In addition, since the plated area is large relative to the groove width (a ratio of 15:1), series resistance losses in the metallization itself are negligible. Contact resistance is reduced because the entire junction area is metallized. The grooves are 12-15 μm wide and have a 200 μm center spacing.

During plating (thin Ni for adhesion, thick gold for conductance) the grooves are nearly filled with metal, and some top surface area on either side is also covered. The total obscured surface area is ~ 10%. The metallization grid is thus equivalent to a series of lines ~ 12 μm (0.5 mil) wide by 100 μm (4.0 mils) thick, to give an effective resistance of ~ 2 mΩ. The top electrode bus, which connects all of the grooves electrically in parallel, defines an active area 0.66 cm in diameter (0.34 cm^2 in area) and has an outer dimension of 0.76 cm square, as shown in Figure 3. The performance parameters for this cell are shown in Figure 4. The efficiency reaches ~ 18.5% at 500 suns and the decrease beyond 1000 suns is due to voltage drops in the base. The cell uses thermally grown SiO_2 at present as the AR coating, until an improved coating, such as Si_3N_4, is available. The one sun short circuit current is 31.5 mA/cm^2.

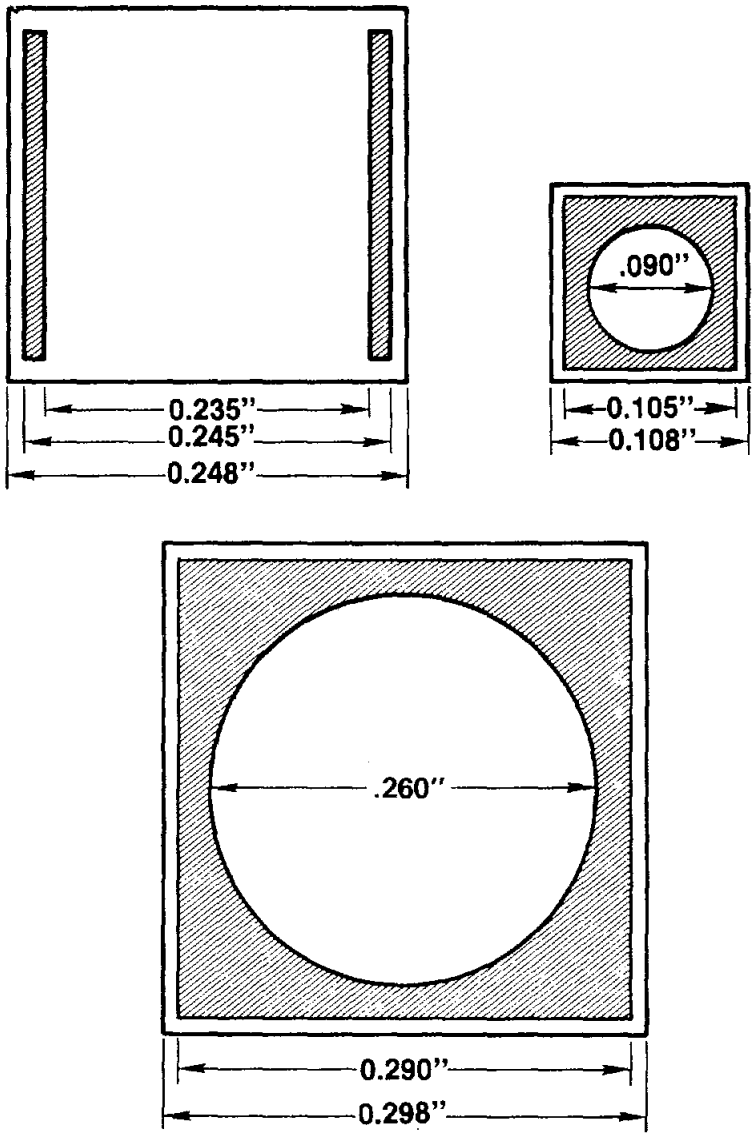

FIGURE 3 TOP SURFACE LAYOUT AND SIZE OF TEST CELLS

D-19593

PERFORMANCE OF FRONT-GROOVED EMVJ CELL (0.260″ DIA)

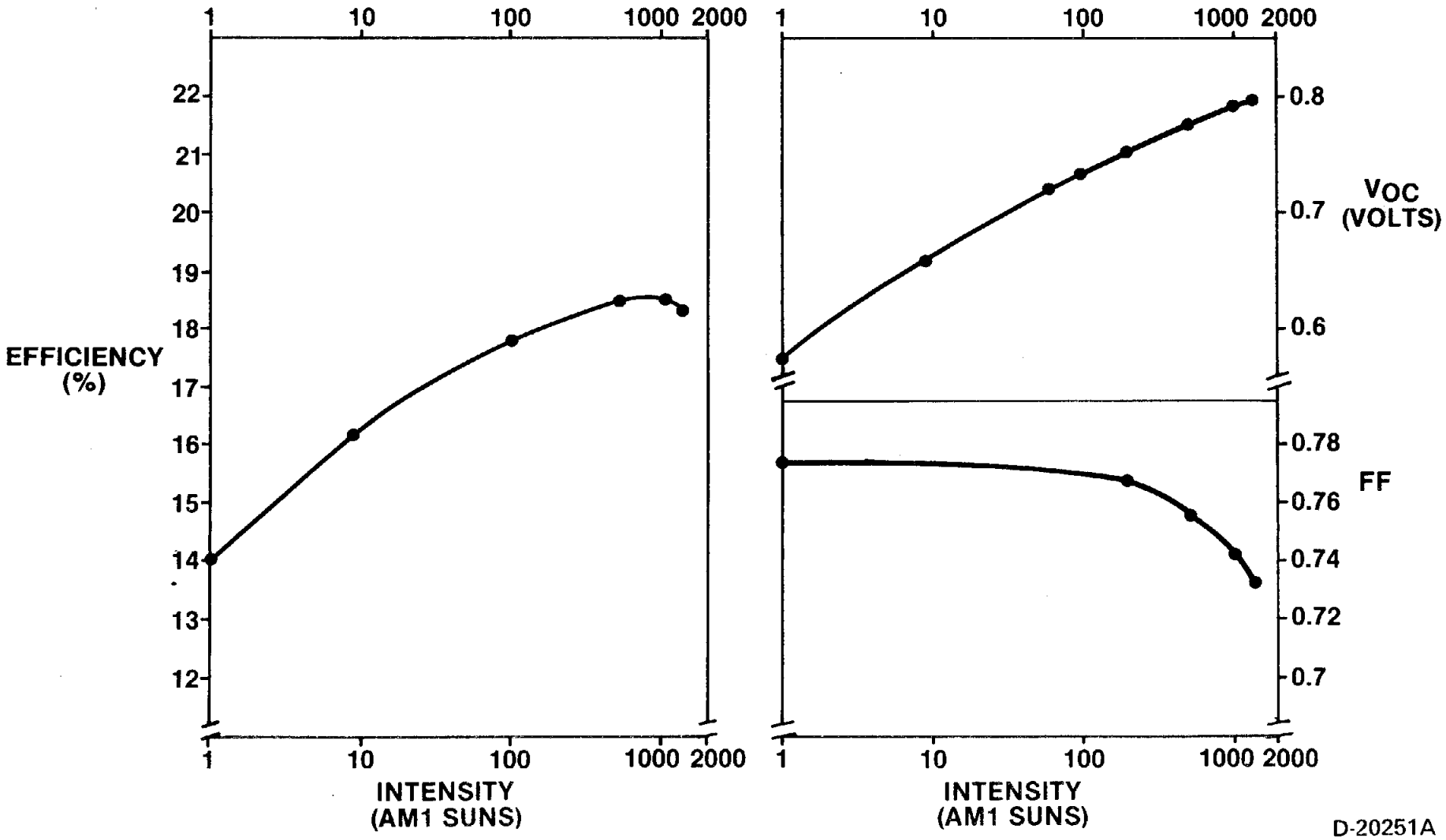

FIGURE 4

3.0 DESIGN CONSIDERATIONS FOR THE T/E CELL

3.1 Size and Intensity

T/E requested a cell with an active area 0.94 cm x 0.94 cm (0.37" x 0.37") or 0.88 cm^2 in area. The spot of focussed light impinging on the cell was designed to cover $\sim \frac{1}{4}$ of the cell area and have an average concentration within the spot of 2000 suns. Assuming no effects due to this highly non-uniform illumination, this is equivalent to a uniform cell illumination of 500 suns. In designing the T/E cell, it was taken as a ground rule that the internal voltage drop in the metallization should be no greater than that in the baseline cell. It was evident that the baseline cell could not simply be scaled up, because the much larger area of the T/E cell would require excessively wide grooves in order to carry the much greater current. This would result in an obscured surface area approaching 30%, which would be totally unacceptable.

The relative groove width required for a given internal voltage drop may be determined as follows. For a uniformly illuminated cell having a conductor grid consisting of straight grooves of equal length, the internal voltage drop due to current flow in the grooves, ΔV, is proportional to SL^2/D, where S is the groove center spacing, L is the groove length, and D is the groove depth. In order to compare similar geometries, an earlier square version of the baseline cell, having a groove length of 0.235" was used for the calculation.

This cell had the same groove width (12.5 μm), depth (100 μm), and center spacing (200 μm) as the present baseline cell, and a peak efficiency at $\sim$ 500 suns, making it especially appropriate for establishing the T/E cell dimensions. Using the above formula, $\Delta V = SL^2/D$, the increase in ΔV due to the increased groove length is $(0.37)^2/(0.235)^2 =$ 2.5. Thus, the groove width would require an increase from 12.5 μm (0.5 mil)

to 31 μm (1.2 mil). In addition the spread of the plating on the surface is about 0.5 times the groove width, to give an obscured area of 46.5 μm (1.8 mil) for the larger cell. Finally, since the illuminated area is much smaller than the cell, ΔV will be much larger than given by the above formula based on uniform illumination, since fewer grooves will be carrying more current for spot positions near the center of the cell. This effect could easily increase ΔV by another factor of two, since for a centered spot, only $\frac{1}{2}$ of the grooves would be carrying the same total current. The result of these considerations is that an increase in groove width by a factor of ~ 5 would be required to maintain the desired internal voltage drop. By increasing the groove depth somewhat, the required increase in groove width would be reduced, but an unacceptably large obscured area of $\sim 30\%$ would still be necessary.

3.2 Description of the Cell Structure Designed for T/E

In a single crystal silicon wafer having a ⟨110⟩ surface orientation, there are two sets of ⟨111⟩ planes which are normal to the surface. These sets of planes intersect each other at an angle of $\sim 70^{\circ}$. In a typical EMVJ cell, the grooves are etched along only one set of these planes to give the desired set of straight vertical-walled grooves. If both sets of planes are utilized, a quadrant type of pattern can be obtained, which reduces ΔV by almost a factor of 4 with uniform illumination (for a given groove width). The use of such a pattern, therefore, allows the use of the same groove width as in the baseline cell with only a small increase in ΔV. The layout chosen for the T/E cell is shown in Figure 5. The space between grooves along the diagonals is exaggerated - the grooves must not actually meet because rapidly etching corners are then exposed. The actual space is on the order of the center spacing of adjacent grooves.

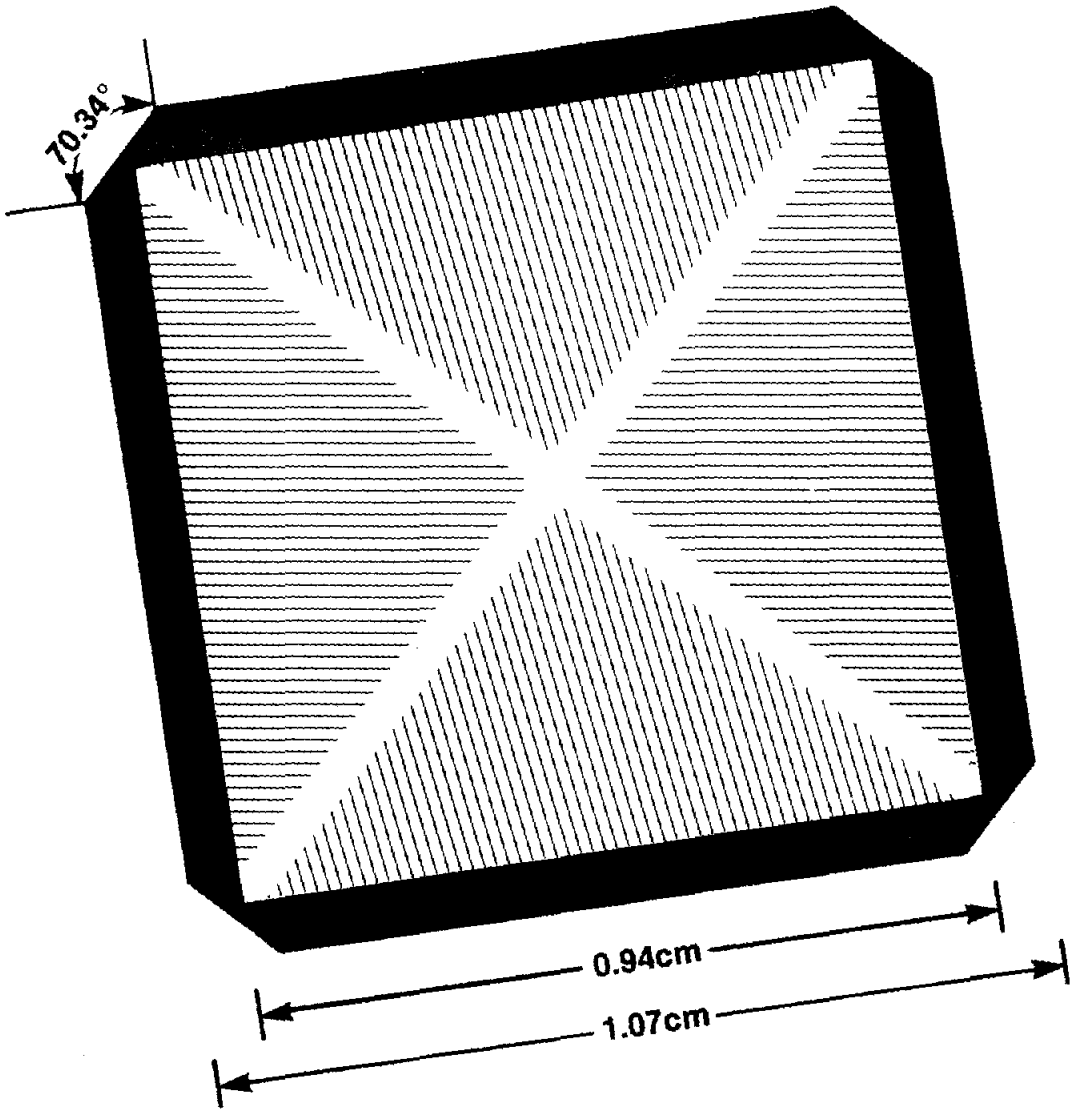

FIGURE 5

D-20250

4.0 EXPERIMENTAL RESULTS

4.1 Fabrication and Testing of Quadrant Cells

The first run of T/E cells was fabricated during August 1980. For comparison, a run of standard baseline cells and a run of baseline cells with a quadrant pattern were carried out at the same time. No difficulties were encountered during fabrication with the groove etching step, or any of the other steps. Cells of each type were mounted for high-intensity testing. The one sun V_{oc} and FF performance of all three types was very good. The T/E cell had the best one sun values of V_{oc} and FF ever measured on an EMVJ cell, with $V_{oc} = 0.6$ volts and FF = 0.79. One sun values for J_{sc} were not measured for these initial runs, due to poor weather conditions.

The high intensity measurements will now be described. The baseline cell behaved in a typical fashion such as that shown earlier in Figure 4. The T/E cell could only be tested to $\sim$ 700 suns because of its large size. The results are shown in Figure 6, where it is seen that the FF decreases very rapidly with increasing intensity, starting at about 100-200 suns, and V_{oc} is also somewhat low at high intensities. The decrease in FF was not due to R_s in the metallization; this was determined by over-plating a cell and finding no change in FF behavior. It was also found that the run of baseline cells having a quadrant pattern behaved much like the T/E cell, with a relatively rapid decrease in FF at high intensities, while the standard straight-grooved baseline cells had good high intensity performance, as shown previously in Figure 4.

A close-up photo of a mounted cell is shown in Figure 7. The top electrode of the cell is attached to the external leads with enough ribbon bonds to avoid voltage drops at high intensity. A close-up of a packaged baseline cell is shown in Figure 8, with a top contacting scheme similar to one that could be used with the T/E cell.

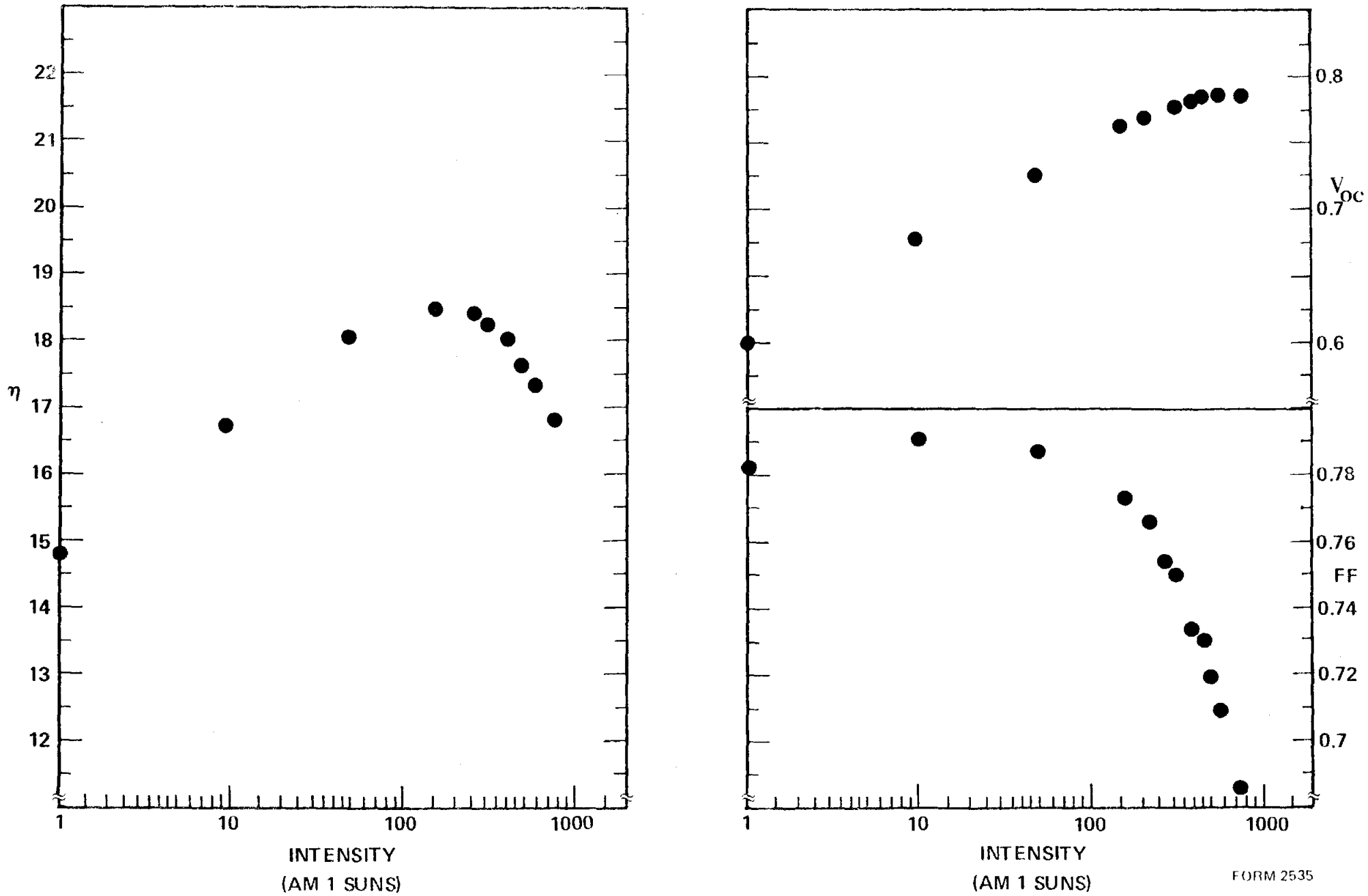
η
22
21
20
19
18
17
16
15
14
13
12
1
10
100
1000
INTENSITY
(AM 1 SUNS)
V_{oc}
0.8
0.7
0.6
FF
0.78
0.76
0.74
0.72
0.7
1
10
100
1000
INTENSITY
(AM 1 SUNS)
FORM 2535

FIGURE 6

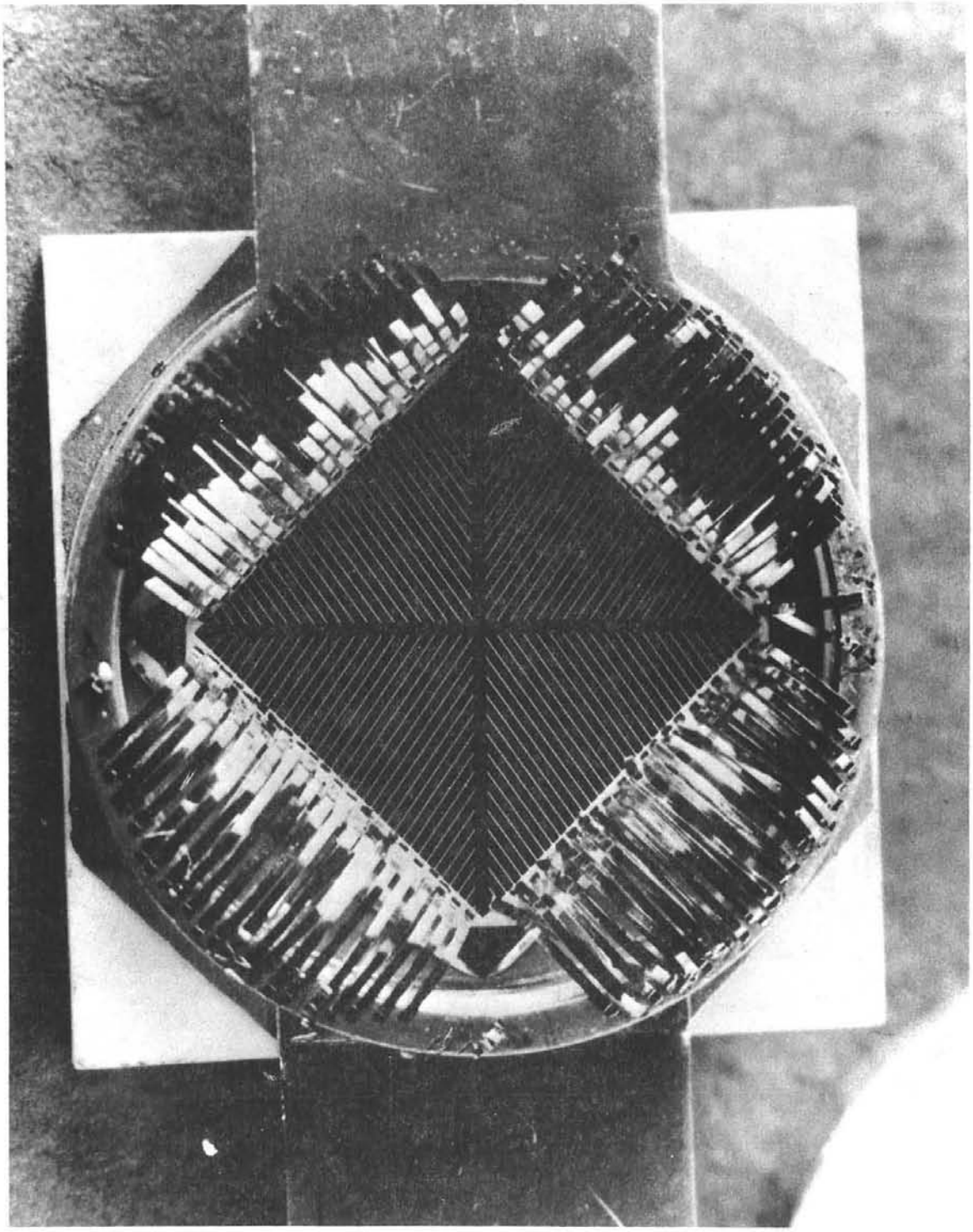

Figure 7. Photograph of the T/E Quadrant Cell in Its Special Mount Using a Metallized Beryllia Base. Multiple Ribbon Bonds are Used to Connect the Top Cell Electrode to the Top Copper Tab With a Negligible Voltage Drop.

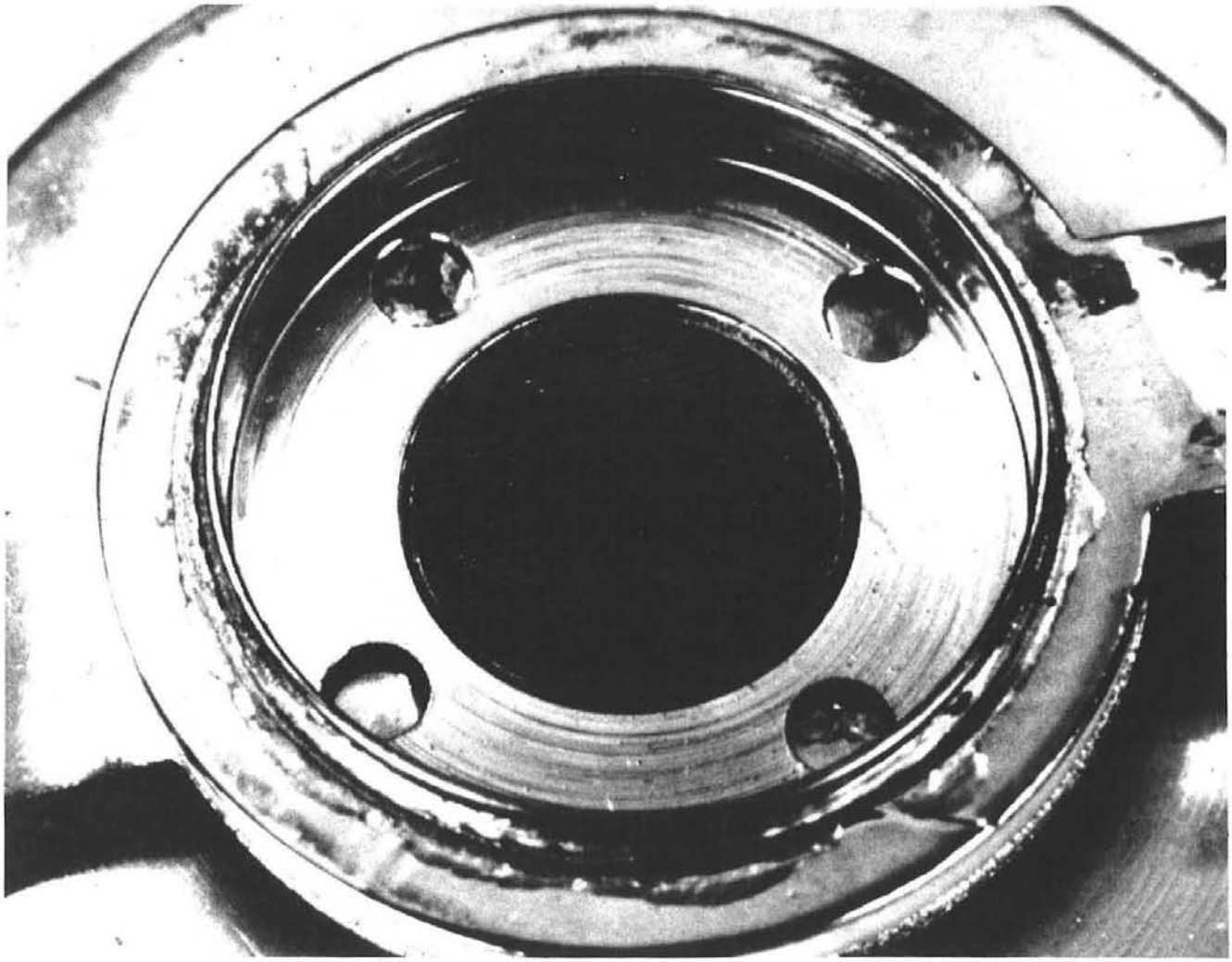

Figure 8.

4.2 Discussion

From these results it can be concluded that the problem lies with neither the processing nor the large size of the T/E cell, but with the design of the quadrant pattern. This conclusion is based on the fact that baseline cells had good performance, and modified baseline cells with a quadrant pattern, from the same run, had poor performance similar to that of the T/E cells.

Since there is no fundamental difference, either structurally or electronically, between the two sets of (111) planes, attention was focussed on the specific dimensions chosen for the design of the T/E grid pattern. In particular, the spacing between sets of grooves in each quadrant, i.e. along the cell diagonals, was a potential source of voltage drops in the base region. This is because the ends of the grooves are not vertical, like the groove walls, but slope away from the top surface at an angle of 35°, so carriers collected deeper in the base have a greater distance to travel with increasing depth into the base. In the cell design shown in Figure 7, the distance between p+ junctions at the cell diagonals is 12 mil at the surface, but is 18.6 mil at the bottom of the grooves for the 70.34° angle quadrants and 21.3 mil at the bottom of the 109.66° quadrants. Therefore, the effective base width for the quadrant cells is much greater in this diagonal region (which represents 9% of the cell active area) than anywhere in the baseline configuration. This large effective base width is probably not too long compared to the carrier diffusion length in the base region. Sandia Laboratories measured the carrier lifetime of baseline cells to be on the order of 400 μsec, which corresponds to a diffusion length of 30 mil. The problem lies, however, with the loss of conductivity modulation at high carrier injection levels*. When current flows through a cell at very high light intensities a depletion of minority carriers occurs starting at the back surface (where minority carriers cannot be generated). This creates a non-uniform electric field in the cell's base region, and consequently a voltage drop across the area of the cell depleted in holes. The base region conductivity is thus no longer proportional to incident light intensity, but becomes limited by the conductivity of the material. Hence, cell fill factor,

*See Schwartz, et al., IEEE Trans. Elec. Dev. ED-28, 264 (1981).

and consequently efficiency drop at lower light intensity than expected. This loss of conductivity modulation at high intensity manifests itself as a current dependent series resistance, and looks like a shunt resistance on an I-V curve.

There are two approaches to overcoming this limit to high efficiency at high intensity. One can make cells out of lower base resistivity material so that the limiting resistance of the base region is as small as possible. Also, the effective base region can be decreased, which reduces the extent of the effect. In horizontal junction cells, this would mean thinning the base region so p+ and n+ junctions are closer together. In a vertical junction cell this can be accomplished by moving the grooves closer together. This was attempted with the modified geometry shown in Figure 9. At the cell surface the grooves are only 2 mils apart on the diagonal, and at the bottom of the grooves the distance is less than 10 mils (the groove center spacing).

Unfortunately, cells with this modified groove pattern showed essentially the same behavior as the original cells. Either this modification was not entirely effective in narrowing the base region or the problem lies elsewhere. The following approaches could be used to reduce the base width:

1. Make thinner (e.g. 8 or 6 mil) cells.
2. Etch deeper grooves.
3. Etch n+ grooves up from the back of the cell.
4. Use lower resistivity material.

More time is required to investigate these possibilities.

Although the overplating experiments suggest the contrary, it is possible that the small voltage drops along the grooves affect the fill factor adversely. As the grooves are connected only at the bus and their lengths vary considerably, there could be significant potential differences at the ends of the grooves. This could be investigated by metallizing stripes along the cell diagonals that would tie all the grooves together.

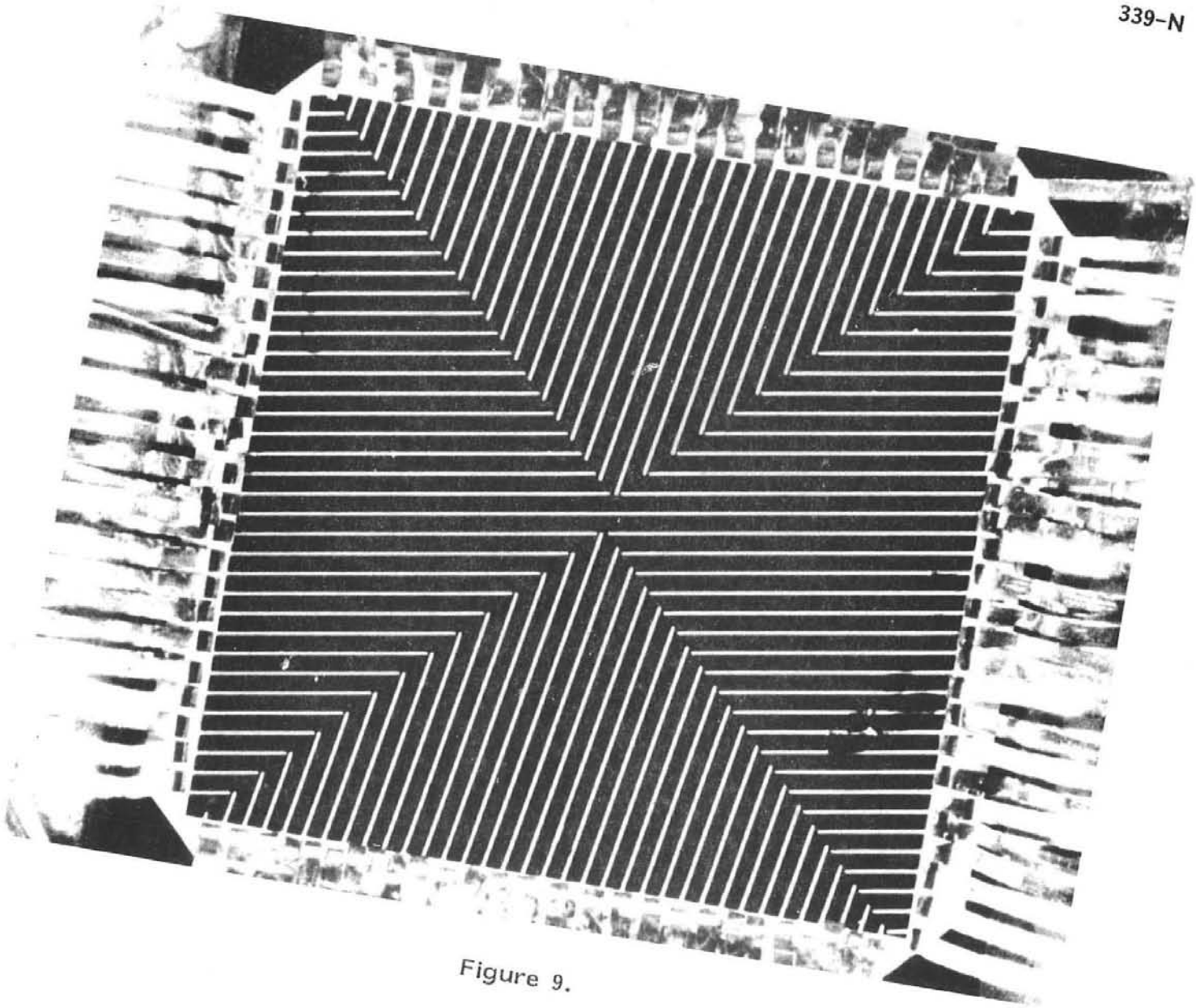

Figure 9.

It should be noted that the sawn edges of the cells do not play a significant role in the fill factor degradation. Compared with baseline cells, the T/E geometry has a 50% greater volume to edge ratio, and edge effects are not predominant in baseline cells.

4.3 Experiments with Secondary Concentrator

One of the options proposed by T/E in the original proposal to Sandia was the use of a secondary stage concentrator. This could be a dielectric type in optical contact with the cell, operating by internal reflection, and other types such as reflective cones were also mentioned. The advantages offered by this approach are: (1) the use of smaller cells becomes possible; (2) less pointing accuracy in the tracking system is required; and (3) more uniform cell illumination is obtained. Alternatively, the secondary stage can be used to reach higher concentration ratios, should that prove desirable.

In order to test the concept experimentally, a baseline EMVJ cell was thoroughly characterized from 1 to 1000 suns, and a glass secondary stage concentrator operating by internal reflection was then bonded to the cell. T/E performed the bonding with a silicate material after practicing on mechanical samples provided by M/A for this purpose. Measurements were then carried out to determine if the operation of the unit was as expected based on geometric considerations, and if any degradation of cell performance had been caused by the bonding process. The unit was also exposed to unfiltered 1000 sun illumination from the Xenon arc lamp for 1-2 days to see if degradation of the bonding material was occurring, and very little change was observed.

The one sun current was determined by outdoor measurements before and after bonding of the secondary concentrator. Various corrections were necessary in order to make a valid comparison because (1) the illuminated cell area was different with and without the concentrator, (2) the reflectance at the cell-concentrator interface is different from the cell-air interface and (3) the reflectance of the top surface of the concentrator must be taken into account. Otherwise, if not for these three items, the ratio of one sun currents would simply equal the ratio of the area of the

concentrator's top surface to the area of the cell. The concentrator is simply a solid glass cone 0.315" in height, with a top surface diameter of 0.377" and a bottom surface diameter of 0.250". When the correction factors for reflectance and difference in illuminated areas are multiplied by $(0.377)^2/(0.250)^2$, good agreement is obtained with the measured current ratio. The measured ratio is 1.83, and the calculated ratio is 1.88. The actual values of the one sun currents, determined from outdoor measurements, are 18.95 mA with the secondary and 10.35 mA without the secondary.

The fact that the secondary concentrator does not change the intrinsic cell performance is shown in Figure 10. The measured points for V_{oc} and FF at a given current output are in excellent agreement with and without the secondary. In order to achieve optimal cell performance with the secondary, an AR coating with an index of 2.3 - 2.4 is required (equal to $\sqrt{n_{si} n \text{ glass}} = \sqrt{(3.5)(1.5)} = 2.3$). This can be accomplished with evaporated TiO_2 or Ta_2O_5. Better techniques for attaching the secondary should also be investigated. It is felt that electrostatic bonding would not be an appropriate process for this application. The surface of the solar cell is not flat, as it has both the grooves and plated metal which sticks up above the surface. Electrostatic bonding on such a surface would require temperatures that would probably be detrimental to the relatively low temperature nickel-gold metallization scheme used on the cells.

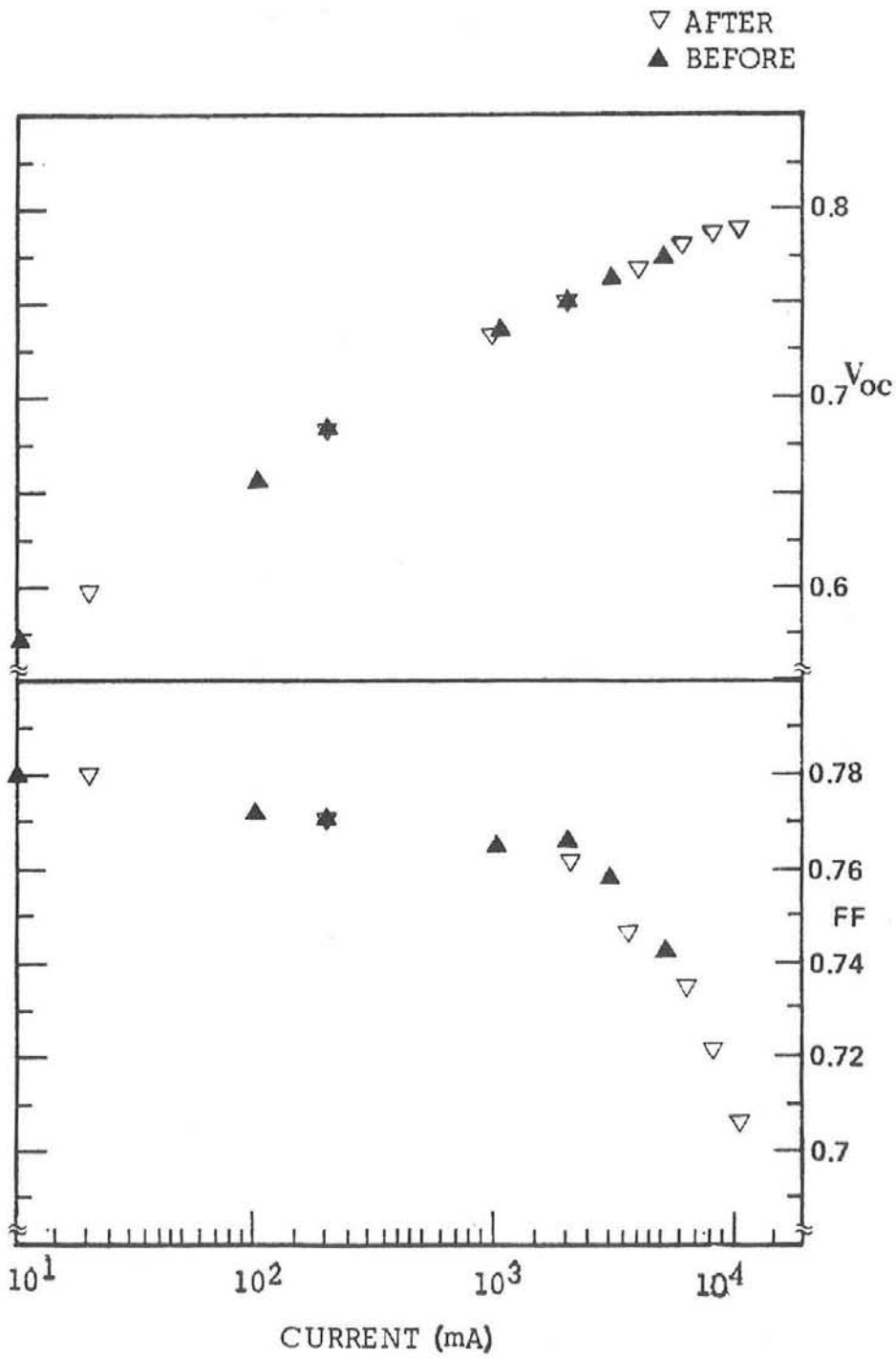
▽ AFTER
▲ BEFORE
0.8
0.7
V_{oc}
0.6
0.78
0.76
FF
0.74
0.72
0.7
10^1
10^2
10^3
10^4
CURRENT (mA)

FIGURE 10

5.0 CONCLUSIONS

The large quadrant-type cell developed for T/E peaks in efficiency at lower concentrations than would be expected from a direct scaling of Microwave Associates' 0.34 cm^2 cell. It appears that the source of this problem lies in either internal voltage drops or in non-uniform potentials along the unconnected grooves of different lengths. With further development the quadrant design should yield improved performance. The secondary stage glass concentrator appears to work well, and with an improved AR coating to match the indices of Si-glass interface, this approach to high concentration photovoltaic conversion using the Thermo-Electron lens system should be effective.

DISTRIBUTION LIST:

Acurex Corporation (3)
Attn: George Sutton
Bob Spencer
Dariush Rafinejad
485 Clyde Avenue
Mountain View, CA 94042

Aerospace Corporation
Attn: Ed Simburger
2350 El Segundo Blvd.
El Segundo, CA 90266

Alliance Tool Corporation
Fresnel Optics Division
Attn: Helmut Walter
1300 Mt. Read Blvd.
Rochester, NY 14606

Applied Solar Energy Corp. (2)
Attn: Frank Ho
Ken Ling
15251 E. Don Julian Road
City of Industry, CA 91746

ARCO Power Systems
Attn: Floyd Blake
Suite 307
7061 S. University Blvd.
Littleton, CO 80122

Arizona State University (2)
Attn: Charles Backus
Robert Sanderson
College of Engineering
Tempe, AZ 85281

Ray Bahm & Associates
Attn: Ray Bahm
2513 Kimberly Court NW
Albuquerque, NM 87130

Battelle
Attn: Don Carmichael
505 King Avenue
Columbus, OH 43201

The BDM Corporation (3)
Attn: Tim Lambarski
Wayne Kauffman
Bill Schwinkendorf
1801 Randolph Road SE
Albuquerque, NM 87111

Black & Veatch
Attn: Sheldon L. Levy
P. O. Box 8405
Kansas City, MO 64114

Boeing Engineering & Const. Co.
Attn: Roger Gillette
P. O. Box 3707
Seattle, WA 98124

Burns & Roe, Inc.
Attn: G. A. Fontana
800 Kinderkamack Road
Oradell, NJ 07649

Carbone Investment
& Management Corp.
Attn: Robert C. Carbone
570 Dwight Place
Berkeley, CA 94704

Chevron Research (2)
Attn: John Cape
L. Fraas
P. O. Box 1627
Richmond, CA 94802

Cyro Industries
697 Route 476
Clifton, NJ 07015

U. S. Dept. of Energy
ALO
Attn: D. L. Krenz
P. O. Box 5400
Albuquerque, NM 87115

U. S. Dept. of Energy
Attn: John Hanson
Nuclear & Geosciences Div.
P. O. Box 5400
Albuquerque, NM 87115

U. S. Dept. of Energy (9)
Div. of PV Energy Technologies
Attn: R. Annan
A. Krantz
M. Prince
L. Herwig (5)
A. Scolaro
1000 Independence Ave. SW
Washington, DC 20585

EPRI (2)
Attn: Roger Taylor
Ed DeMeo
P. O. Box 10412
Palo Alto, CA 94303

E-Systems (3)
Attn: Mark O'Neill
A. J. McDanal
Skip Waller
P. O. Box 226118
Dallas, TX 75266

General Electric Co.
Attn: Ron Hodge
P. O. Box 527
King of Prussia, PA 19406

Graham Hatfield
8402 Magnolia, Suite H
Santee, CA 92071

Hirst Company
Attn: Carrol Cagle
P. O. Drawer 1926
Albuquerque, NM 87103

Hughes Research Labs (2)
Attn: R. Knechtli
S. Kamath
3011 Malibu Canyon Road
Malibu, CA 90265

International Rectifier
Attn: Harold Weinstein
235 Kansas Street
El Segundo, CA 91214

Intersol Power Corporation (2)
Attn: John Sanders
Sid Broadbent
11901 West Cedar
Lakewood, CO 80228

Jacobs Engineering
Attn: Bob Martin
251 South Lake Ave.
Pasadena, CA 91101

Jet Propulsion Lab (3)
Attn: K. Shimada
R. Ferber
Solar Data Center
4800 Oak Grove Drive
Pasadena, CA 91109

Martin Marietta (3)
Attn: R. Hein
D. Hughes
J. Baumann
P. O. Box 179
Denver, CO 80201

McGraw Hill
607 Boylston St.
Boston, MA 02116

Microwave Associates
Attn: Joel Goodrich
South Avenue MS-116
Burlington, MA 01803

MIT/Lincoln Lab
Attn: John C.C. Fan
Box 73
Lexington, MA 02173

3M (2)
Attn: Sanford Cobb
Optical Technology Center
235 2D15
3M Center
St. Paul, MN 55144

Motorola
Attn: Keith Kingston
GED
8201 E. McDowell
Scottsdale, AZ 85252

NASA, HQ
Attn: John Loria
Code RET-1
Washington, DC 20546

New Shelter Home Magazine
9317 Shoshone
Albuquerque, NM 87111

Oak Ridge National Lab
Attn: Steve Kaplan
P. O. Box X
Oak Ridge, TN 37830

Photowatt (2)
Attn: William Taylor
Mike Keeling
2414 W. 14th Street
Tempe, AZ 85281

Power Hybrids
Attn: Jeff Meyer
1742 Crenshaw Blvd.
Torrance, CA 90501

PRC
Attn: E. Stirewalt
5201 Leesburg Pike
Suite 400
Falls Church, VA 22070

Purdue University (2)
Attn: Richard Schwartz
Mark Lundstrom
Electrical Engineering Dept.
West Lafayette, IN 47907

Quantum PV Concentrator Systems
Attn: James E. Molle
163 Verde Circle
Rohnert Park, CA 94928

Research Triangle Institute
Attn: Mayrant Simons
Box 12194
Research Triangle Park, NC 27709

SERI (3)
Attn: Gene Blakeslee
Lee Cole
John Benner
1617 Cole Blvd.
Golden, CO 80401

SERI, Library (2)
1536 Cole Blvd., Bldg. #4
Golden, CO 80401

Solar Works
Attn: Paul Wilkins
Route 2, Box 274
Santa Fe, NM 87501

Southern Cal Edison
Attn: Spencer Carlisle
2244 Walnut Grove Ave.
Rosemead, CA 91770

Spectrolab (2)
Attn: Brian Elm
Steve Olah
12500 Gladstone Avenue
Sylmar, CA 91342

Spire (4)
Attn: S. Tobin
M. Nowlan
R. Little
S. Rechtoris
Patriots Park
Bedford, MA 01730

Springborn Laboratories, Inc.
Attn: Bernard Baum
Enfield, CT 06082

Star Light Energy
Attn: J. Furber
4505 Dresden St.
Kensington, MD 20895

Strategies Unlimited
201 San Antonio Circle
Suite 205
Mountain View, CA 94040

Thermo Electron
Attn: Abbot Moffat
45 First Avenue
Waltham, MA 02154

United Energy Technologies
Attn: John Mackay
420 Lincoln Center Dr.
Foster City, CA 94404

University of Wisconsin
Attn: Prof. J. D. Wiley
Dept. of Electrical Engineering
Madison, WI 53706

UNM/NMERI
Attn: G. Leigh
Campus Box 25
Albuquerque, NM 87131

Varian & Associates (2)
Attn: R. Bell
N. Kaminar
611 Hansen Way K-219
Palo Alto, CA 94303

Wright Patterson AFB
Attn: Jack Geis
AFWAL/POOC
Wright Patterson AFB, OH

Wyle Labs (2)
Attn: Dave Christenson
George Meares
7800 Governors Drive West
Huntsville, AL 35807

1133 R. Chaffin
1133 J. Wiczer
1141 R. Dawson
1142 J. Gee
1811 R. Assink
1822 J. Sweet
Attn: M. Moss, R. Pettit
1823 M. Chamberlain
1845 R. Eagan
2146 R. Nasby
2146 J. Rodriguez
2146 H. Weaver
6200 V. Dugan
6220 D. Schueler
6221 J. Banas
6221 H. Gerwin
6223 E. Burgess
6224 E. Boes
6224 D. Arvizu
6224 L. Beavis
6224 C. Chiang
6224 M. Edenburn
6224 B. Hansen
6224 D. King
6224 A. Maish
6224 M. Rios
6224 B. Rose
6224 R. Siegel
6224 C. Stillwell
3141 L. J. Erickson (5)
3151 W. L. Garner (3)
3154-3 C. H. Dalin (25)
For DOE/TIC
(Unlimited Release)
8214 M. A. Pound